# Ultrafast dynamics of excitons in bulk and monolayer selenide transition metal dichalcogenides

vorgelegt von

**Simon Raiber**

aus Laupheim

im Jahr 2023

Promotionsgesuch eingereicht am: 29.01.2020

Die Arbeit wurde angeleitet von: Prof. Dr. Christian Schüller

Prüfungsausschuss: Prof. Dr. Tilo Wettig

Prof. Dr. Christian Schüller

Prof. Dr. Dominique Bougeard

PD. Dr. Jay Weymouth

Datum Promotionskolloquium: Feb. 2024

# Contents

# Chapter 1

# Introduction

One hundred years ago in 1924, Luis de Broglie proposed the concept of wave-particle dualism [Bro24]. The simple postulate that a particle behaves like a wave with a corresponding wavelength $\lambda = h/p$ that is inversely proportional to its momentum p initiated the metamorphosis from the rather rigid and lethargic classical physics towards the nowadays prevalent topic of quantum physics. This radical and fundamentally distinctive theory was able to provide a theoretical framework for the description of matter, reconciling the contradictions of classical physics. The capability to simulate the electronic structure of atoms, molecules and crystals, in particular the knowledge of the electronic band structure that determines the electronic and optical properties of a solid is essential for modern natural science. The rapidly expanding discipline of condensed matter physics has sparked innumerable technical applications. The development of transistors, lasers, medical imaging techniques, as well as DNA sequencing have revolutionised many fields like electronics, telecommunications,and medicine. Quantum mechanics has become the cornerstone of contemporary physics and paved the way to our modern way of life. Fundamental scientific research has evidenced its importance for the wealth of society. Tough, the former success of science has transformed over time to a service provider for technology. Nowadays, Quantum Computing or Artificial Intelligence is on every ones lips. Science which is connected in some way to such technological light houses is considered with very extensive funding. Considering myself, the motivation was not the promising economic perspective, but much more the desire to gain a more comprehensive picture of the underlying principles. From my perception, it is this intrinsic curiosity and passion that enables to proceed in fundamental research. I am very thankful for the opportunity to follow the visions of modern physics, starting from the ground-breaking postulations of Luis de Broglie up to the recent developments in semiconductor optics allowing

me to participate and add a very small contribution onto this topic. Accordingly, in this introduction, I will not argue for potential technological applications of exciton physics. Much more, I would rather like to point out what makes this subject appealing from a physical point of view.

The framework for these investigations form layered materials of the class of Transition Metal Dichalcogenides (TMDCs). While sounding rather exotic, this material family is not extraordinary exquisite but even occurs naturally. The layered structure of those crystalline materials is similar to common graphite. However, its' merit hide in the electronic and optical properties of these materials. Semiconducting TMDCs compose fertile host materials for so-called 'excitons'. These composite quasi particles form from an excited electron that binds to its vacant valence band state, resulting in a robust bound state which conceptually can be described in analogy to a hydrogen atom [Che14]. Moreover, excitons in TMDCs exhibit a very strong light-matter interaction and hence dominate the electrical and optical response of these materials in the vicinity of the band gap. A peculiar property of the TMDCs is the so-called 'spin-valley locking' and the concomitant optical selection rules that allow to address electronic transitions with a spin configuration fixed to the helicity of the circularly polarised light [Yao08; Cao12; Mak12]. This allows to inject and equally detect spin-polarised charge carriers. By the creation of an exciton, the spin components of the binding partners add up to a zero net spin but the spin orientation of its constituents is still well defined. Therefrom arises the expression of the exciton's 'pseudospin' [Mak10; Xu14; Jon14]. Unless the concept of an exciton appears to be rather figurative, this model has to balance the coexistence of the fermionic nature of its composites as well as the bosonic character of the quasiparticle itself. Depending on the context, excitons reveal a more fermionic character, for instance the existence of Pauli blocking [Sch85; Kli12], allowing for pump-probe investigations, as on the other side, they also exhibit bosonic properties which has been evidenced by the observation of a Bose-Einstein condensate of excitons [Kas06; Shi22]. The control and manipulation of the excitons' pseudospins nourishes the vision of valley spintronics, exploiting the (pseudo-) spin state to represent and process information [Xu14; Zib14; Ye17; Mue18]. Combined with the ability to address the pseudospin states optically, on-chip optical circuits may come into reach [Gon20; Gra23].

Taking stock of the field, there have been extensive studies mostly on single layers of TMDC crystals during the last decade due to the direct band gap, emerging in the monolayer limit [Spl10; Mak10]. Latter permits easy access via luminescence spectroscopy and therefore renders an excellent platform to investigate the abundance of other excitonic complexes such as trions [Ros13; Mak13] or (charged)

biexcitons [You15; Sie15]. More recently, the focus has moved towards the investigation of heterostructures and stacks of multiple van der Waals materials. The combination of different material properties, giving rise to an additional degree of freedom which originates from the variable stacking angle, has evoked diverse new phenomena like the discovery of superconductivity in 'magic-angle' graphene [Cao18], the emergence of moiré potentials [van14; Ale19; Jin19; Sey19; Tra19] and the finding of interlayer excitons with electron and hole residing in different layers or materials [Riv15; Kun18]. Interlayer excitons are of special interest because of their inherent permanent electric dipole along with a long lifetime up to several nanoseconds [Riv16] which allows for manipulation and external control [Par20]. Remarkably, the excitonic properties significantly change with the number of layers in a van der Waals crystal [Yeh15; Aro15; Aro18]. The distinct band extrema are notably shifted for different layer numbers and new excitonic states arise due to hybridisation effects [Slo19; Mun19; Zha23]. The dipolar interactions of hybridised excitons in bulk TMDC crystals can be electrically tuned [Erk23; Tag23; Zha23; Alt22]. Joint with their increased lifetimes compared to excitons in monolayer TMDCs [Riv16; Raz17; Li20], multilayer TMDCs present an utile base for a more advanced investigations regarding the excitons' pseudospin. The interplay between the distinct excitonic states is decisive for the resulting exciton dynamics of the considered material. In order to comprehend the temporal evolution of excitons in mono- and multilayer TMDCs, it is vital to fully understand the excitonic landscape and their interactions. In this ambit, we have been able to unveil pseudospin quantum beats on a femtosecond time-scale by applying strong in-plane magnetic fields [Rai22]. The discovered phenomena represents a significant step towards a full control of the excitons pseudospin in multilayer TMDCs that might be realised by combining time-dependent magnetic and electric fields. Within the scope of this thesis, it is aimed to give a comprehensive picture on the temporal dynamics of excitons in mono-and multilayer $WSe_2$ and $MoSe_2$. On that account, Time-resolved Faraday Ellipticity (TRFE) measurements with in- and out-of-plane magnetic fields up to 9 Tesla have been performed which are complemented by transient differential transmission pump-probe experiments. In addition, Time-integrated Four-Wave Mixing (TI-FWM) experiments have been conducted in order to access the coherent regime of the investigated exciton ensembles.

In the first chapter, the fundamentals electronic and optical properties of TMDC crystals, including the impact of magnetic fields as well as their rich excitonic landscape are briefly discussed. This is followed by a detailed introduction on exciton dynamics where the most important theoretical considerations for the

description of the dynamics of an ensembles of excitons are outlined. In the subsequent method chapter, all applied experimental techniques and their according evaluation approaches are discussed accompanied by exemplary measurements. Besides, the sample characterisation is also included in this chapter. The third chapter comprises an elaborate presentation and discussion of the results. The exploration of pseudospin quantum beats in multilayer $WSe_2$ and $MoSe_2$ that have a non-zero in-plane g-factor imprinted on their oscillation frequency constitutes the preeminent highlight of this work. The last section of this chapter is dedicated to preliminary results about degenerate two-beam FWM experiments. A summary with an outlook is given at the end of this thesis.

# Chapter 2

# Fundamentals

## 2.1 Transition metal dichalcogenides

Sparked by the Nobel price awarded discovery of atomically thin carbon which was coined as 'graphene' [Nov04], the material class of layered van der Waals materials has increased steadily. As the name indicates, the major resulting force between adjacent layers originates from van der Waals interaction whereas within the layers, comparably strong covalent bonds dominate the atomic interactions. The anisotropic binding forces permit the cleavage of few- or even monolayer sheets of the particular material. By the reduction of dimension and the possibility of combining different materials, the intrinsic electrical and optical properties are strongly altered, giving rise to an abundance of novel phenomena. The group of van der Waals materials comprises metals, semimetals, insulators, superconductors and in particular semiconductors [Liu16; Nov16; Wan18]. Latter ones are of special interest from a physical point of view as well as for technical applications, nourishing the vastly expanding industry of computation and communication technologies. The most eminent semiconducting van der Waals materials constitute the group of Transition Metal Dichalcogenides (TMDCs). Prominent members of this family are tungsten disulphide ($WS_2$), tungsten diselenide ($WSe_2$), molybdenum disulphide ($MoS_2$), and molybdenum diselenide ($WSe_2$). Although the basic properties of these materials have been investigated already many decades before [Fri63; Eva67; Wil69; Bro72], their actual breakthrough has been launched by the capability of the mechanical exfoliation of single layers. The inherent broken inversion symmetry in a single layer [Yao08] combined with strong spin-orbit interactions result a unique conjunction of the spin and valley degrees of freedom which renders TMDCs as an appealing platform for optical spin- and valley physics. The strong optical absorption of up to 20% of the incident light per layer

and the direct bandgap of many monolayer TMDCs [Spl10; Mak10] make them especially attractive for applications in optoelectronics [Mue18; Tha20]. Furthermore, TMDCs host a large variety of Coulomb-bound electron hole pairs which are entitled as 'excitons'. These quasi particles exhibit extraordinarily large binding energies such that excitons dominate the optical response of TMDCs even at room temperature [Kli12; Raj17; Wan18].

## 2.1.1 Crystal structure

The first investigation of the crystal structure of $MoS_2$, performing X-ray spectroscopy, was published one century ago by Rosco Dickinson and Linus Pauling [Dic23]. In the 70s of the past century, another cluster of publications about electronic and optical properties of TMDC bulk crystals was released [Fri63; Eva67; Wil69; Bro72]. The revival of TMDCs was stimulated by the discovery of the emergence of a direct band gap on monolayer $MoS_2$ [Spl10; Mak10]. In contrast to graphene, a single TMDC layer is strictly speaking not atomically thin. It is composed of transition metal atoms, for example molybdenum or tungsten, sandwiched between two layers of chalcogen atoms such as sulphur or selenium. The arrangement of the atoms figures a honeycomb-like structure with a hexagonal lattice. In the following, only selenide TMDCs are considered as these have been investigated in the here presented experiments. Top and side view of a prototypical TMDC are depicted in figure 2.1(a). A single layer exhibits a 3-fold symmetry (D3h) without inversion symmetry [Har71]. Within the layer, strong covalent bonds dominate the atomic interaction. The lattice constants for $MoSe_2$ and $WSe_2$ are almost identical and count 3.3 Å in the lateral dimension and 6.5 Å in vertical direction [Wil69; Bro72]. On top of the omnipresent van der Waals interaction between the layers adds a stacking energy due to the particular stacking orientation of the adjacent layers. The energetically favourable stacking orders occur at 0° and 60° twist angle. For configurations in close vicinity to these angles, atomic reconstruction takes place, causing a domain formation [Ros20]. For larger deviations, a so-called 'moiré' structure forms. The naturally occurring stacking order in a bulk TMDC crystal is the 2H stacking order which implies that every neighbouring layer is rotated by 60° (equivalent to a rotation by 180°) with respect to each other. A cross section of an H-type TMDC crystal is presented in the lower part of figure 2.1(a). Another stable stacking order constitutes the 3R stacking order where the adjacent layers are not twisted (0°) but laterally shifted with respect to each other. For selenide TMDCs, industrially grown 3R bulk crystals are not commercially available up to now.

The corresponding reciprocal lattice transforms also to a hexagonal lattice. An illustration of the hexagonal first Brillouin zone is shown in figure 2.1(b). The symmetry points at the zone edges denote the K points. From the absence of inversion symmetry in a single layer, it follows that the opposing K points are inequivalent. Further on, the K points will be distinguished by their valley index into $K^+$ and $K^-$. The inequivalence does also hold for the $\Sigma$ points which play an important role in the bulk material. The alternating layer orientation in an H-type multilayer crystal entails also in reciprocal space a rotation of 180° with respect to each layer.
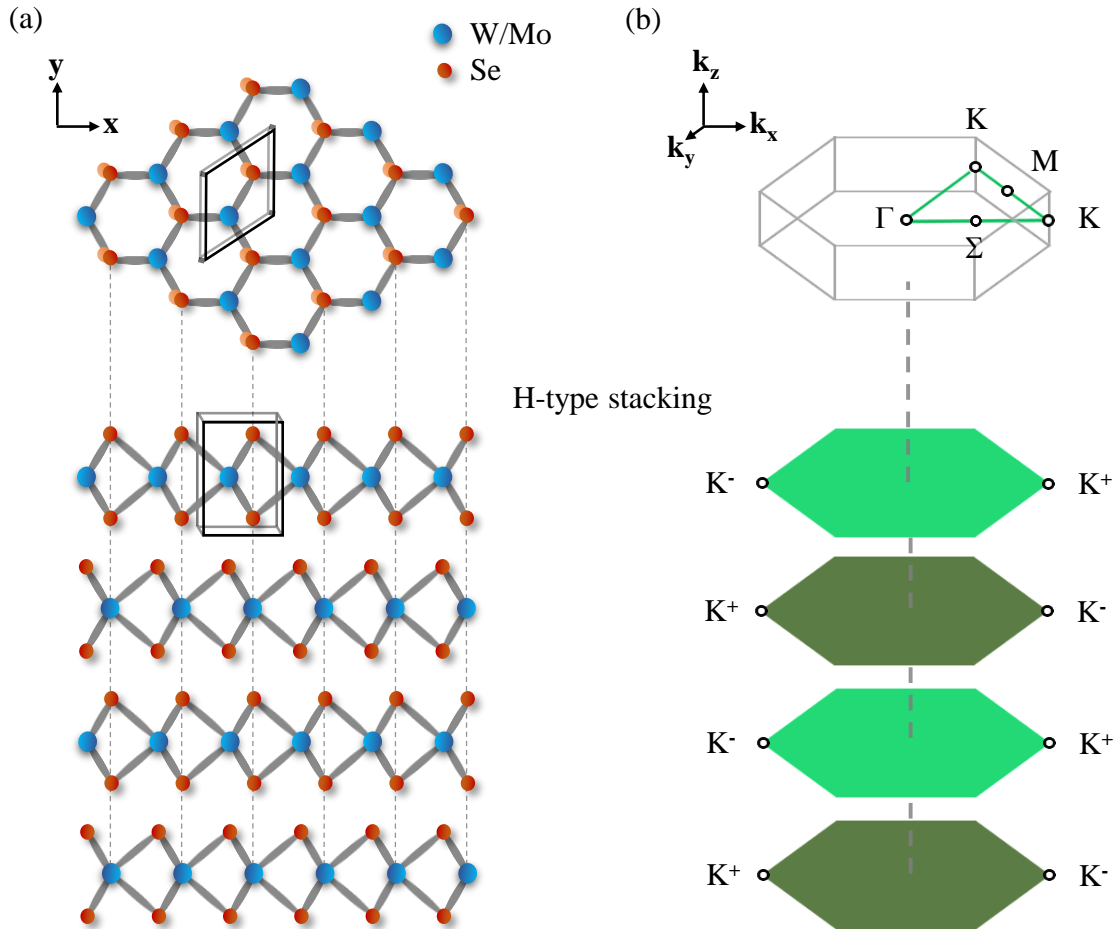


**Figure 2.1: Structure of H-type TMDCs in real and reciprocal space.** Orange spheres symbolise the selenium atoms while the blue ones denote the tungsten or molybdenum atoms. (a) Top view and side view of a 2H stacked TMDC crystal structure. A naturally grown bulk crystal obeys the 2H stacking order implying a rotation of 180° with respect to the adjacent layers. A cross section of the unit cell is outlined in black. (b) First Brillouin zone of a TMDC. Owed to the lack of inversion symmetry, the K points at the corner of the zone are inequivalent and commonly denoted as $K^+$ and $K^-$. In reciprocal space, the 2H stacking leads equally to a twist of the reciprocal layers such that the valley indices of the individual layers alternate in the vertical direction.

## 2.1.2 Optical and electronic properties

In order to determine the material specific electronic and optical properties, a profound knowledge about the electronic band structure is necessary. The band alignment of the bulk material reveals an indirect bandgap between the valence band (VB) at $\Gamma$ and the conduction band (CB) at K with transition energies covering the near infrared regime. An intriguing feature in TMDCs constitutes the transition to a direct band gap semiconductor when it is thinned down to a single layer [Spl10; Mak10]. The underlying mechanism becomes seizable by analysing the orbital composition of the CB and VB. Density functional theory (DFT) calculations can provide this information [Kor15] (cf. figure 2.2(a) and (b)). While the states at the K point are mainly composed by d orbitals that stem from transition metal atoms, the states at the $\Gamma$ point mostly consist of the chalcogen atoms' $p_z$ orbitals [Li07; Zhu11; Kor15]. By removing the neighbouring layers, the orbitals of the chalcogen atoms deform whereas the intercalated transition metal atoms are effectively shielded and hence nearly insusceptible to the altered surrounding. This results in an increase of the energy gap at the $\Gamma$ point while the CB and VB at K remain largely unperturbed rendering a direct band gap.

A remarkable characteristic of TMDCs is the strong spin-orbit coupling (SOC) originating from the comparably heavy transition metal atoms. As a consequence, a significant spin splitting in the VB emerges, counting around 0.2 eV (0.4 eV) at the K points for the molybdenum-based (tungsten-based) TMDCs. The CB spin splitting at K is much smaller featuring some tens of meV which is owed to partial compensation of the p and d states contributions in the SOC [Koś13; Liu13; Kor15]. Remarkably, the sign of the spin splitting is opposite for Mo- and W-based TMDCs. In the case of MoSe$_2$, an anti crossing of the spin-split bands occurs due to different effective masses [Lu20; Yan20].

The light-matter interaction is dictated by optical selection rules. Due to time-reversal symmetry and given half-integer spin, Kramers' theorem proclaims that there has to be a degenerate state with opposite spin. As a result, the spin characters of the bands at the high symmetry points have reversed order under inversion. From symmetry arguments it can be derived that the optical selection rules are chiral. Optical transitions ought to be spin-conserving, thus, only electronic transitions between bands with the same spin state are allowed [Yao08; Cao12; Mak12]. With this considerations, the band structure at the K points can be modelled in a simplified schematic picture which is presented in figure 2.3. The robust spin splitting in the VB and CB joint with the optical selection rules allows to address a transition in a specific K valley which is termed as 'spin-valley locking'.
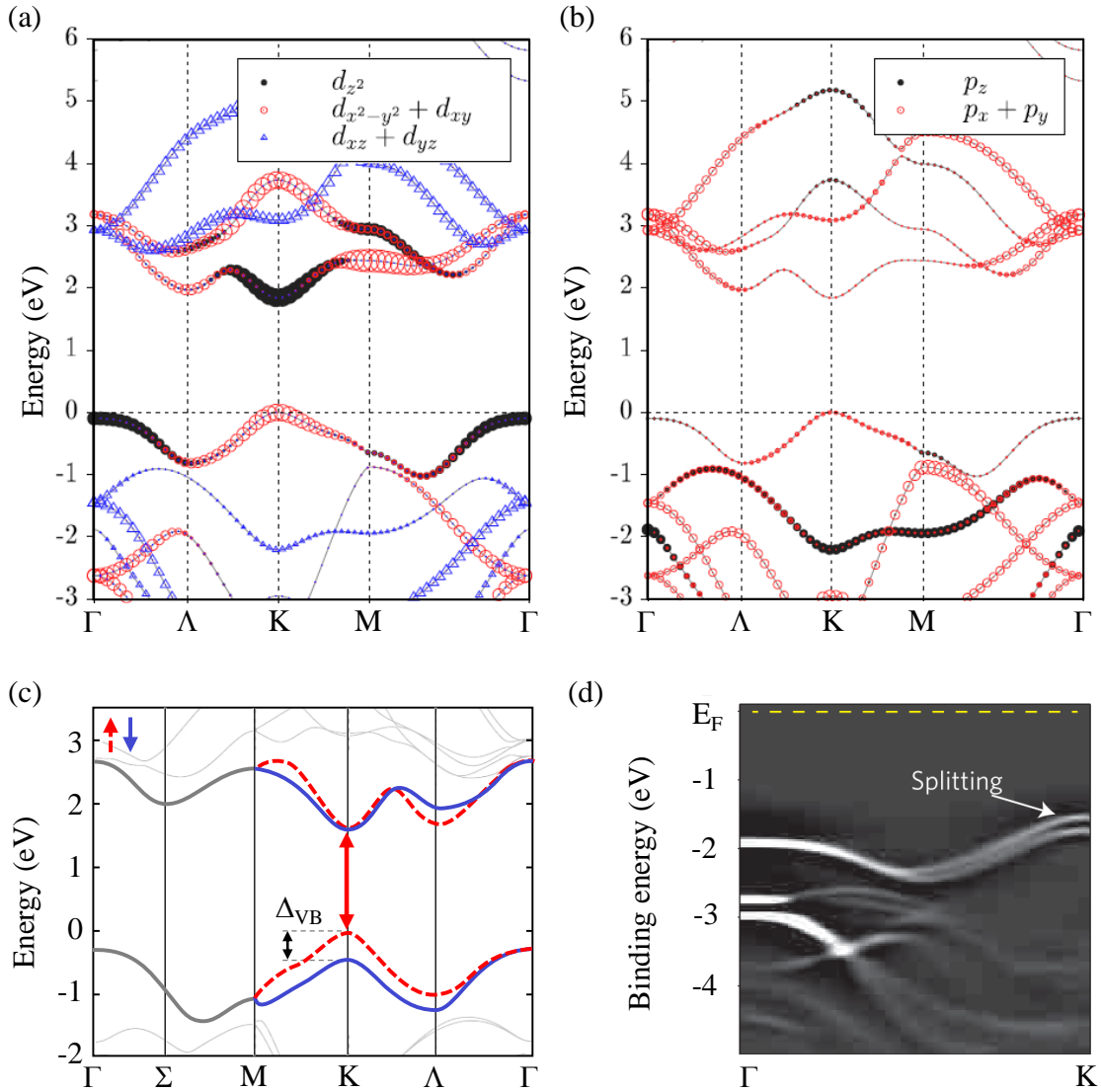
**Figure 2.2: Orbital contributions to the monolayer TMDC band structure and spin-orbit induced band splitting.** (a) displays the band structure contributions of the d orbitals from the transition metal atoms, whereas in (b), the impact of the p orbitals of the chalcogen atoms are depicted. The volume of the symbols scales with the orbital weight. Spin-orbit coupling was neglected in this approach which has been performed by Kormanyos et al. [Kor15]. (c) Due to the heavy masses of the transition metal atoms, a strong spin-orbit splitting is induced. Red and blue lines denote spin up and down, respectively. (d) The spin-split CB is well observable in the angle-resolved photoemission spectroscopy measurement of Zhang et al. [Zha14]. Graphs (a)-(c) reproduced from [Kor15].

For samples consisting of multiple layers, the situation becomes more intricate. In compounds with an even number of layers, inversion symmetry is restored whereas it remains broken for an odd number of layers. Since inversion symmetry dictates whether the bands are spin-degenerate or not, the number of layers in principle decides over the spin degeneracy of the regarded system. In the limit of a very
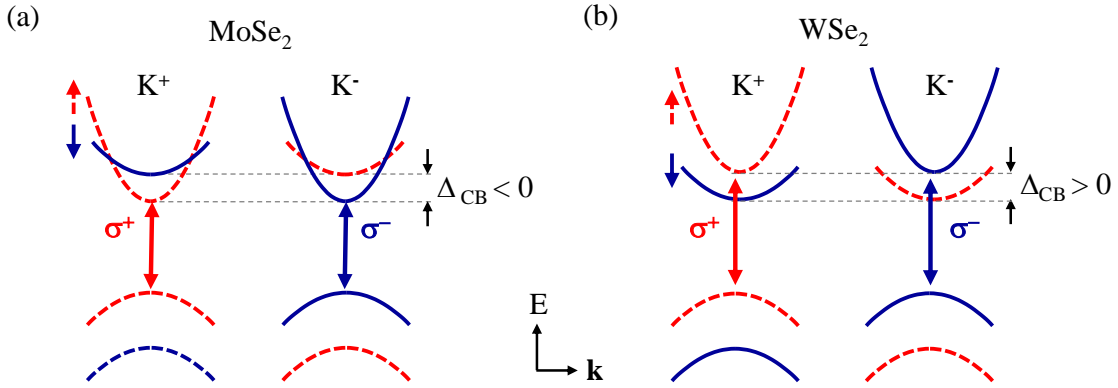
(a)   MoSe$_2$
(b)   WSe$_2$



**Figure 2.3: Schematic illustration of the band structure at the $K^{\pm}$ points.** The dispersion around the high-symmetry points $K^+$ and $K^-$ can be modelled within a parabolic approximation. Optical transitions need to be spin-conserving and obey the chiral selection rules. (a) Molybdenum-based TMDCs reveal a spin-split conduction band (CB) with a negative energy splitting. Due to different effective masses, a crossing of the spin-split bands in the CB occurs. (b) Tungsten-based TMDCs exhibit a reverse order of the spin-split bands compared to Mo-based TMDCs. In WSe$_2$, the lowest energy state is consequently optically forbidden and referred to as a dark state.

thick structure, the argument of an odd or even layer number is softened since a bulk TMDC is commonly considered to be spin-degenerate [Kli12]. Regarding 2H bulk material, the K valleys alternate from layer to layer (cf. figure 2.1 (b)) but the optical selection rules are preserved for every single layer. Hence, it is still possible to generate photo carriers with a fixed spin according to the helicity of the incident light. This is referred to as spin-layer locking [Jon14; Gon13; Raz17].

## 2.1.3 Magnetic fields

Experiments in magnetic fields are an indispensable tool in semiconductor physics. For instance, Hall measurements represent an important tool to determine effective masses of carriers [Kli12]. In general, the effect of the magnetic field on the material properties depends on the orientation of the field with respect to the crystal. Regarding TMDCs, an external magnetic field orthogonal to the crystal layers breaks time-reversal symmetry. By shifting the opposite valleys to different energies, valley degeneracy is lifted. Moreover, this leads to a redistribution of the carriers between the valleys which is termed as 'magnetic-field-induced valley polarisation' [Li14; Aiv15]. Magnetic fields applied in parallel to the layer plane induce a mixing of the spin states of the according bands giving rise to a partial brightening of dark states in monolayer TMDCs [Zha17; Ech16]. The Zeeman effect describes the shift of the energy states, scaling linearly with the strength

**Table 2.1: Results of ab-initio calculations for effective g factors.** Computed values of out-of-plane and in-plane spin S, and orbital angular momenta L for the CB and VB states at the K points of selenide TMDCs. For out-of-plane orientation, only the z component accounts whereas for in-plane configuration only the x component contributes (y and x are equivalent). The overall effective g factor is given by twice the difference of the CB and VB values. Paulo E. Faria Junior has conducted this calculations [Rai22].

|  | Monolayer WSe$_2$ | bulk WSe$_2$ | Monolayer MoSe$_2$ | bulk MoSe$_2$ |
|---|---|---|---|---|
| | **out-of-plane** | | | |
| $S_z^{CB}$ | 0.98 | 0.97 | 1.00 | 1.00 |
| $L_z^{CB}$ | 2.97 | 2.98 | 1.81 | 1.76 |
| $S_z^{VB}$ | 1.00 | 1.00 | 1.00 | 1.00 |
| $L_z^{VB}$ | 5.00 | 4.40 | 3.96 | 2.67 |
| $g_{eff,\perp}$ | -4.10 | -2.89 | -4.30 | -1.84 |
| | **in-plane** | | | |
| $S_x^{CB}$ | 0.00 | 0.00 | 0.00 | 0.00 |
| $L_x^{CB}$ | 0.00 | 0.00 | 0.00 | 0.00 |
| $S_x^{VB}$ | 0.00 | 0.47 | 0.00 | 0.74 |
| $L_x^{VB}$ | 0.00 | $\pm 0.07$ | 0.00 | $\pm 0.06$ |
| $|g_{eff,\parallel}|$ | 0.00 | 0.80...1.08 | 0.00 | 1.36...1.60 |

of the magnetic field. The proportionality constant is given by the gyromagnetic ratio $g$. As the spin-split VBs and CBs all are shifting individually, it has established to introduce an effective g factor $g_{eff}$ for TMDCs. It is defined by the energy difference of a specific transition (commonly the band gap at the K valleys) with opposite valley index, i.e.

$$E^{K^+}(B) - E^{K^-}(B) = g_{eff} \cdot \mu_B \cdot B \tag{2.1}$$

with $\mu_B$ denoting the Bohr magneton [Mit15; Mac15; Aro16; Sti16]. Since 2020, ab-initio approaches based on DFT calculations represent the state-of-the-art method to model the Zeeman shift in TMDCs [Woź20; Dei20; För20; Xua20]. The starting point constitutes a Hamiltonian that is composed by the unperturbed electron energy and the interaction of the magnetic field with the angular momentum and the spin component. The electronic wave function is described by a Bloch state. As initial input, the geometry of the atoms, i.e. the lattice parameters and the size of the k-grid that is modelled (an infinite crystal would exceed the computational power) have to be implemented. Subsequently, the electron density and the corresponding eigenenergies are computed. Within a self-consistent approach, the resulting values serve again as starting conditions for the next it-
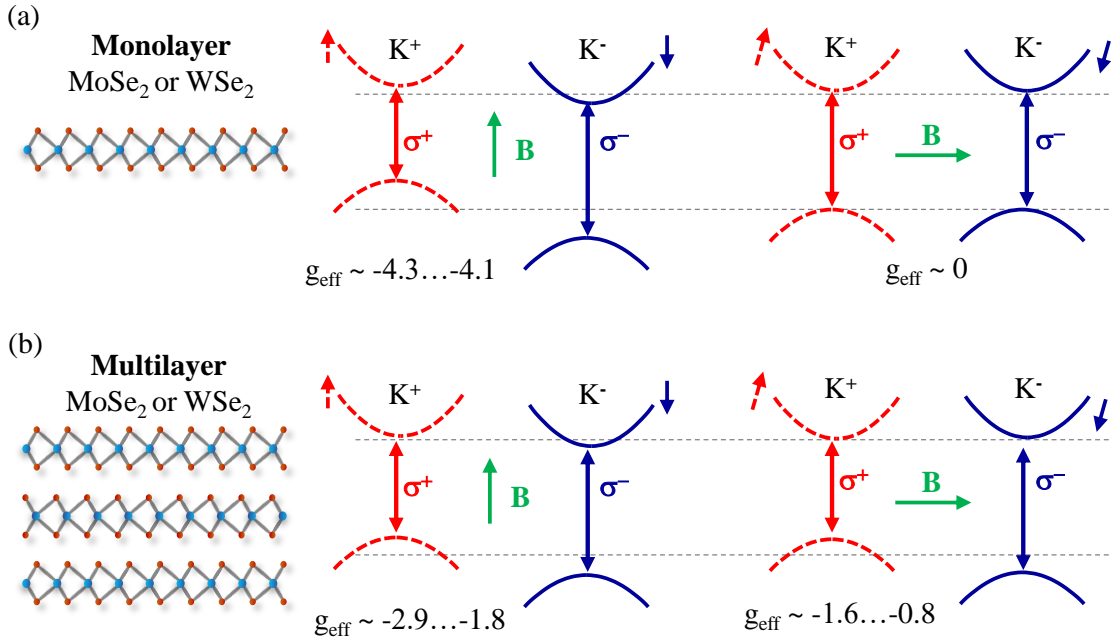
(a)

**Monolayer**
MoSe$_2$ or WSe$_2$

$g_{eff} \sim$ -4.3...-4.1

$g_{eff} \sim$ 0

(b)

**Multilayer**
MoSe$_2$ or WSe$_2$

$g_{eff} \sim$ -2.9...-1.8

$g_{eff} \sim$ -1.6...-0.8

**Figure 2.4: Influence of magnetic fields on the valley structure of se-lenide TMDCs.** For simplicity, only the bands for the optical transitions that are lowest in energy are presented. The grey dotted lines indicate the energy levels of the band edges at B = 0. As presented in table 2.1, the Zeeman shift is composed of spin and angular momentum contributions resulting in an individual shift of VB and CB. The effective g factor represents the proportional constant of the energy difference between K$^+$ and K$^-$, i.e. $\Delta E(K^{\pm}, B) = g_{eff} \cdot \mu_B \cdot B$. (a) For monolayers exposed to in-plane magnetic fields, the effective g factor is zero but the spin states get mixed which is indicated by the tilted spin arrows. (b) For bulk crystals, in addition to the coupling of the spin states, recent ab-initio calculations reveal a non-vanishing effective g factor.

eration. This is conducted for more than a hundred bands and hence does not only comprise the states of the valence electrons but also the inner shell electrons since every band corresponds to one electron. Thereby, the convergence of the contributions of spin and angular momenta is verified. As a final output, the contributions to the effective g factor, originating from spin and angular momentum for the CB and VB states are obtained. The difference of the CB components and the VB components delivers the contributions of one valley. In table 2.1, the computed values for mono- and multilayer WSe$_2$ and MoSe$_2$ are listed. Because of time reversal symmetry, the bands in the opposed valley shift exactly reverse, so doubling the shift of one valley yields the effective g factor. Note that for out-of-plane orientation, only the z components of the angular momenta contribute whereas for in-plane configuration, only the x component is relevant (x and y components are equivalent). Remarkably, only the valence band exhibits a contribution to g$_{||}$ for multilayer TMDCs while for the conduction band, it is strictly

zero, i.e. the orbital component $L_x^{CB}$ as the spin component $S_x^{CB}$ are both zero. This arises from the particular symmetry of the bands (CB $\sim \Gamma_9$ and VB $\sim \Gamma_7$ in the $D_{3h}$ point group of the K valleys) which is similar to the effective g factor of $g_{||} = 0$ for in-plane magnetic fields of the heavy-hole valence band in wurtzite materials with hexagonal symmetry [Ven77; Far19]. The obtained values are in very good accordance with calculated [Kat20; Woź20; Dei20; För20; Xua20] and experimentally determined effective g factors in literature [Li14; Wan15b; Mac15; Aro16; Aiv15; Sti16]. In figure 2.4, the impact of in- and out-of-plane magnetic fields on the band structure around the K valleys is visualised and summarised.

## 2.2 Excitons

In semiconductor physics, one of the fundamental description of charge carriers is the concept of electrons and holes. Latter one figures a vacant electron state in the VB and can be described by a quasi particle with opposite charge, effective mass and spin compared to an electron. Within this framework, the charge carrier dynamics can be described in a particle picture. The material properties are comprised in the explicit texture of the band structure. Delving into this concept, it becomes natural that there is interaction among the particles. Concerning Coulomb interaction, bound states comparable to a positronium, atom-, or a molecule-like complex become conceivable. In fact, electrons and holes can form Coulomb-bound pairs, resulting in a metastable state which has been coined as 'exciton'. An exciton is regarded as a quasi particle without net charge. Binding energies of excitons range between tens of meV in inorganic bulk crystals [Kaz14] or in GaAs quantum wells [Mil85] up to several eV in organic semiconductors as for instance used in OLED-technology [Knu03]. Extensive fundamental research on excitons in III-V quantum wells was realised already in the eighties of the last century, establishing the basic concepts of excitons [Mil85]. Their comeback has arisen with the revival of TMDCs since excitonic transitions determine the optical response of those materials [Yu10; Kli12; Raj17; Wan18]. Moreover, this allows the formation of charged excitons or molecule-like excitonic complexes [Ros13; Mak13]. A schematic illustration of different types of excitons is shown in figure 2.5(a). In multiple layers (of different materials), interlayer excitons (ILX) may form. Here, electron and hole reside in different layers of a crystal [Aro17; Par20] (a heterostructure [Riv15; Kun18]).

## 2.2.1 Composition and description

For the modelling of the excitonic states, apart from the Coulomb interaction, it is crucial in which manner the surrounding potential is approximated. Within the approach of Frenkel [Fre37], excitons are assumed to be localised, sensing the potential of the neighbouring atoms. This ansatz yields bound states with very high binding energies up to the eV range. Alternatively, excitons can be regarded as being delocalised over many unit cells of the crystal. Under this presumption, the impact of the surrounding can be approximated by an averaged potential. Following the concept of Wannier [Wan37], a description analogous to a hydrogen atom can be applied, delivering comparably small exciton binding energies [Kli12]. The energy hence is given by

$$E(n) = -\frac{\mu R_H}{m_0 \epsilon_r^2 n^2} = -\frac{R_X}{n^2}. \tag{2.2}$$

Here, n denotes the principal quantum number of the state, $\mu$ the reduced exciton mass, $m_0$ the electron rest mass, $\varepsilon_r$ the materials dielectric constant and $R_H$ the Rydberg constant. $\frac{\mu R_H}{m_0 \varepsilon_r^2}$ can be defined as the modified exciton Rydberg energy $R_X$. In analogy to the Bohr model, the radius of the orbit is given by [Kli12]

$$r_n = \frac{m_0}{\mu} \epsilon_r n^2 a_H = n^2 a_X. \tag{2.3}$$

Here, $a_H$ denotes the Bohr radius of the hydrogen atom. Concerning excitons in two dimensions, which is convenient for excitons in monolayers, the upper expressions are slightly modified. Most important, the principal quantum number n needs to be substituted by $n - \frac{1}{2}$ when going from 3d to 2d systems. The modified exciton Rydberg energy $R_X$ does not change. Consequently, the binding energies of the lowest exciton state is $1 \cdot R_X$ in 3d and $4 \cdot R_X$ in 2d. Thus, the oscillator strength increases and $r_n$ decreases by the reduction of dimension [Kli12]. Moreover, the removal of the neighbouring layers leads to a so-called 'reduced dielectric screening' resulting in an additional boost of the binding energy, but also in a deviation of the two-dimensional Rydberg series [Che14].
Technically speaking, the description of excitons in TMDCs is somewhere in-between the Wannier-Mott approximation and the Frenkel-type exciton because the typical exciton Bohr radii and the size of an unit cell differ less than one order of magnitude. Besides, the binding energies range between 0.5 -0.2 eV and are extraordinary high for the ansatz of Wannier. However, the experimental evidence of the exciton Rydberg series [Che14] is a strong indication for a Wannier-
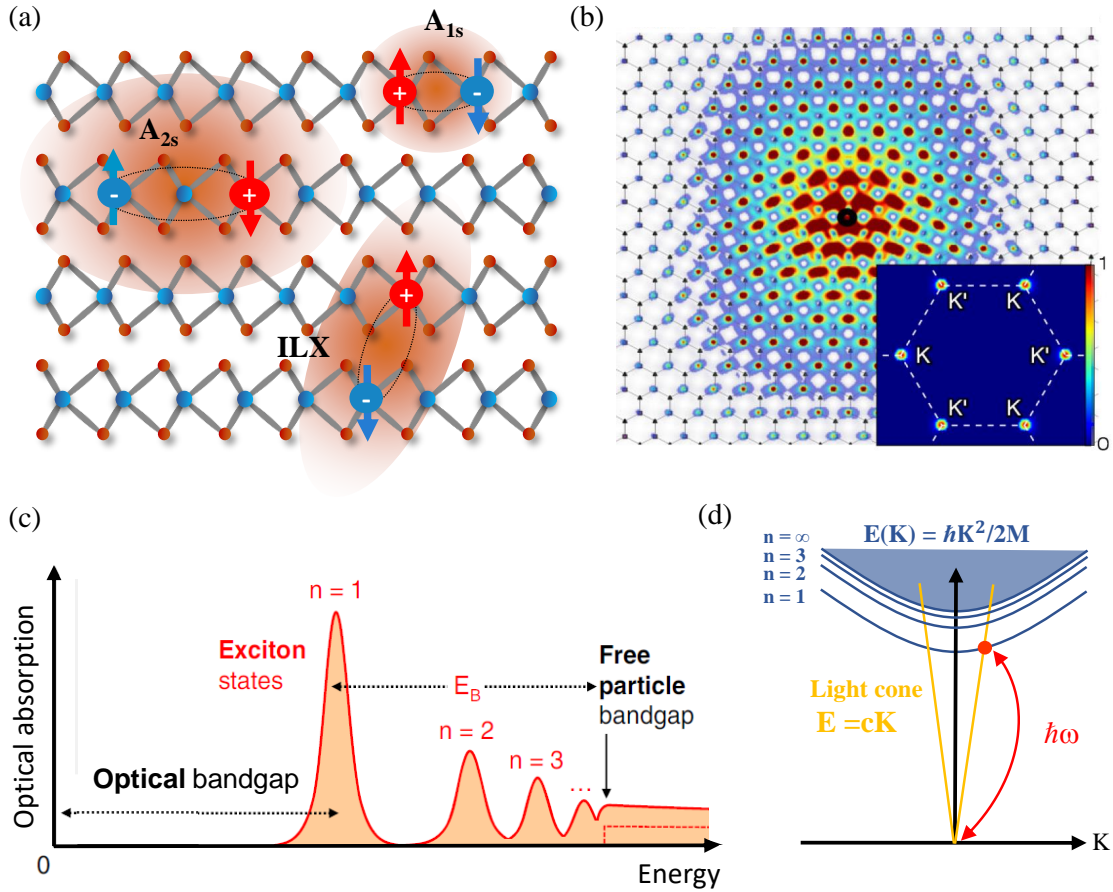
**Figure 2.5: Composition and properties of excitons.** (a) Schematic representation of different types of excitons in a multilayer crystal. The mutual attractive Coulomb interaction between electron and hole gives rise to bound states. Excited excitonic states, for instance the $A_{2s}$ exciton or an interlayer excitons (ILX) can also form in TMDC materials. (b) Modulus squared of the wave function of the $A_{1s}$ exciton calculated for monolayer $MoS_2$ via the GW-BSE while the position of the hole is kept at the centre. The inset presents the according distribution in k-space. Figure reprinted from [Qiu13]. (c) Illustration of the optical absorption in a semiconductor which hosts excitons. The transitions mimic a Rydberg series that converges as the free particle bandgap is approached. The optical bandgap is lowered by the exciton ground state binding energy. n denotes the principal quantum number in analogy to an atomic level structure (scheme adapted from [Wan18]). (d) Exciton dispersion (blue parabolas) with respect to the centre-of-mass momentum $K = k_{el} + k_{hole}$. Direct optical transitions have to fulfil energy and momentum conservation and thus are exclusively permitted at the intersection with the light cone (yellow lines).

type behaviour of excitons. Its nomenclature derives from the fact weather the optical transition includes the upper or the lower spin-split CB. First ones are labelled as A excitons and latter ones as B excitons. For instance, the neutral ground state exciton is denoted by $A_{1s}$. The indices refer to the principal quantum

number and the letter to the orbital momenta of the excitonic wave function. Figure 2.5(b) depicts the calculated distribution of the wave function of an $A_{1s}$ exciton for monolayer $MoS_2$. In real space it reveals an extent over several unit cells while being strongly confined at the K points in reciprocal space [Qiu13]. Experimental findings evidence that the Bohr radius is smaller than the results of Qiu et al. propose. Values of approximately $a_X = 1$ nm have been reported for hBN encapsulated monolayer TMDCs [Zip18; Sti18]. Figure 2.5(c) illustrates a characteristic TMDC absorption spectrum which is dominated by strong excitonic effects. The optical bandgap is lowered by the binding energy of the exciton. Excited exciton states appear following $E_B \sim \frac{1}{n^2}$ approaching a continuum state at the free particle band gap. As the excitonic states are lower in energy as the individual carriers, the description of excitons in the electronic band structure is insufficient. Therefore, a two-particle dispersion with respect to their centre-of-mass momentum $K = k_{el} + k_{hole}$ is convenient (cf. figure 2.5(d)). Due to momentum and energy conservation, direct optical transitions can only occur at the intersection with the linear dispersion of light $E = cK$ with c denoting the speed of light. Figuratively, the linear dispersion of light is entitled as 'light cone'. The optical selection rules discussed in the section before hold equally for excitons since they are formed of electrons and holes obeying the constraints of the electronic band structure. Despite of the bright exciton's zero net charge and zero total spin, the constituent electron and hole possess a fixed spin orientation locked to the valley where the transition took place and thus to a fixed circular polarisation of light. By definition, a valley pseudospin, which is assigned to the valley that hosts the exciton transition, imports this information by a binary character $\tau = \pm 1$.

## 2.2.2 Dynamics

In order to exploit the new degree of freedom of the valley pseudospin for valleytronic and optoelectronic applications, a profound knowledge of the excitons' temporal evolution and the according valley dynamics as well as its coherence is required. This includes the formation processes, the interaction with other excitons, and finally the decay mechanisms. The investigation of the excitons' coherence and lifetime constitute a basic building block therefore.

In general, the temporal evolution of excitons can be described within two different regimes, namely the coherent and the subsequent incoherent regime. In the first one, the photo-excited particles share a phase relationship among them selves and the generating light field. In this time segment, many fundamental quantum

mechanical processes take place as Bloch oscillations, photon echoes and quantum beats [Sha13]. In the incoherent regime, scattering events accompanied with thermalisation processes dictate the carrier dynamics. Particularly for excitons in TMDCs, the decay of valley polarisation is mediated by long-range exchange interaction [Yu14; Gla15]. Moreover in bulk crystals, the indirect band gap allows for enhanced intervalley scattering [Wal16; Bre19].

As a fundamental introduction, the concept of the quantum mechanical description of an ensemble of independent two-level systems interacting with a classical electro-magnetic field is presented here. It follows the description of J. Shah [Sha13]. The most elementary quantum mechanical framework to describe an exciton constitutes a two-level system with the ground state representing no exciton and an exciton denoting the excited state. Most simple, no interaction between the individual two-level systems is assumed. Technically, this is realised by exploiting the density matrix formalism which obeys the Liouville variant of the Schrödinger equation. The corresponding Hamiltonian is made up by three components, figuring an unperturbed, an interaction and an relaxation component, i.e. $\mathcal{H} = \mathcal{H}_0 + \mathcal{H}_{int} + \mathcal{H}_{relax}$. Latter one comprises constant phenomenological longitudinal and transverse relaxation rates for the lifetime of the excited states and the life time of the coherent superposition states which are defined as $T_1$ and $T_2$, respectively. This ansatz is called 'Markovian', presuming the coupling of the excitation to a 'bath' [Kli12]. Following these principles, the coupled equations of motion for the population and polarisation can be derived which are known as the 'Optical Bloch Equations'. There is no analytical solution for those coupled equations. They can be either expanded or numerically solved. In order to describe four-wave mixing experiments it is sufficient to expand the equations up to the third order as this is a third-order non-linear process. In semiconductors, however, the two-level systems cannot be assumed to be entirely independent as in separated atomic systems. Coulomb interaction between different polarisation components has to be included which results in the 'Semiconductor Bloch equations'. The solutions of the Bloch equations can be visualised on a so-called Bloch sphere which is a geometrical representation of a qubit introduced by Felix Bloch in the fifties of the last century [Blo46]. In this context, north and south pole of the sphere can be assigned to the ground state $|0\rangle$ and the excited state $|X\rangle$, respectively. Every state can be represented by a point in the Bloch sphere. Its vertical orientation monitors the superposition of the ground and excited state while the horizontal position renders its phase. The two fundamental relaxation times act in longitudinal ($T_1$) and transverse direction ($T_2$). Figure 2.6 shows the exciton dynamics imprinted on the Bloch sphere. The experimental access to the
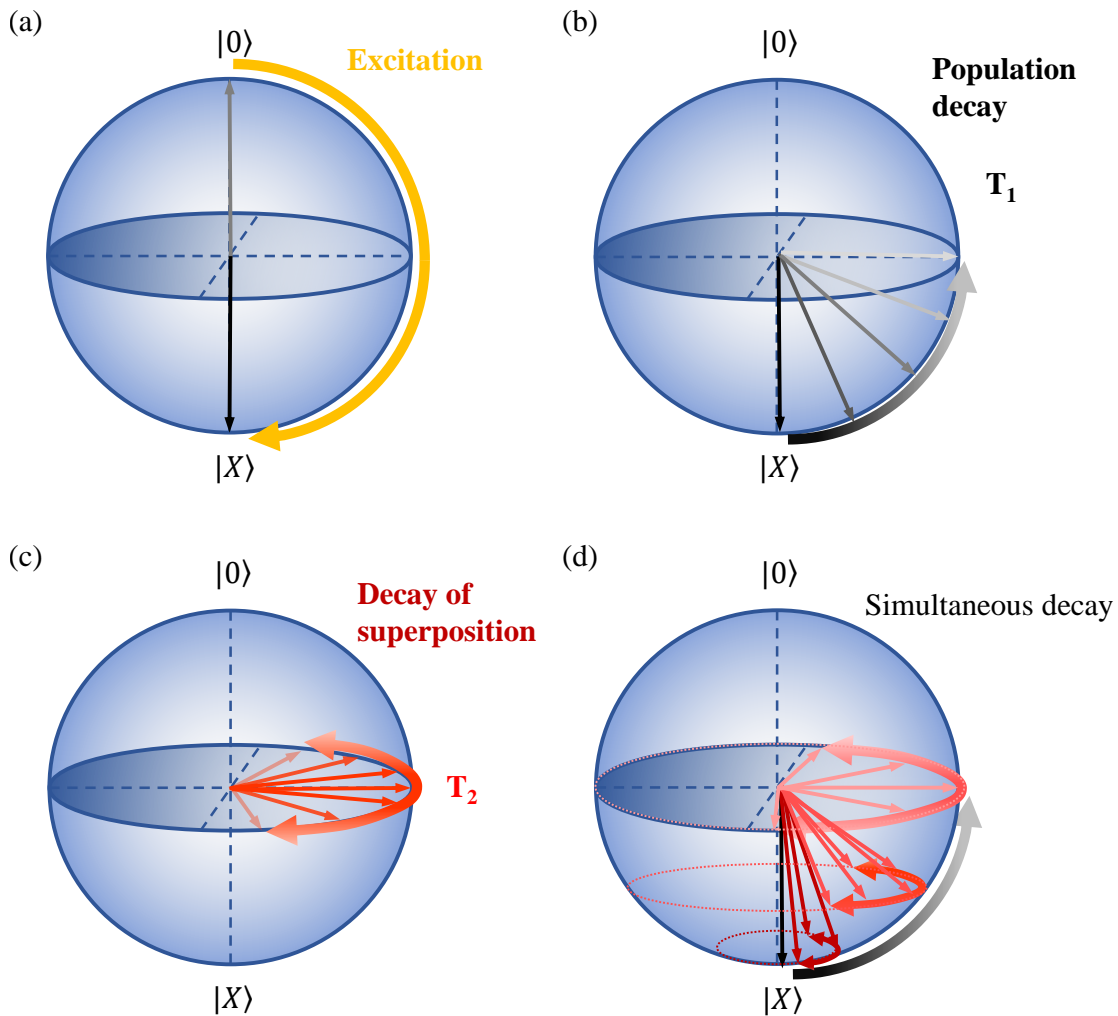
**Figure 2.6: Exciton dynamics visualised on a Bloch sphere.** In the most simplest consideration, an ensemble of excitons can be regarded an ensemble of quantum mechanical two-level system whose states can be represented by an arrow on the Bloch sphere. Depending on the energy, intensity and duration of the excitation, an arbitrary state on the Bloch sphere can be initialised. Assuming perfect coherent excitation, all systems are initially in the same state. (a) For instance, all oscillators can initially be prepared in the excited state. (b) Over time, the population of the excited state diminishes which is quantified by the longitudinal relaxation time $T_1$. (c) In addition, a loss of coherence of the ensembles occurs which scales with the transverse relaxation time $T_2$. To visualise this, an initial state at the equator has been chosen. (d) Effectively, both contributions impact the dynamics of the two-level systems.

longitudinal and transversal relaxation times turns out to be rather difficult since in most time-resolved spectroscopy methods, the measured dynamics underlie an entanglement of the loss of coherence $(T_2)$ and population decay $(T_1)$. Accordingly, it is important to understand the physical interpretation and the interplay of those two basic time constants.

To initialize the system, a short laser pulse creates electronic excitations. The electromagnetic wave generates a polarisation $P$ which is initially coherent with the light field. Due to interaction processes e.g. scattering, the coherence of the polarisation diminishes exponentially over time since a constant interaction with the surrounding 'bath' is presumed. The coherent part of the polarisation thus formulates as:

$$P_{coh} = P_0 \exp\left(\frac{-t}{T_2}\right).$$

(2.4)

Assuming that recombination of the excited particles, which is quantified by a recombination time $T_1$, is the only phase-destroying process, one can express the number of excitations $N(t)$ as:

$$N(t) = N_0 \exp\left(\frac{-t}{T_1}\right) \propto P(t)^2 = P_0^2 \exp\left(\frac{-2t}{T_2}\right)$$

(2.5)

since $N$ scales with intensity and consequently with $P^2$. This gives an upper limit for $T_2$:

$$T_2 \leq 2 \cdot T_1$$

(2.6)

Owed to the existence of so-called 'Pure dephasing' ($T_2^*$) which considers the loss of coherence without a concomitant loss of population, the relation between the relaxation times formulates as:

$$\frac{1}{T_2} = \frac{1}{2T_1} + \frac{1}{T_2^*}$$

(2.7)

In semiconductors, the most significant interactions that cause pure dephasing are phonon scattering, interactions with other quasiparticles or residual charges, as well as impurities and defects [Kli12]. A cartoon of those mechanisms is presented in figure 2.7(a) and (b). Exciton-phonon interaction facilitates energy and momentum relaxation. Since the CB levels of the $\Sigma$ valleys (often also termed as Q valleys) are equal or even lower in energy for bulk TMDCs, there exist several phonon modes that redistribute the exciton's constituents, transducing them to a momentum-dark exciton state [Car15; Cho17; Raj18]. A selection of the most important phonon modes in figure 2.7(c). The concrete impact of phonons on the carrier dynamics involving the $\Sigma$ valleys is discussed elaborate in chapter 4.2. In order to keep the loss of coherence and population at a minimum, temperature has to be low, the particle density and the number of dopants need to be very
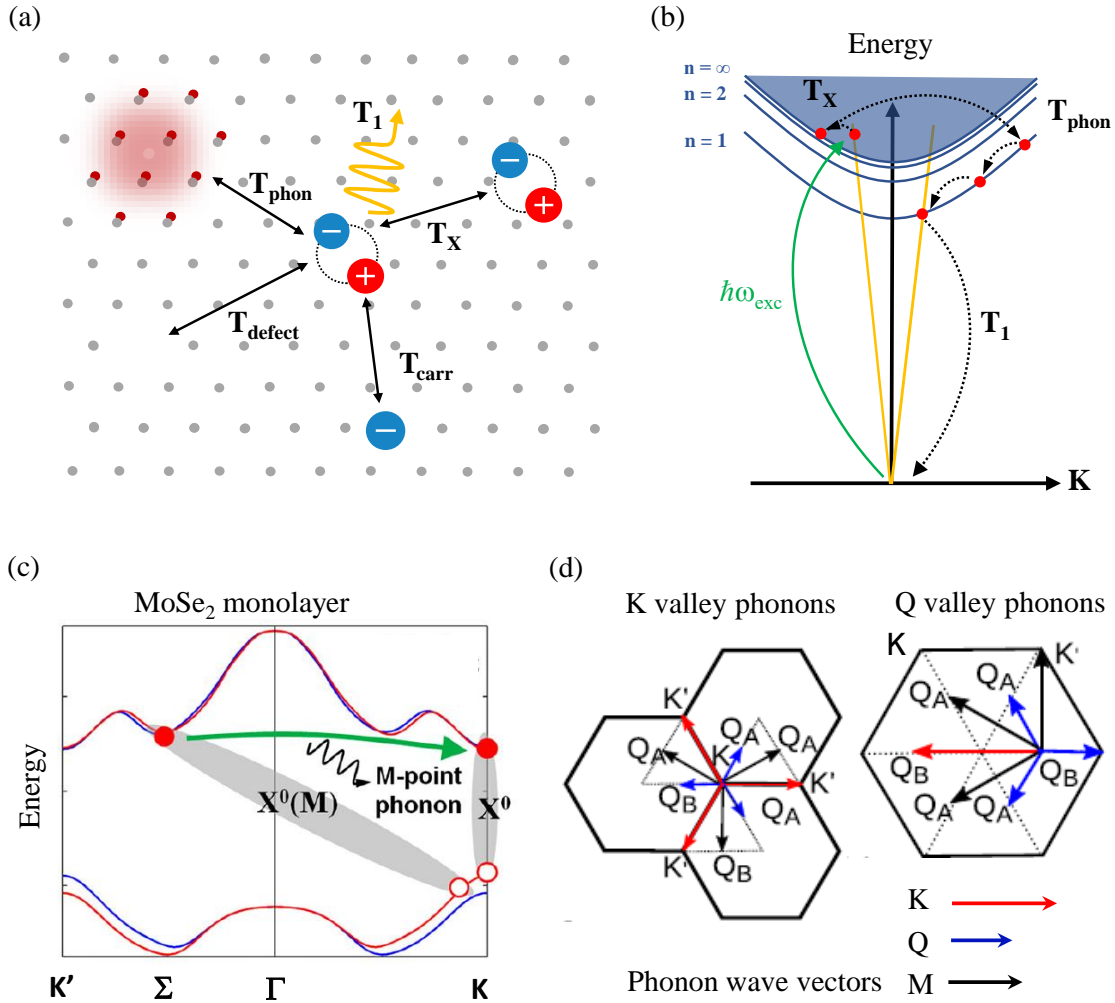
(a)

(b)



(c)

(d)



**Figure 2.7: Sources for loss of coherence and depopulation in TMDCs.**
(a) Cartoon of common interactions which destroy the exciton coherence (reproduced from [Wag23]). (b) Relaxation dynamics visualised in the exciton dispersion. Off-resonant excitation is followed by thermalisation, causing a distribution that exceeds the light cone. Relaxation is mostly mediated by phonons (adapted from [Kli12]). (c) Exciton-phonon interaction involving the $\Sigma$ valley. In TMDCs, the $\Sigma$ valley is energetically at the same level or even lower (multilayers) than the CB level of the K valleys. For $MoSe_2$, a longitudinal acoustic M-point phonon mode matches with the $\Sigma$-K transition, transferring the exciton's electron to the $\Sigma$ valley. Plot reprinted from [Cho17]. (d) In general, the existence of various zone-edge phonons make TMDCs prone to exciton-phonon interaction [Car15; Cho17; Raj18]. Here, $Q_A$ and $Q_{A'}$ denote the $\Sigma^{\pm}$ valleys, respectively. Image reproduced from [Hos15].

dilute and the sample has to be clean and free of defects. In the method chapter, it will be discussed how it is possible to access the $T_1$ and $T_2$ time by four-wave mixing experiments. There is a manifold of implications that result from $T_1$ and $T_2$. In particular, homogeneous line broadening $\Gamma$ can be derived by:

$$T_2 = \frac{2\hbar}{\Gamma} \tag{2.8}$$

This holds, given that all oscillators have exactly the same energy, since this formula describes the damping width of a harmonic oscillator that decays with $T_2$. If the oscillators' frequencies are slightly different due to disorder effects, i.e. following a Gaussian distribution, the dephasing time of the systems' polarisation $T_{deph}$ is shorter because the polarisation components of the individual oscillators soon average to zero. The loss of the coherent polarisation of such a system is linked to the width of the Gaussian distribution $\omega_{Gauss}$ and obeys the condition: $T_{deph} \cdot \omega_{Gauss} \approx 1$ [Kli12]. Nonetheless, the $T_2$ time can be accessed very accurately in inhomogeneously broadened systems as it will be discussed in the method section 3.2.3.

In addition to these theoretical considerations which are valid for a generic quantum mechanical ensemble of two-level systems, the enhanced Coulomb interaction does strongly impact the exciton coherence in TMDCs. The main driving force stems from long-range exchange interaction (LRX) between the constituent electron and hole which was introduced already for excitons in GaAs quantum wells [Mai93], giving rise to an additional efficient source of the exciton polarisation [Gla14; Zhu14; Hao16a]. Visually, an exciton can switch its valley by the virtual recombination and simultaneous generation of an exciton in the opposite valley (cf. 2.8(a)). This mechanism requires neither a change of momentum of an individual carrier nor its' spin to flip. In TMDCs, large excitonic binding energies and the concomitant high oscillator strengths of the optical transitions lead to an enhanced impact of LRX that is more than one order of magnitude larger compared to GaAs quantum wells and hence results in a comparatively fast exciton polarisation relaxation [Gla15]. Theoretically, the effect of long-range electron-hole exchange interaction can be treated in a $k \cdot p$ approach or equivalently in a pure electro-dynamical manner, considering an optically active exciton as a microscopic dipole oscillating at its resonant frequency. Therefrom emerges a longitudinal and transverse splitting of the bright exciton state which acts as an effective magnetic field $\Omega$ (cf. figure 2.8(b)), causing a mixing of the spin states and thus leads to decoherence of the exciton ensemble. The size of the splitting scales linearly with the exciton centre of mass momentum (COM) [Hao16a]. This process occurs on a
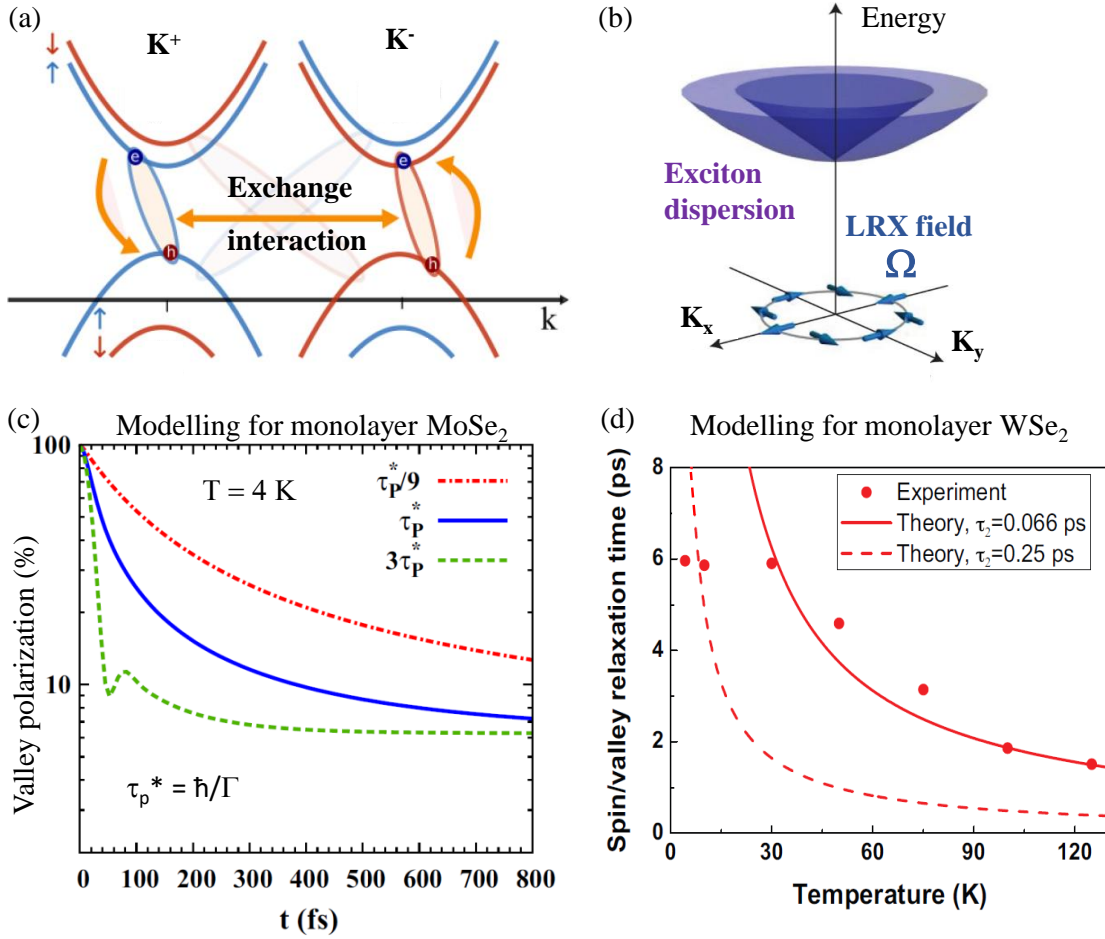
**Figure 2.8: Illustration of electron-hole long-range exchange interaction (LRX) and its time dynamics.** In TMDCs, LRX constitutes the major source for the loss of coherence. (a) Schematic interpretation of LRX. By a virtual recombination of an exciton residing e.g. in the $K^+$ valley, a simultaneous generation of an exciton in the opposite valley can occur without violating energy and momentum conservation (reproduced from [Sel19]). (b) LRX can be conceived as an effective in-plane magnetic field $\Omega$. Its orientation and magnitude depends on the excitons' centre-of-mass momentum $K_x$ and $K_y$ (adapted from [Hao16a]). (c) Modelling of the valley polarisation for MoSe$_2$, pumping resonantly on the A exciton transition. Different momentum relaxation times $\tau_p^\star$, which can be related to the exciton linewidth, are taken into account (calculations from [Yu14]). (d) Calculated valley relaxation times for two different momentum scattering times $\tau_2$ compared with time-resolved Kerr measurements of [Zhu14] as a function of temperatures. The valley relaxation time increases for augmented momentum scattering (plot from [Gla15]).

picosecond time scale which is shown in figure 2.8(c) and (d). As Yu et al. show, valley coherence increases for higher momentum scattering rates [Yu14], which is also observable in the work of Glazov et al. in (d) [Gla15]. The theoretical considerations of Hao et al. reveal analogue systematics [Hao16a]. This counter-intuitive

behaviour can be explained by a more frequent change of the excitons' momenta, e.g. by impurity scattering [Hao16a] or Coulomb scattering with resident electrons [Gla15] which reduces the effect of the time-averaged effective magnetic field $\Omega$. To clarify, the momentum scattering rate figures a measure of the distribution of the excitons' COM, but not the specific value of the COM itself. Regardless of the presumed momentum scattering rates, all models predict a subsequent more long-lived valley polarisation in the picosecond range which is attributed to residual excitons that possess a rather small COM and therefore experience fewer impact of LRX.

Concluding over this section, an exciton population can be modelled as an ensemble of two-level systems. Within this framework, the loss of coherence as the decay of population is considered. $T_1$ and $T_2$ quantify the respective processes. Owed to the excitons' extraordinary strong Coulomb interaction, LRX constitutes the main source for decoherence of excitons in TMDCs.

# Chapter 3

# Methods

## 3.1 Sample fabrication and characterisation

Within the last two decades that have passed since the exfoliation of graphene, several fabrication methods for the cleavage of layered van der Waals crystals, as the precise deposition of several (mono-) layers have been developed [Cas14; Pur18]. Nowadays, the state-of-the-art 'Hot pick-up' method introduced by Purdie et al. permits the full control of the stacking parameters while providing exquisite clean interfaces [Pur18]. Before, the more basic and robust 'all-dry viscoelastic stamping' method invented by Castellanos-Gomez et al. has constituted the prevalent approach to handle atomically thin layers [Cas14]. In the last view years, Chemical Vapour Deposition (CVD) growth has made large efforts to increase the quality of artificially grown monolayer crystals, allowing a deterministic and scalable production which presents an important step towards applications and industrial use of TMDC semiconductors [Par20; Kan22].

All of the here discussed samples have been manufactured in our research group. The samples have been characterised performing photoluminescence (PL) and reflectance (RC) spectroscopy. On the multilayer samples, only RC measurements have been conducted since PL is strongly quenched due to the indirect band gap. From atomic force microscopy (AFM) scans, the number of layers of the multilayer samples has been determined. Besides, a novel subsidiary method which allows for a precise in-situ determination of the sapphire substrate temperature in common 'Cold-finger' flow cryostats has been developed. This might be a valuable tool for all people working with sapphire as a substrate and is therefore presented in the last subsection.

### 3.1.1 Sample fabrication

The procedure of the sample fabrication follows in principle the suggestions as proposed by Castellanos-Gomez et al. [Cas14]. A detailed description of the exfoliation process and the transfer to the sapphire substrate can be found in my master thesis [Rai19]. Due to geometrical restrictions of the setup, samples with a size of at least 50 μm had to be manufactured. All monolayer samples have been encapsulated in hexagonal Boron Nitride (hBN) which is an insulating van der Waals material [Gei13]. hBN encapsulation has become a standard in TMDC sample fabrication in order to minimize dielectric disorder and hence narrowing the excitonic linewidths close to the homogeneously broadened limit [Cad17; Raj19; Rho19]. Moreover, it prevents the degradation of the sample since the encapsulation renders an air-tight coating [Hol20]. The multilayer samples were not encapsulated because the outer layers act as protecting layers. Degradation of those layers should marginally affect the excitonic landscape inside of the crystal since the signal arises from many layers. The CVD-grown monolayers have been provided by the group of Andrey Turchanin of the Friedrich Schiller University of Jena and assembled, following the 'Hot pick-up' method [Pur18].

### 3.1.2 Atomic force microscopy

Four years after the Nobel-prize rewarded invention of the scanning tunnelling microscope (STM) [Bin82], Binning et al. crafted the atomic force microscope (AFM), which could cope with the largest issue of STM, namely the prerequisite of a conducting sample [Bin86]. This technique enables the imaging of basically any type of surface with a spatial resolution on the angstrom regime. Since a few decades, AFM setups are commercially available and hence facilitate the analysis of nanostructures.

With regard to this work, AFM has been used to determine the thicknesses of the multilayer samples for the specification of the number of layers. The so-called 'Non-contact' scan mode has been applied where the cantilever tip operates in the attractive force regime of the interaction potential of surface and the tip atoms. Consequently, the sample surface is not demolished. The crystals are scanned at various edges. Therefrom, line-cut profiles have been extracted and analysed. The number of layers is calculated by dividing the obtained heights by the thickness of a single layer. The values for $MoSe_2$ and $WSe_2$ denote 6.45 Å and 6.48 Å, respectively [Coe87; Sch87]. Microscope images, AFM scans and height profiles of the investigated multilayer samples are shown in figure 3.1. The $WSe_2$ multilayer

sample was found to consist of approximately 160 layers and the MoSe$_2$ sample of 84 layers.

(a)



101 nm / 0.648 nm ≈ **160 layers**

(b)
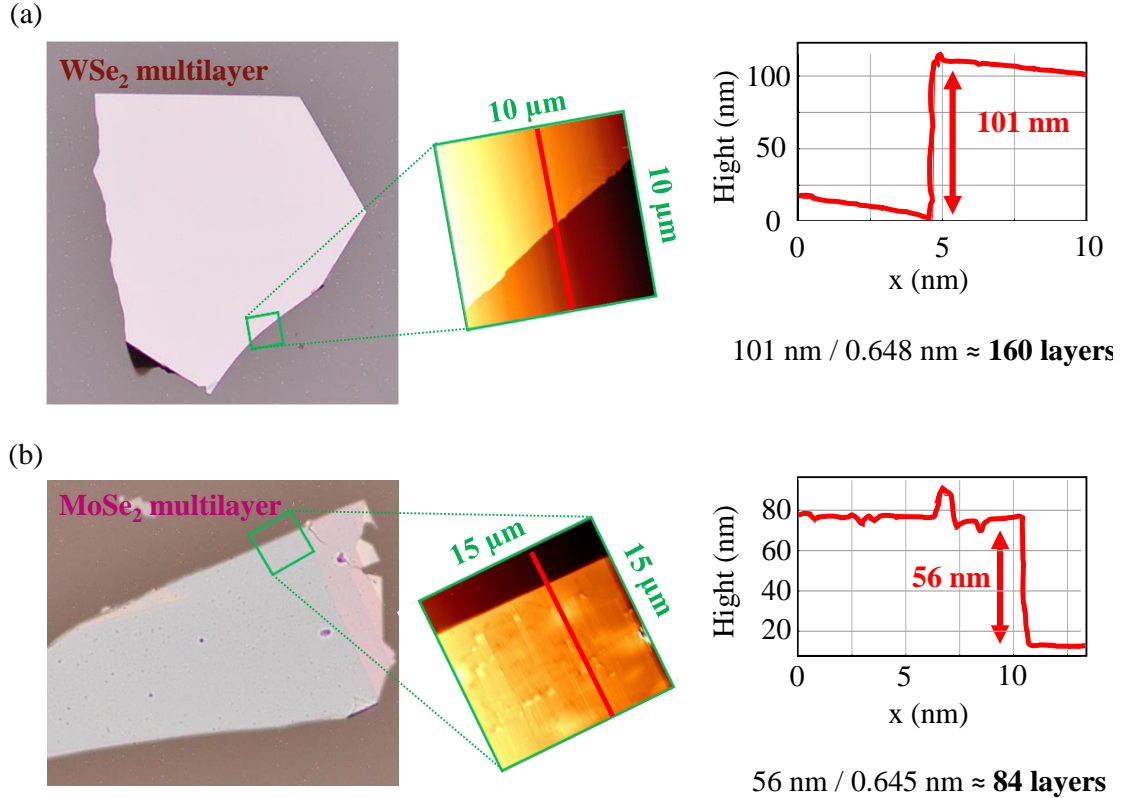


56 nm / 0.645 nm ≈ **84 layers**

**Figure 3.1: Light microscope images and AFM scans to determine the number of layers.** (a) WSe$_2$ multilayer on sapphire. The AFM scan evidences a flat surface. From the height profile of the edge, the number of layers has been determined to be about 160. (b) MoSe$_2$ multilayer on sapphire. The AFM scan reveals some adsorbents as well as dust particles (also visible as violet grains in the optical image) on top of the samples. The sample was found to consist of approximately 84 layers.

### 3.1.3 Photoluminescence spectroscopy

Photoluminescence (PL) spectroscopy represents one of the basic spectroscopy methods for the investigation of direct semiconductors. Carriers are excited above the band gap and subsequently relax to the lowest energy states. The spectral analysis of the emitted light of the radiatively decaying photo carriers provides information about the optical bandgap. In monolayer TMDCs, the PL is characterised by rich excitonic transitions [Cad17; Wan18]. The peak positions and the according linewidths provide information about the specific excitonic transitions. Furthermore, the appearance of charged excitons, termed as 'trions', reflects the amount of dopants in the materials [Ros13]. Overall, PL spectroscopy provides

*Chapter 3 Methods*

valuable information about the spectral position of the bright excitonic transitions and the sample quality.

Figure 3.2 displays microscope images of the examined monolayer samples and the corresponding PL spectra. The WSe₂ sample in (b) has been fabricated by our Bachelor and Master students Simon Feldl and Petter Marzena. The CVD-WSe₂ sample in (c) has been manufactured by our Master Student Niclas Maier. PL scans have been conducted using a microscope lens to focus the excitation laser (532 nm) on to the sample with a spot size of 2 μm. All samples have been cooled down in a cold finger flow cryostat to nominally 4 K. The effective temperature has been determined via the 'Ruby peak' method (cf. subsection 3.1.5) to be smaller than 20 K, 15 K and 5 K for (a), (b) and (c), respectively. The $A_{1s}$ exciton transition can clearly be assigned to the peak structure in the PL spectra by comparison with literature [Cad17]. The other peaks are attributed to other excitonic complexes (e.g. trions, biexcitons or charged biexcitons), phonon replicas as well es defects and localised charge carriers [Ber13; Sid17; He20]. Note that hBN encapsulation leads to a redshift of several tens of meV compared to bare monolayers, arising from the distinct dielectric environments [Cad17]. In addition, it has to be mentioned that the peak structure as well as the spectral position of the peak and the respective intensities vary significantly with the spatial position on the samples. This is reasoned by dielectric disorder (i.e. bubbles and dust) and strain effects which is hardly avoidable in such large samples. Concerning the energy of the $A_{1s}$ exciton, shifts of $\pm$ 5 meV occur. The effective linewidth is certainly broader than the exemplary PL spectra, taken with a microscope setup, imply because the sample is illuminated over a comparably large area with 50 microns spot diameter in the pump-probe experiments below, which is owed to the restrictions of the cryostat. Thus, the excitonic transitions are inhomogeneously broadened. Apart from that, a drastic difference in PL intensity shows up, comparing intensities. The scaling factors in (a) and (c) are given with respect to (b). The rich emission of PL in MoSe₂ is based on the fact that the lowest energy state is a bright state whereas in WSe₂, the lowest state is dark, acting as a sink and additional decay channel. The rather poor PL emission of the CVD-grown sample is most likely owed to the CVD growth process. Interestingly, the rich peak structure at lower energies, which is present in the exfoliated sample is absent in the CVD sample. Here, only the trion is still present.
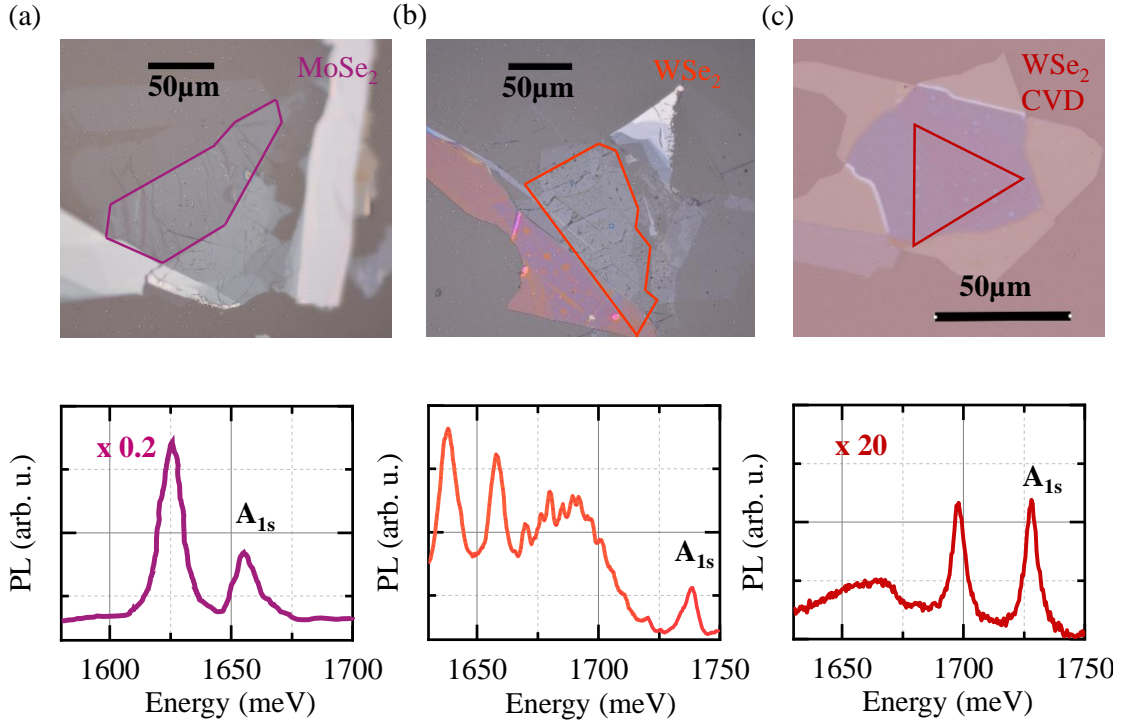
28

**Figure 3.2: Microscope images and representative PL spectra of the investigated monolayer TMDC samples.** All samples are prepared on sapphire (Al$_2$O$_3$). In each spectrum, the peak of the A$_{1s}$ exciton is remarked. (a) Exfoliated monolayer MoSe$_2$ encapsulated in hBN. The most prominent peak can be attributed to the trion. (b) Exfoliated monolayer WSe$_2$ in hBN. The diffuse peak structure at lower energies arise from charged (bi-)excitons and phonon replicas [He20]. (c) CVD-grown monolayer WSe$_2$ picked up from the host substrate and sandwiched in hBN. The second peak 30 meV below the A exciton probably corresponds to the trion. The scaling factors in (a) and (c) are given with respect to (b). Temperature was below 20 K for all samples.

## 3.1.4 Reflectance spectroscopy

The beginning of spectroscopy can be traced back to Sir Isaac Newton who split up the sun light into its colour components. Since then, spectroscopy evolved and became a fundamental branch in experimental physics, exploring interaction between light and matter. Moreover, the studies of black body radiation or of the hydrogen Rydberg series paved the way for the development of quantum mechanics.

Nowadays, the prevalent spectroscopic method figures absorption spectroscopy which reveals the optical transitions that take place in a specific material. A drawback of this approach is the prerequisite of at least partial transparency of the sample and its substrate. From a technical view, it is much more convenient for many experiments to analyse the optical response of the medium in reflectance

instead. Physically, this is equivalent because transmission and reflection are connected by the Kramers-Kronig relations [Kro26; Kra27]. These relations imply that the real- and the imaginary part of the complex dielectric function (i.e. reflection and absorption) depend on each other. Consequently, the effects of absorption have to be observable as well in reflectance. An advantage of reflectance spectroscopy is the accessibility of optical transitions that are higher in energy and consequently do not contribute in luminescence measurements. Furthermore, it enables to determine the relative strength of different transitions which can be quantified by the oscillator strength [Kli12].

Practically, this is achieved by focusing the light of a white-light-lamp through a microscope lens onto the sample and analysing the reflected light $R$ by a spectrometer. By subtraction of the reflectance spectrum of the substrate $R_0$, the transitions become distinctive. In order to compare the different strengths of various oscillators, it is crucial to weight the entire spectrum correctly since the emission of the light source and the sensitivity of the spectrometer is not constant over the whole spectrum. This issue can be corrected by dividing subtracted spectra by $R_0$. As there might be some back light illumination or dark current on the CCD, it is reasonable to include the background spectrum $R_B$ in the denominator:

$$\frac{\Delta R}{R} := \frac{R - R_0}{R_0 - R_B} \tag{3.1}$$

In principle, reflection contrast measurements are already sufficient to determine the approximate energy position of an oscillator. However, things become more complex when the investigated sample consists of a stack of multiple materials with various thicknesses and diverse dielectric functions, i.e. different refractive indices and absorption coefficients. Thereby, the incident light is refracted and partially reflected back at each layer interface. Additionally, interference comes into play. In order to take all those effects into account, a transfer matrix approach is applied to the reflectance contrast. Within this ansatz, each layer of the structure is considered with a specific matrix that comprises the parameters of reflection, transmission and absorption. By matrix multiplication, the system's matrix can be obtained. For the material layer of interest, its dielectric function $\varepsilon_r^*$ of is modelled by $n$ Lorentzian oscillators:

$$\varepsilon_r^* = \varepsilon_{back} + \sum_n \frac{f_n}{E^2(\omega) - E_n^2 - iE(\omega)\Gamma_n} \tag{3.2}$$

The dielectric background, i.e. the dielectric constant in absence of the oscilla-
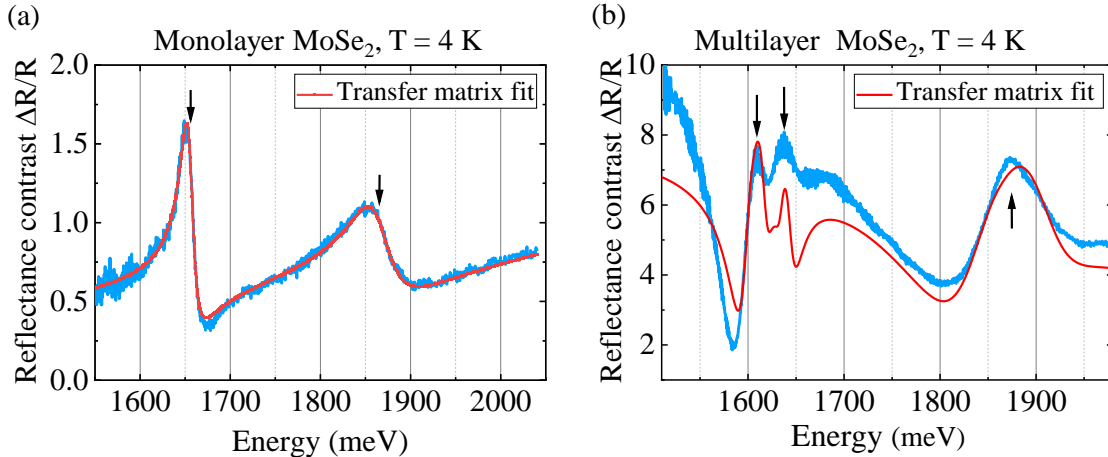
**Figure 3.3: Exemplary reflectance contrast measurement on MoSe₂ modelled by a transfer-matrix approach.** The red curve gives the fit of the reflectance contrast (blue line) by the transfer matrix model. Black arrows indicate the peak position of the Lorentzian oscillators that are obtained by the fit. (a) Encapsulated monolayer MoSe₂. The fitting function of the transfer matrix model comprises two Lorentzian oscillators which can perfectly describe the acquired RC data. (b) Multilayer MoSe₂. Here, the fitting function consists of three oscillators. While the shape of the RC spectrum can be modelled still reasonably, the amplitudes deviate.

tors is denoted by $\varepsilon_{back}$. The parameters of the Lorentzians are the weights of the oscillators $f_n$ which are proportional to the associated oscillator strengths, the resonance energies $E_n$ and the broadening $\Gamma_n$. From this function, the according transfer matrix and the heron based reflectance contrast spectrum is implemented and fitted to the experimental data, following the restrictions given by the stack of the involved materials. Since this fitting function is literally complex, comprising a multitude of material parameters as the dielectric functions of all involved materials, layer thicknesses etc., it is convenient to use an automated fitting algorithm. Based on the concept of S.J. Byrnes [Byr16], this has been realised by Dr. Jonas Zipfel from the group of Prof. Alexey Chernikov who kindly provided their Matlab® code to us. A much more detailed description of the transfer matrix fitting programme can be found in the dissertation of Jonas Zipfel [Zip20]. As a result of this evaluation, the fitted parameters of the individual Lorentzian curves are obtained which indicate the exact spectral positions of the oscillators. Especially for the bulk samples, this tool is vital to interpret the intricate reflectance spectra. Exemplary reflectance measurements evaluated with the transfer matrix approach are presented in figure 3.3. For monolayer samples, the modelled functions match the measured RC data perfectly over a large energy range. For multilayer samples, fitting gets more delicate. Many parameters, as the sample
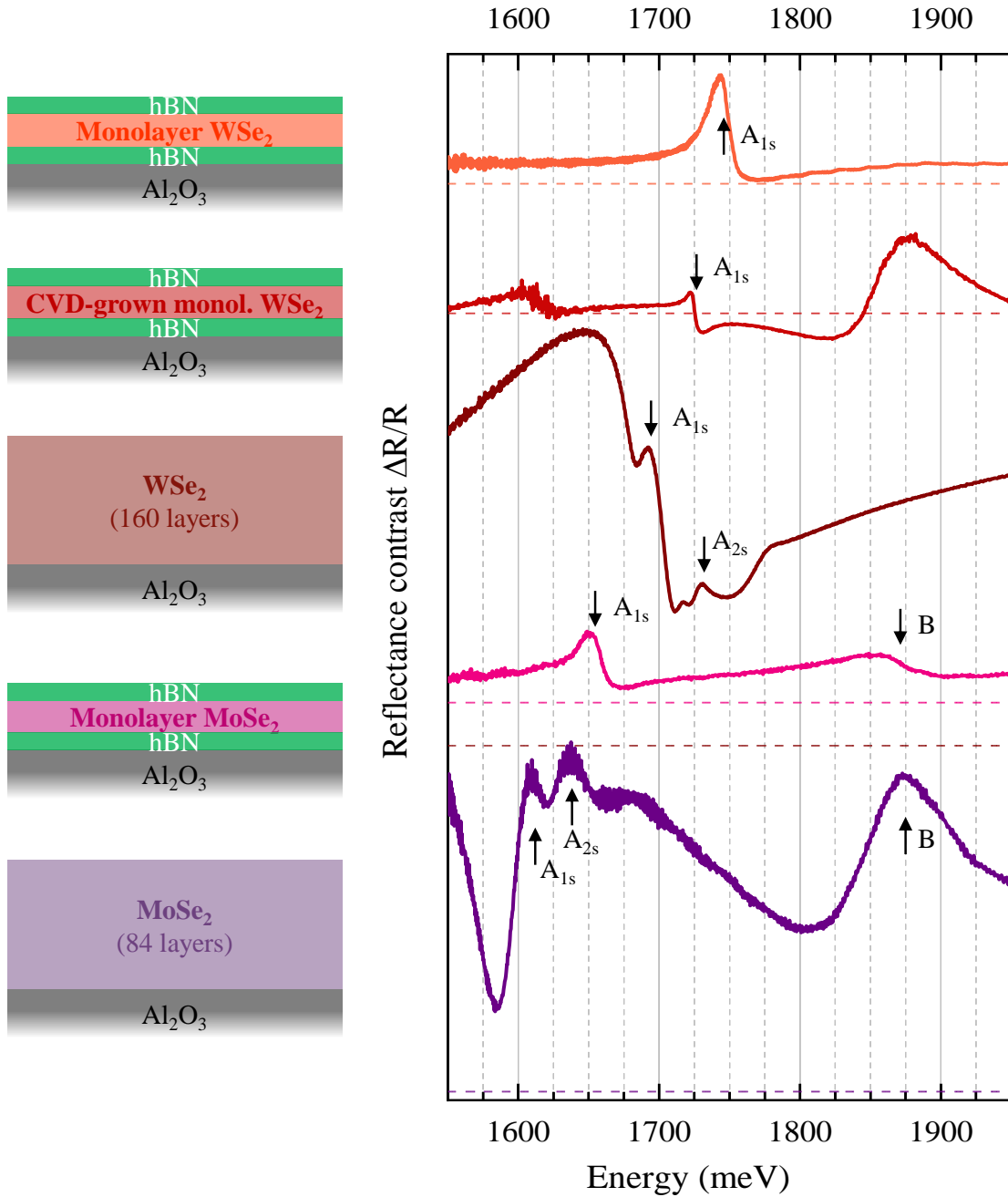
**Figure 3.4: White-light reflectance contrast measurements of the investigated samples.** The schematic cartoons on the left represent the composition of the regarded sample. All samples are prepared on transparent sapphire substrates ($Al_2O_3$). The substrate temperature in all RC measurements was below 20 K as derived from the intensity ratio of the ruby lines (cf. section 3.1.5). The dashed lines denote the zero levels. The vertical black arrows indicate the peak positions of the Lorentz oscillators obtained by a transfer-matrix-model fit. For the monolayer samples, the dominant features can clearly be assigned to the respective $A_{1s}$ exciton transitions. For the multilayer samples, the RC spectra appear more intricate. The according fits reveal the appearance of a second, less pronounced oscillator that can be ascribed to the $A_{2s}$ exciton transition.

thickness and the dielectric background, need to be kept fixed in order to resemble the shape of the RC properly. Reasons therefore are enhanced interference effects that come into play when the layer thicknesses approach the same order of magnitude as the wavelength of the incident light [Byr16]. In figure 3.4, the reflectance spectra of the here investigated samples are presented. The dominant oscillator in monolayer $WSe_2$ ranges at an energy of 1746 meV which can be assigned to the $A_{1s}$ exciton. For monolayer $MoSe_2$, two oscillators can be identified, ranging at 1695 meV and 1866 meV which can be ascribed to the $A_{1s}$ and the $B_{1s}$ exciton, respectively. Note that for monolayer $WSe_2$, the B exciton is outside the displayed energy range. Concluding over the monolayer samples, the identification of the excitonic transitions is in very good agreement with the experimental findings in literature [Aro15; Cad17; Niu18].

Turning towards the multilayer samples, the excitonic resonances undergo a redshift with respect to the monolayers. Moreover, the energy separation between the $A_{1s}$ and $A_{2s}$ exciton transition is reduced because of stronger dielectric screening [Aro17]. The energy positions of the $A_{1s}$ transition in the bulk samples coincide very well with the experimental findings of Arora et al. [Aro18]. In the calculations of Paulo E. Faria Junior [Rai22] that are included in this thesis, binding energies of 29.9 (9.1) meV for the $A_{1s}$ ($A_{2s}$) exciton in $WSe_2$ and 41.9 (10.1) meV for the $A_{1s}$ ($A_{2s}$) exciton in $MoSe_2$ are obtained. These values match the experimental findings very well and thus are a strong indication that the transitions above the $A_{1s}$ exciton can be assigned to the $A_{2s}$ exciton.

Concluding this section, the excitonic resonances can be identified using a matrix transfer fitting approach. The spectral position of the ascribed exciton states are corroborated by theoretical modelling.

### 3.1.5 Temperature determination from the ruby peaks in sapphire substrates

In mineralogy, sapphire ($Al_2O_3$) renders the host material for many well-known gemstones. The shining colours of blue sapphire or ruby originate from impurities in the crystal lattice. Sometimes it occurs that elements of the same group, i.e. with a similar configuration of valence electrons replace some of the predominant constituents. Regarding $Al_2O_3$, aluminium atoms are scarcely substituted by chromium atoms (Cr). These so-called 'colour centres' render a trapping potential, giving rise to discrete energy levels that are very sharp in energy. In physics, ruby has become famous, serving as the medium for the very first laser [Mai60]. In spectroscopy, temperature affects the spectral position and the broadening of

the investigated transition. In addition, phonon interaction comes into play in solids. Thus, for most experiments, low temperatures and a precise determination thereof is mandatory. Nowadays, cold-finger flow-cryostats are broadly used in spectroscopy setups providing temperatures of a few Kelvin. To fix the sample substrates to the metallic base of the cold finger cryostat, FixoGum glue by Marabu GMBH is broadly used. Originally developed for collage work in arts, the glue remains flexible and can be removed easily without residuals. Transparent samples are fixed on every corner with a dot of glue on the base to which the temperature sensors are coupled. Figure 3.5(a) depicts a cartoon of the sample installation in a flow cryostat. Cooling is achieved via heat conduction. For this installation, the thermal bottle neck constitutes the gluing connection. Consequently, the effective temperature of the substrate remains vague and is probably higher than the monitored values, taking into account that the exciting laser constantly heats the sample. To overcome the issue of the lacking knowledge about the effective temperature on the sample, it is possible to use the emission lines of the residual chromium impurities in sapphire as a thermometer. Generally, every PL spectrum recorded with sapphire as a substrate exhibits these very bright and narrow-band emission peaks which are referred to as ruby lines and account for the reddish colour of ruby. A typical PL spectrum is presented in figure 3.5(b). At closer consideration, two lines become distinguishable which are labelled as $R_1$ and $R_2$. Even in industrially grown sapphire crystals, chromiums atoms occasionally occur, substituting some lattice sites of the aluminium atoms since both atomic species posses the same configuration of valence electrons and consequently equally fit the ionic bindings of the crystal (cf. figure 3.5(c)). However, the larger $Cr_3^+$ ions have a different orbital composition compared to aluminium. The lowest-energy state of such an embedded Chromium atom denotes the $2^E$ state which is a doublet state, i.e. a composite quantum state with an effective spin of $1/2$. Whilst the level spacing is owed to the coupling of spin and crystal field, the population of these is ruled by thermodynamics. These fluorescence peaks emit at 1788.5 meV and 1792.2 meV, respectively (694.3 nm for $R_1$). The averaged energy difference $\Delta E$ denotes 3.64 meV. Converting $\Delta$E to temperature by $\Delta E = k_B T$ yields a corresponding temperature of T = 42 K. Consequently, the change in relative population becomes most apparent for temperatures below this value. The occupation of the lowest state $N(E_1)$ relative to the higher state $N(E_2)$ which is thermally populated writes as [Sig18]:

$$\frac{N(E_2)}{N(E_1)} = \frac{g_2}{g_1} \exp\left(-\frac{E_2 - E_1}{k_B T}\right) \tag{3.3}$$

(a)



$\hbar\omega_{exc}$

T = ?

Al$_2$O$_3$

FixoGum

Cold finger cryostat
T = 4 K

(b)



PL intensity (arb. u.)

R$_1$

R$_2$

1780 1785 1790 1795 1800
Energy (meV)

Ruby
lines

PL WSe$_2$

1650    1700    1750    1800
Energy (meV)

(c)



Al atom

O atom

z
y   x

(d)



Energy

E$_2$

E$_1$

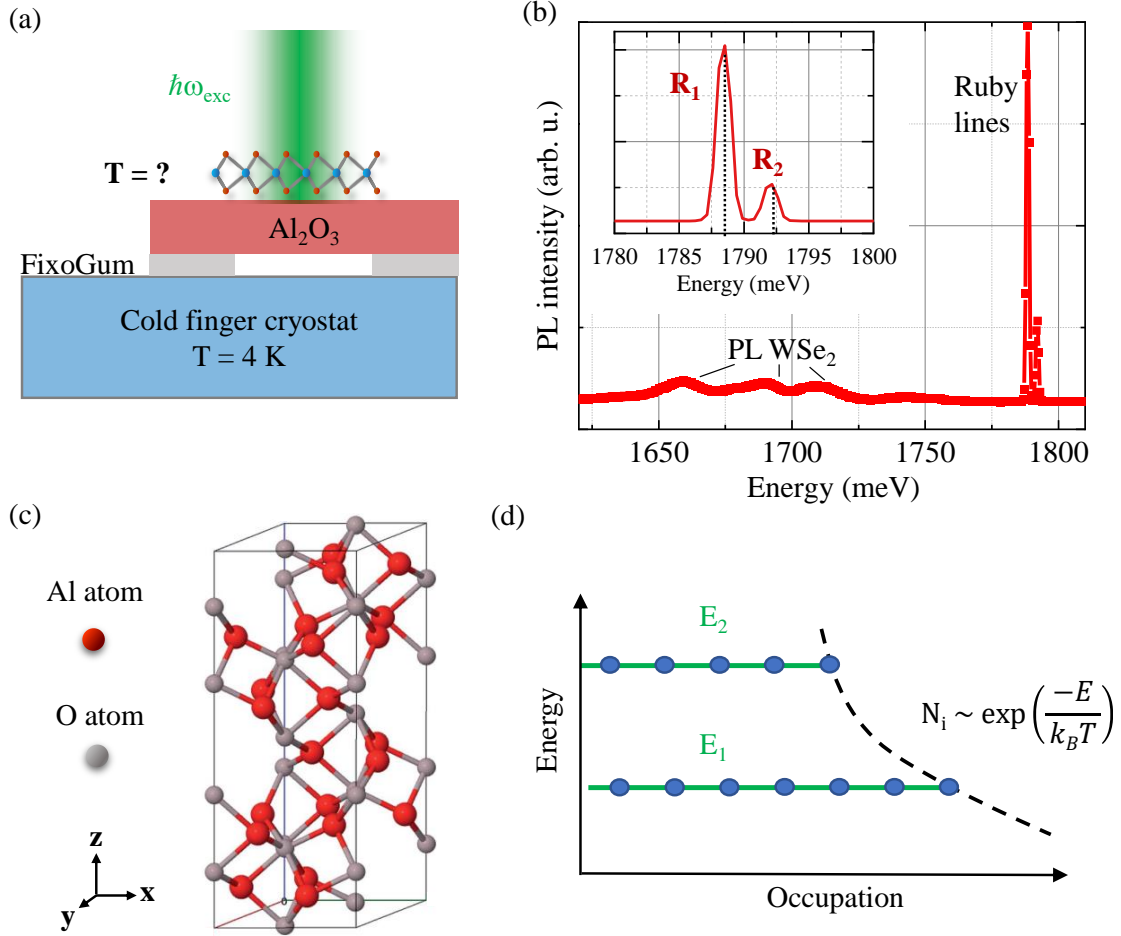$N_i \sim \exp\left(\dfrac{-E}{k_B T}\right)$

Occupation

**Figure 3.5: Temperature determination of the sapphire substrate from the relative intensities of the ruby lines.** (a) In cold-finger flow cryostat, transparent sample substrates are broadly mounted with FixoGum glue on the metallic base of the cryostat which is cooled down to 4 K by liquid helium evaporation. The glued interface figures the bottle neck of the heat transfer. Thus, the temperature on the sample remains illusive as the incident light heats up the sample. (b) Exemplary PL spectrum of monolayer WSe$_2$ at low T. The shallow peaks correspond to the TMDCs' PL emission whereas the bright peaks at higher energies originate from chromium impurities entitled as ruby lines, R$_1$ and R$_2$, respectively. (c) Hexagonal unit cell of sapphire ($\alpha$ - Al$_2$O$_3$). Also industrial grown sapphire contains some residual chromiums atoms that substitute some lattice sites of the aluminium atoms (reproduced from [Pei14]). (d) Thermally populated two-level system. In thermodynamic equilibrium, the population N$_i$ of the levels $i$ obey the Boltzmann distribution. Accordingly, the effective temperature of the sapphire can be derived from the ratio of R$_1$ and R$_2$.

Here, $g_2$ and $g_1$ denote the degeneracies of the corresponding states. Apparently, the relative population of both states is a function of temperature:

$$T \propto \frac{E_2 - E_1}{k_B} \log\left(\frac{N(E_2)}{N(E_1)}\right)^{-1} \tag{3.4}$$

35

Further on, it is presumed that the relative population can be approximated by the peak ratio of the $R_1$ and $R_2$ ruby peaks. This implies that the degeneracies are presumed to be equal and that the radiative recombination is a direct measure of the populations, i.e. the oscillator strengths are identical. It turns out that this is not entirely true but can be adapted by the introduction of a scaling factor. To start, the peak ratio is plotted against the temperature T interpreting the $\propto$ as $=$ in equation 3.4 (cf. figure 3.6(a), dotted line). A scaling factor $a$ is introduced
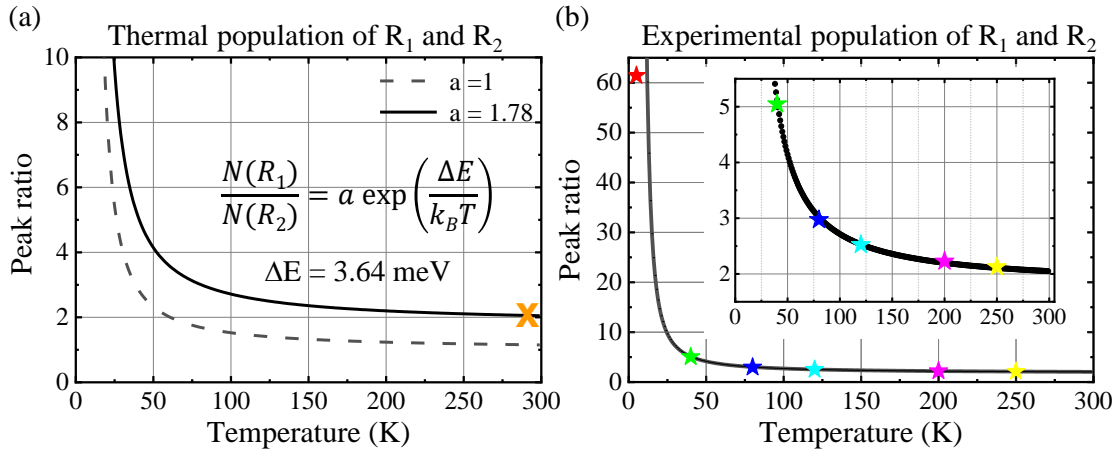


**Figure 3.6: Temperature as function of the ratio of the ruby $R_1$ and $R_2$ peaks.** (a) Taking the height of the peaks as a direct measure of the populations of $R_1$ and $R_2$, temperature can be deduced thereof since the ratio of thermally distributions scales with the Boltzmann factor. The energy difference between the both levels denotes 3.64 meV. The dotted line assumes equal degeneracies (a=1). Apparently, it does not coincide with the experimentally found average value of the peak ratio for T = 300 K (orange x). Empirical calibration can be achieved by introducing a scaling factor $a$ which satisfies previous condition. (b) In order to verify the calibration of the function, the sapphire was mounted with heat-conducting paste to the cryostat ensuring excellent thermal coupling. The peak ratios that have been extracted from the PL data at different temperatures (monitored by the cryostat) reveal an excellent agreement with the calibrated function. At 5 K, the $R_2$ peak has completely vanished.

which is fitted such that it matches the experimentally extracted average value of the peak ratio at 300 K. The introduction of this factors is reasonable since it empirically incorporates the unknown parameters of the $R_1$ and $R_2$ transition such as degeneracies and differences in oscillator strengths. The explicit function of the peak ratio $R(T)$ with all parameters included is hence given by:

$$R(T) = 1.78 \exp\left(\frac{42.24\ \text{K}}{T}\right) \tag{3.5}$$

In order to verify the values that are predicted by the upper formula, PL spectra were recorded at different nominal temperatures (i.e. output of the cryostat's temperature sensor). For this purpose, the sapphire was connected to the base of the cryostat with a thin film of heat-conductive paste all over the surface. Here, nearly perfect cooling can be assumed in contrast to the FixoGum gluing connection which is only partially applied at the substrate corners. The extracted peak ratios for different nominal temperatures are presented in figure 3.6(b). The temperatures determined from the peak ratio and the corresponding nominal temperatures reveal an excellent agreement. Especially for temperatures below 100 K, the peak ratio renders an accurate thermometer with an estimated accuracy of $\pm$ 5 K. By revisiting older PL spectra, the temperature retrieved from the peak ratio has been found to be several tens of Kelvin higher than the cryostat indicated.

At this point, it has to be mentioned that an enquiry of literature delivers various reports on temperature measurements involving the ruby lines [Gib99; Win01]. However, in these articles, temperatures at ambient conditions are considered. Therefore, the shift of the ruby lines has served as a measure of temperature. Moreover, the shift of the ruby lines has established to be used as a calibration method for high pressure experiments [Bar73]. Apart from that, the here presented method to determine the substrate temperature in flow cryostats, exploiting the relative height of the ruby peaks, has been developed in the scope of this thesis with the support of Dr. Johannes Holler and Dr. Sebastian Bange.

Summarising over this section, it is found that the effective temperature on samples investigated in usual cold-finger cryostats may be much higher than pretended by the cryostat sensors. In sapphire, evaluating the height ratio of the two ruby lines is a powerful and simple approach to precisely determine the effective sample temperature, especially in the range of 30 - 100 K. Since the emission of the ruby lines is intrinsically implemented on every recorded PL spectrum, it is a minimal effort to extract the temperature. Moreover, PL data from ancient scans can be revisited and checked, if the temperature has been indeed as low as indicated.

## 3.2 Time-resolved spectroscopy

In traditional spectroscopic methods, such as absorption or emission spectroscopy, the system under study is probed by a continuous light source. While these techniques provide valuable information about the electronic and vibrational properties of solids and molecules, they lack the ability to capture the dynamics of transient states and processes occurring on ultrafast timescales. Modern electronics as for instance avalanche photodiodes are able to monitor events down to the

sub-nanosecond time regime. This limit is imposed by the inertia of the electrons and the concomitant problems of noise and heating, restricting the clock rates of electronic devices. In time-resolved pump-probe spectroscopy, the issue of ultra-fast detection is overcome, utilizing various ultra-short laser pulses whose time delays can be precisely controlled by altering the optical path lengths of the respective pulses. For instance, it takes 1 fs for a light pulse to travel 0.3 μm additional path. As the length of the optical paths can be controlled very accurately, time resolution is hence limited only by the laser pulse duration. With the development of tunable ultrafast lasers [Ipp72; For81], as for example the Ti:Sapphire laser [Aus93], its colour can be adjusted to a specific wavelength, allowing a selective excitation of particular states.

The basic concept is realised in a pump-probe scheme. A first, a so-called 'pump' pulse excites the system of interest. The subsequent 'probe' pulse, which follows after a controllable time delay, interacts with the excited or modified state, generating a spectroscopic signal that carries information about the system's temporal evolution. By varying the time delay between the pump and probe pulse, a detailed temporal profile of the excited state and thereby its relaxation dynamics can be obtained. The temporal resolution on a femtosecond timescale enables the investigation of fundamental processes, such as electron dynamics, molecular conformations, and chemical reactions. Regarding solid-state physics, pump-probe spectroscopy has become an indispensable tool to investigate carrier lifetimes and their energy- and momentum distribution, as well as spin- and phonon dynamics [Kli12; Dem13]. Considering TMDCs, the exciton and valley dynamics occur on a pico-second time scale, rendering ultra-fast pump-probe spectroscopy as the preferred method to access this regime [Wan18].

In the scope of this thesis, carrier lifetimes from common transient differential absorption experiments are combined with 'Time-resolved Faraday ellipticity' (TRFE) experiments. In addition, 'Time-integrated four-wave mixing' (TI-FWM) experiments have been conducted in order to draw a complete picture of the underlying exciton dynamics which in many aspects still constitutes 'terra incognita' for multilayer samples and more complex heterostructures.

## 3.2.1 Pump-probe spectroscopy

The pump-probe technique represents the 'classic' of ultrafast spectroscopy methods. Time resolution is achieved by splitting up an ultra-short laser pulse into two and delaying one of them by introducing additional optical path way via a mechanical stage that can be controlled on a sub-micron scale. The typically much

stronger pump pulse generates a population which evolves in time. The second pulse (probe) interacts with the excited system. Due to the residual population, a so-called 'bleaching' of the considered transition occurs. Consequently, the probe pulse interacts weaker as with the unperturbed system. The specific polarisation of pump and probe pulse and the detection scheme allow to specify weather transient differential transmission, Faraday rotation/ellipticity or four-wave mixing is explored.

A schematic representation of the pump-probe principle is shown in figure 3.7(a). The light source for all pump-probe experiments is a passively mode-locked Ti:sa laser with an optical output power of 1 W, emitting 80 millions pulses per second ($\Gamma_{Rep} = 80$ MHz) that have a duration of approximately 100 fs. By scanning the mechanically introduced pump-probe delay, the acquired values can be plotted as a function of the delay time $\Delta$t. The displacement $\Delta x$ accounts for a time delay of $\Delta t = \frac{\Delta x}{c}$. For every time delay, the signal of the probe is acquired for 0.3 s. Thus, the obtained value reflects no single-shot measurement but the average of millions of pulses with the same time delay. Therefore, the pulse trains can be regarded as beams. For transient differential transmission, which is also often termed as 'pump-probe', the change in transmitted intensity $\Delta$T/T of the probe beam as a function of time delay is detected. The recorded signal is directly proportional to the temporal evolution of the population created by the pump pulse. For signals that are much more long-lived than the pulse duration, the data can be fitted with a multi-exponential decay. In many occasions, a mono-exponential fit matches the data, implicating a uniform decay mechanism. Exemplarily, a transient differential transmission measurement on monolayer $WSe_2$ is shown in figure 3.7(b). If multiple decay mechanisms contribute, a multi-exponential fit must be applied to model the dynamics.

A lock-in amplifier is used to purify the signal and remove contributions that oscillate with other frequencies as well as DC components. For this purpose, pump- and probe beam are modulated at two different frequencies by an optical chopper with distinct chopping wheel spacings for the specific beams. In order to be sensitive to a signal that is caused by both beams, it is convenient to process the signal in the lock-in either at the difference or sum frequency of both. Since the DC background noise is removed more efficiently at higher frequencies, the sum frequency is favoured and set as reference signal for the lock-in amplifier. A detailed map of the complete setup is presented in figure 3.8. The here depicted setup is valid for all further pump-probe methods because the particular arrangement for Faraday and four-wave mixing experiments can be realised by altering the polarisation optics and the detection scheme.
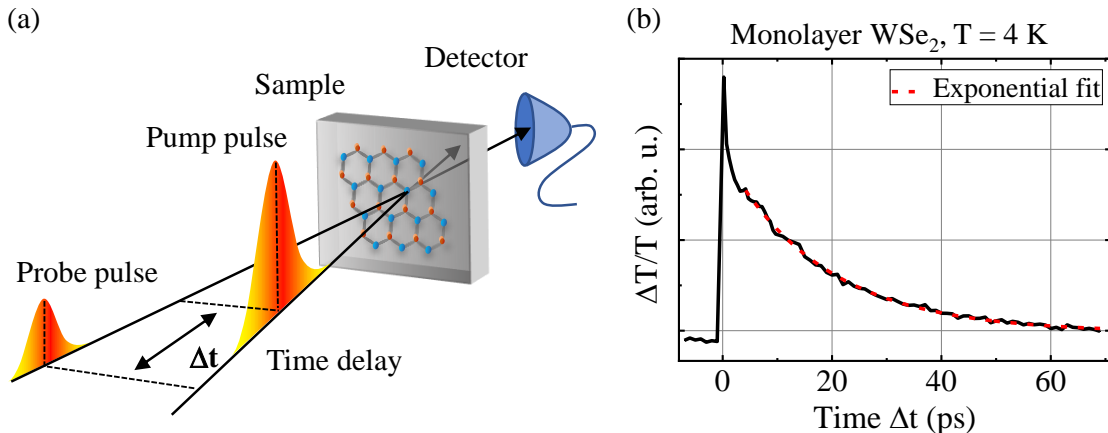
(a)

(b)



**Figure 3.7: Principle of pump-probe detection.** (a) Schematic representation of a pump-probe experiment. A strong pump pulse excites the transition of interest. The probe pulse, which follows the pump pulse after a controllable time delay, interacts with the excited system, carrying the spectroscopic signal. (b) Exemplary transient differential transmission signal of monolayer WSe₂. The intensity of the probe pulse is recorded for different time delays and subsequently plotted for every specific time delay, resulting in a time-resolved mapping of the population dynamics. Basically, the data can by analysed by applying a mono-exponential fit.

Moreover, it is essential to be conscious of the carrier densities that are generated at certain laser powers. Exciton-exciton interactions come into play at higher densities, culminating in the so-called Mott-Regime where densities are so high that the distance between the excitons is in the same order of magnitude as their excitonic Bohr radius. In this regime, the constituents of the exciton interact mutually strong with the surrounding particles. The exciton as a distinctive particle does not exist any more [Kli12]. For TMDCs, the Mott regime sets in at densities around $3 - 10 \cdot 10^{12}$ cm$^{-2}$ [Ste17]. In order to investigate pure excitonic effects, it is vital to excite only moderate excitons densities. To ensure this, absorption measurements have been performed directly within the split coil cryostat. For this purpose, the intensities of the laser beams are measured after having passed through the cryostat when being aligned to maximal pump-probe signal, and second, when passing only through the substrate next to the sample. The difference of both intensities yields the absorbed power $P_{abs}$. Therefrom, the density of photo-excited excitons $n$ can by obtained by:

$$n = \frac{P_{abs}}{\Gamma_{Rep}/2 \cdot E_X \cdot A_{pulse}} \tag{3.6}$$

$\Gamma_{Rep}$ denotes the repetition rate of the laser. The diameter of focussed laser beams that account for the area of the laser spot $A_{pulse}$, which has been determined
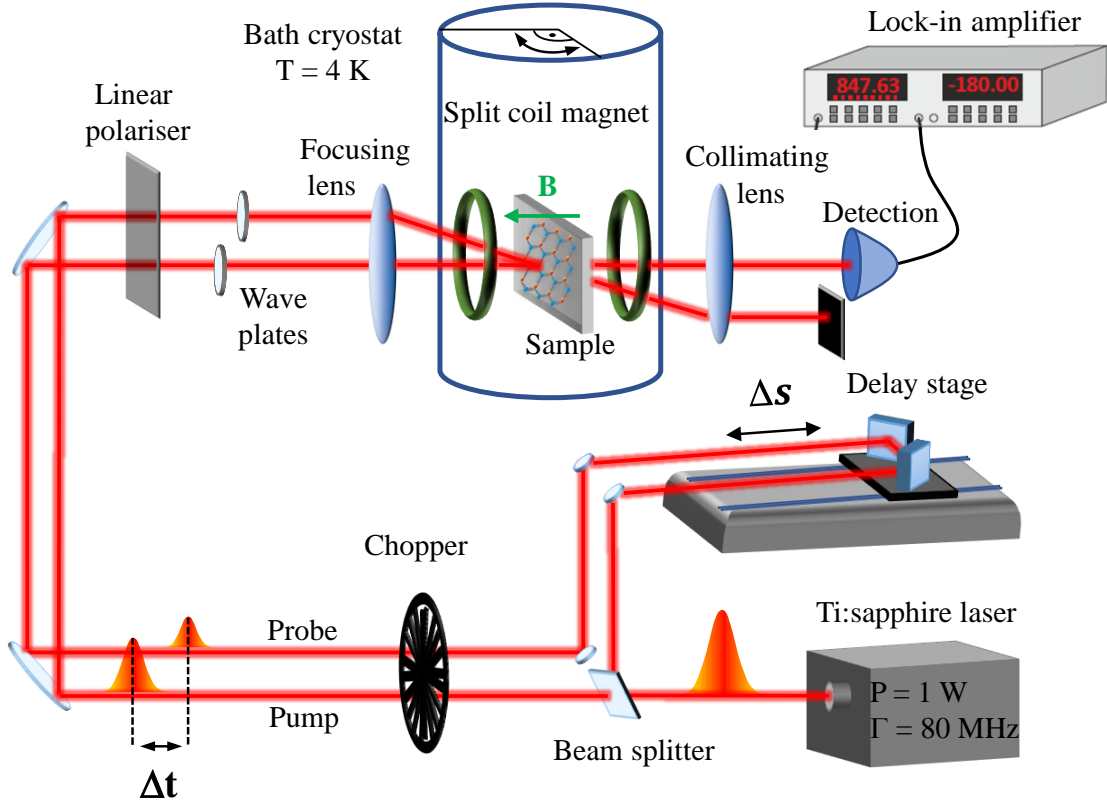
**Figure 3.8: Setup for pump-probe experiments.** A Ti:sa laser creates linearly polarised ultra-short laser pulses with a duration of approx. 100 fs. The cw output power ot the Ti:Sa amounts up to 1 W with a pulse repetition rate of $\Gamma_{Rep}$ = 80 MHz. The pulse is split into a pump and a probe beam. The latter one is time-delayed by an optical delay stage moving with sub-micron accuracy. The thereby additionally introduced optical pathway is proportional to the time delay between pump and probe pulse by $\Delta t = 2\frac{\Delta s}{c}$. Optical chopping of the beams is applied for lock-in detection. A linear polariser ensures perfect linear polarisation while the subsequent wave plates set the desired individual polarisation of pump and probe beam. Both pulses are focused into the cryostat. The superconducting split coil magnets provide magnetic fields up to 10 T at temperatures down to 1.4 K. The entire cryostat can be turned by 90°, enabling the exertion of in- and out-of plane magnetic fields. After transmission, the beams are collimated and the pump-probe signal is analysed. The specific detection schemes for Faraday and four-wave mixing experiments is specified in the corresponding sections.

using the knife-edge method following the instructions of Araujo et al. [Ara09]. A factor of 2 arises from the optical chopper because half of the power is blocked by the chopper wheel and accordingly, only half of the laser pulses account. The resulting maximal densities, applying full power, amount up to $1 - 2 \cdot 10^{12} \mathrm{cm}^{-2}$ for the single layer samples. For resonant excitation on the A exciton, the total absorption for the monolayers amounts to approximately 1%. For multilayers, there is certainly a distribution of the initial exciton density across the sample

that decreases exponentially with the thickness. So far it is not clear, up to which extent the excitons can spread and distribute in a multilayered crystal.

## 3.2.2 Time-resolved Faraday ellipticity

The Faraday effect can be seen as the corner stone of magneto-optical spectroscopy. In 1846, Michael Faraday discovered the rotation of the linear polarisation of light passing a medium in a magnetic field [Far46]. The microscopic understanding of this effect remained elusive for long time. Exploiting quantum mechanics, it can be traced back to a magnetically-induced difference of refractive indices for circularly polarised light. This causes a phase shift of both circular components, manifesting in a tilt of the linear polarisation. With the availability of tunable and ultrafast pulsed lasers, time-resolved magneto-optical spectroscopy was literally a question of time. This facilitated studies of spin dynamics and coherent spin manipulation in semiconductors GaAs quantum wells [Bau94; Cro97; Kik98]. In the last decade, this methods have been also adapted for the investigation of TMDCs [Zhu14; Hsu15; Dal15; Ple16].
According to the principles of light-matter interaction, the polarisation of light that passes a medium changes due to the material's complex refractive index $n^* = n + i\kappa$. In general, both components depend on the helicity of light which means that $n^*(\sigma^+) \neq n^*(\sigma^-)$. Since $n$ determines the speed of light in a material, the velocity for $\sigma^+$ and $\sigma^-$ polarised light can be different. Complementary, the imaginary part $\kappa$ of $n^*$ is related to the absorption of light. Consequently, the amount of absorption for $\sigma^{\pm}$ polarised light in general may differ from each other. For a linearly polarised beam, whose polarisation components consist of equal intensities of $\sigma^+$ and $\sigma^-$ polarised light, this implicates a retardation of the respective helicity components as well as an unequal diminution of its intensities after having passed a specific material. After interaction, the polarisation can be tilted and elliptical. The first effect is caused because of $n(\sigma^+) \neq n(\sigma^-)$ while latter one is owed to $\kappa(\sigma^+) \neq \kappa(\sigma^-)$. The analysis of the complex refractive index is equivalent to the material's complex dielectric function since $\varepsilon_r^* = (n^*)^2$ holds. As discussed in section 3.1.4 considering reflectance, the dielectric function of a material is related to the optical transitions that occur in the regarded material. The chiral selection rules that apply for TMDCs state that the helicity of light, the carrier's spin and the according valleys are coupled (spin-valley locking). By populating one of the valleys, the number of available states in the respective valley is reduced due to Pauli blocking. Hence, the condition $\kappa(\sigma^+) \neq \kappa(\sigma^-)$ is fulfilled. Therefore, time-resolved Faraday measurements represent a very power-
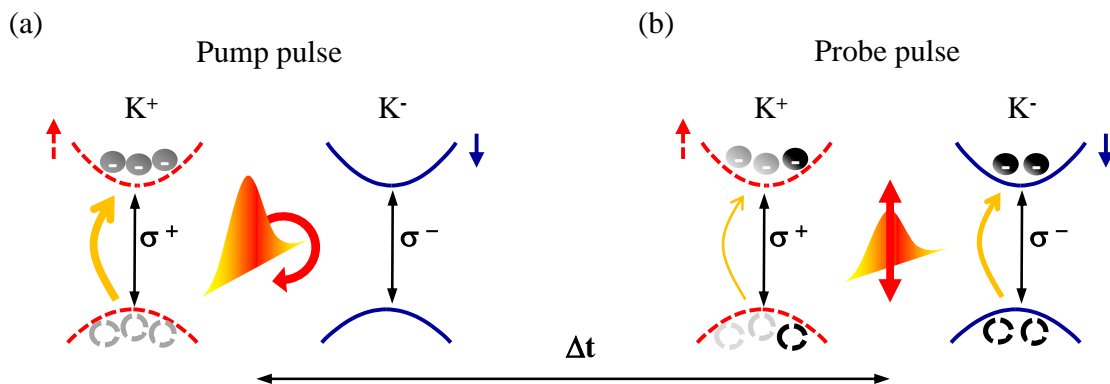
**Figure 3.9: Time-resolved Faraday ellipticity explained in the electronic band structure.** (a) The circularly polarised pump pulse creates a population in the according valley which diminishes over time. (b) After a tunable time delay $\Delta$ t, the linearly polarised probe pulse interacts with the sample. The residual carrier population causes dissimilar absorptions in both valleys. Finally, the ellipticity, i.e. the ratio of the $\sigma^+$ and $\sigma^-$ components is proportional to the absolute difference of the occupation of both valleys.

ful technique to probe spin- and valley dynamics. In principle, both, the rotation as well as the ellipticity of the polarisation can be analysed. As both quantities are connected via the Kramers-Kronig relations [Hie97; Zha09; Wal12], it is sufficient to acquire one of them. In a microscopic picture, it is more convenient to interpret the absorption dynamics that obey the optical selection rules. Therefore, the here presented Faraday experiments are throughout Faraday ellipticity measurements. An equivalent to Faraday experiments represent time-resolved Kerr rotation (TRKR) or ellipticity (TRKE) measurements with the distinction that the rotation or ellipticity of the reflected probe beam is evaluated. TRKR comes with the advantage that no transmissive setup is required which makes it much easier to handle within a microscope setup.

Experimentally, the afore described pump-probe setup is used with modifications in the polarisation optics in excitation and in the detection scheme. The pump pulse therefore is circularly polarised while the probe pulse remains linearly polarised. By the incident pump pulse, a population in a specific valley according to its helicity is created. The probe pulse experiences the pump-induced changes in $n^*$ which are imprinted in the rotation and ellipticity of the probe beam after having passed the sample. A visualisation of Faraday ellipticity in a microscopic picture is presented in figure 3.9. For detection, a balanced photo detection scheme is used which is presented in figure 3.10(a). The decisive element, deciding whether Faraday rotation or ellipticity is detected, figures the analysing wave plate. By using a quarter wave plate, the circular components are transformed to a linear
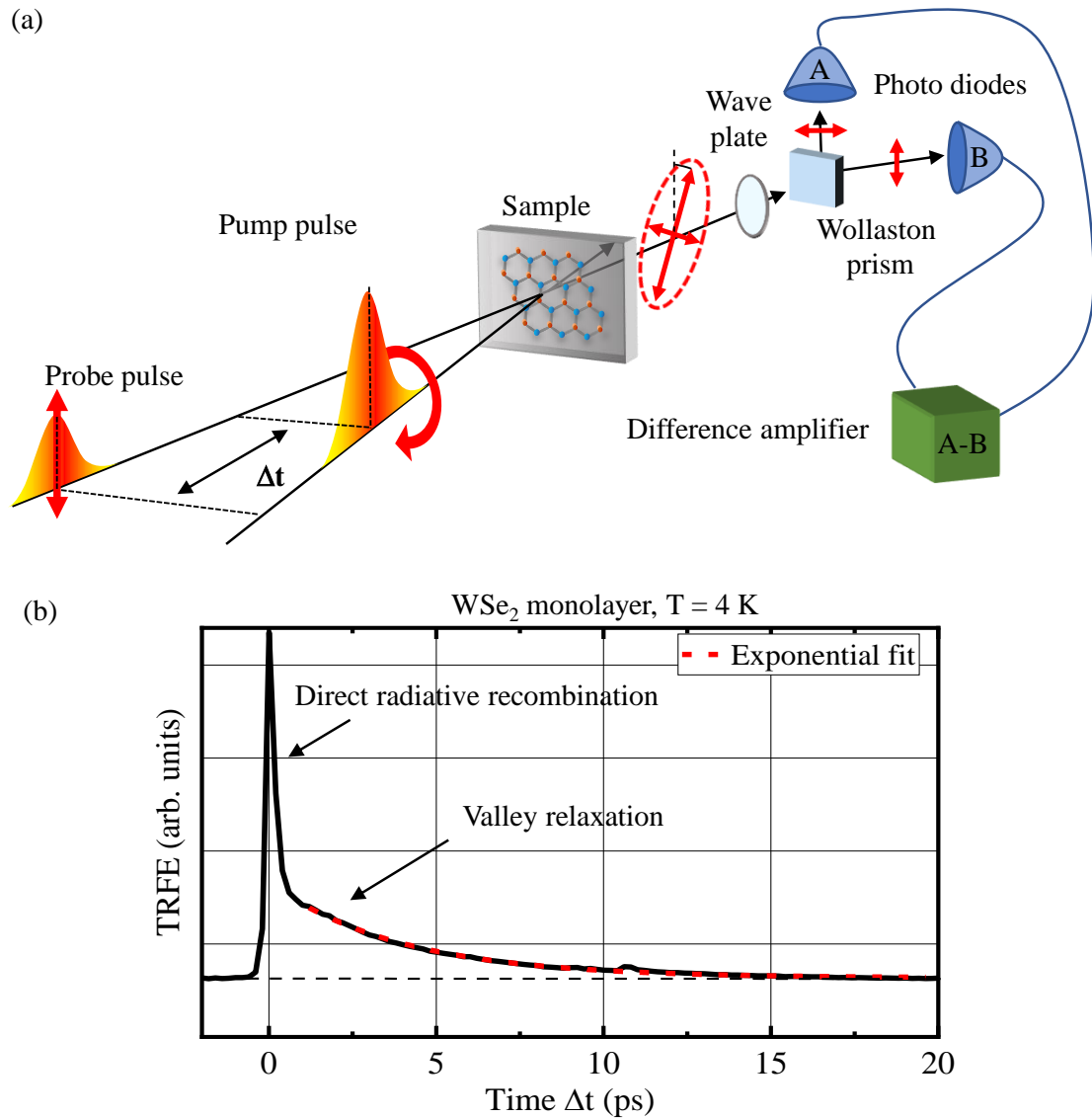
(a)



(b)



**Figure 3.10: Principle of time-resolved Faraday measurements.** (a) Schematic Faraday setup. The circularly polarised pump beam and the linearly polarised probe beam arrive with a certain but sequentially tunable time delay $\Delta t$ with respect to each other at the sample. The difference in the complex refractive index $n^*(\sigma^+) \neq n^*(\sigma^-)$ of the studied material causes a rotation and an ellipticity of the probe beam. By inserting a quarter wave plate (half wave plate), Faraday ellipticity (rotation) can be acquired. A balanced photo detection scheme records the changes of the ellipticity (rotation). The output signal is directly proportional to the change in ellipticity (rotation). (b) Exemplary TRFE measurement on WSe₂ monolayer. A large part of the initially excited excitons recombines radiatively within the first hundreds of femtoseconds. After thermalisation processes, this is followed by a much slower decay that maps the valley relaxation. It has to be emphasised that the TRFE signal monitors difference of the absolute population of the valleys.

polarisation and rotated such that the subsequent Wollaston prism splits up the linear components into equal intensities of horizontally and vertically polarised light. By introducing a half wave plate instead, the linear polarisation component along the major axis of the ellipsis is rotated such that it is divided by the Wollaston prism into two beams with equal intensities. In each case, both components are then recorded by two photo diodes. The photo-induced voltages are subtracted and amplified by a difference amplifier. For calibration, the wave plate is aligned while the pump beam is blocked such that signal of the difference amplifier is zero. A very tiny rotation or change in ellipticity creates a non-zero signal which is then passed to the lock-in amplifier. Balanced photo detection renders a very sensitive detection technique since it removes all shot noise of the laser and other fluctuating contributions from the surrounding. Combined with lock-in detection, benefiting from double chopping, an excellent level of accuracy as signal-to-noise ratio can be accomplished.

For a basic understanding of this technique, an exemplary TRFE data set of monolayer $WSe_2$, which is shown in figure 3.10(b), is discussed next. At $\Delta t = 0$, the pump and probe pulses overlap in time. At this point, the difference of the populated valleys is largest and thus the signal maximal. Owed to direct radiative recombination, the signal diminishes significantly within the first few hundred femtoseconds. The residual exciton population interacts with its surrounding and thermalises. In this regime, valley relaxation, mostly driven by long-range exchange interaction, takes place. For the latter time interval, the data can be modelled by a mono-exponential fit from which the decay constant $\tau_{TRFE}$ is obtained. In general, the TRFE signal is zero when the excitons are equally distributed in both K valleys, or, if all excitons have vanished. To disentangle both contributions, the knowledge about the exciton lifetime is required, which can be retrieved from transient differential transmission measurements. In order to obtain the pure valley dephasing, the influence of the limited carrier lifetime $\tau_{life}$ has to be considered by applying Matthiessen's Rule:

$$\frac{1}{\tau_{TRFE}} = \frac{1}{\tau_{valley}} + \frac{1}{\tau_{life}} \tag{3.7}$$

The thereby obtained value $\tau_{valley}$ so-to-say describes the pure dephasing of the valley pseudospin which can be interpreted analogously to the pure dephasing of an ensemble of two-level systems as discussed in chapter 2.2.2.

### 3.2.3 Time-integrated four-wave mixing

Non-linear optics is a fascinating phenomenon that occurs when the electric field strength of the incident light is comparable to the atomic fields of the interacting material. As a consequence, higher-order contributions of the material's polarisation cause an optical response that contains multiple frequencies. This allows for frequency conversion of the applied light like second-harmonic generation or frequency mixing and in particular, for four-wave mixing (FWM). Regarding semiconductor physics, time-resolved FWM represents an indispensable technique to unravel the elemental temporal evolution of charge carriers. In contrast to other time-resolved spectroscopy methods, it provides direct access to the fundamental time constants $T_1$ and $T_2$ and thus constitutes an essential link between theoretical considerations and experimental findings. In the following section, the concrete experimental approaches to acquire the desired time constants is presented, focussing on degenerate time-integrated FWM which is the most basic FWM approach that is also used in this work.

In general, the optical response of a material is radiated by the polarisation that is created by an external driving field. For higher intensities, the polarisation scales not linear with the driving field any more and the resulting optical response contains higher-order contributions. The issue of non-linear optics and its microscopic origin is visualised in figure 3.11. Explicitly, the non-linear polarisation $P$ can be expanded up to the order of $i$ by a power series of the susceptibility tensors $\chi^{(i)}$ and the driving electric fields $E$:

$$P = \sum_i \varepsilon_0 \chi^{(i)} E^i \tag{3.8}$$

If waves with different amplitudes and frequencies generate the non-linear signal, the explicit expression for the polarisation becomes more complex because of the tensor character of $\chi$ with rank $(i+1)$. The third-order polarisation, which is the source of the FWM signal, writes as:

$$P_i^{(3)} = \sum_{j,k,l} \varepsilon_0 \chi_{i,j,k,l}^{(3)} E_j E_k E_l \qquad \text{with} \ \ \{i,j,k,l\} \ \epsilon \ \{x,y,z\} \tag{3.9}$$

Accordingly, the above denoted tensor comprises 81 elements. The entries of the tensor are material-specific and quantify the contributions for three individual waves that are incident on a material with a specified orientation. By the symmetry of the regarded material, the number of relevant tensor elements can be reduced down to a minimum of 3 for an isotropic material. Considering light
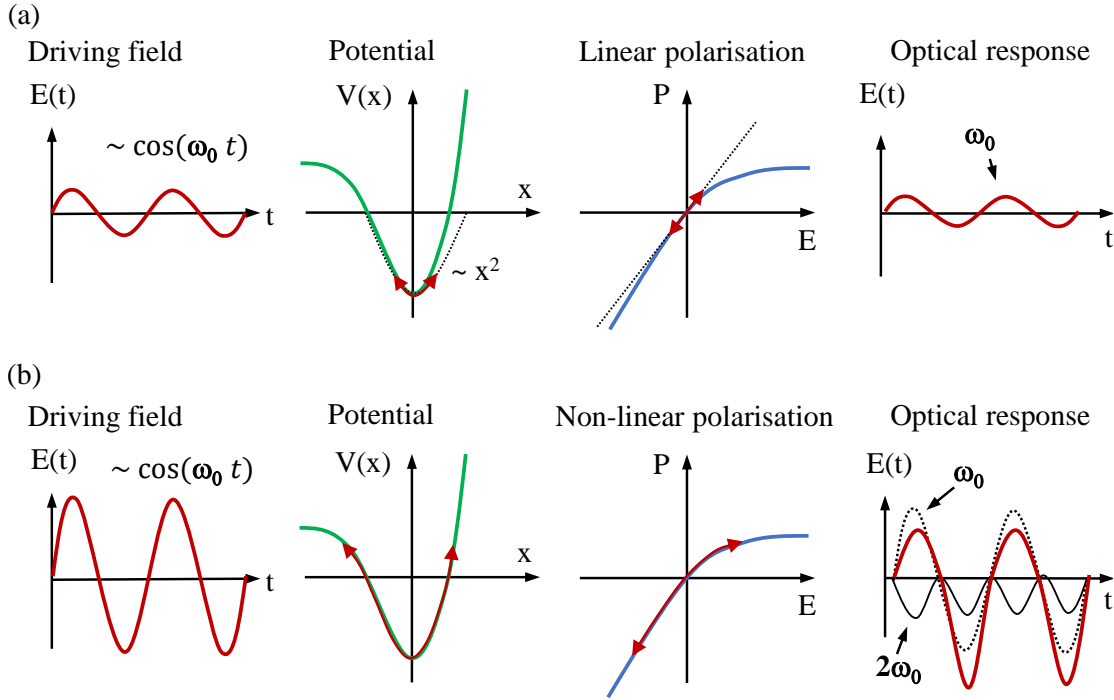
(a)



(b)



**Figure 3.11: Origin of a non-linear optical response.** (a) Linear optics. For weak electro-magnetic excitation, the polarisation of a material follows the periodic driving field with frequency $\omega_0$ linearly since the electronic potential is mostly harmonic in this regime. The resulting optical response has the same frequency. (b) Non-linear optics. If the driving fields are as strong as the atomic fields of the constituent atoms, the core potentials and the therefrom resulting polarisation contains higher harmonics which contribute in the optical response. As a consequence, multiples of the input frequency appear as for example $2\omega_0$. Figure inspired by [Fox12].

as a particle, energy- and momentum conservation for FWM formulates rather intuitive. Energy conservation is given by $\omega_{FWM} = \sum_i^3 \pm\omega_i$. Analogously, momentum conservation, coined as 'phase matching', writes as $\vec{k}_{FWM} = \sum_i^3 \pm\vec{k}_i$. The input frequencies that are mixed determine, according to energy conservation and phase matching, frequency and direction of the fourth wave. Energy conservation is commonly displayed with the help of a level diagram as shown in figure 3.12(b). This representation proposes virtual levels. Although FWM is not explicitly frequency-dependent, it can be strongly enhanced when a virtual level meets a real electronic transition. Momentum conservation is typically represented using vector addition of the participating wave vectors as sketched in figure 3.12(a). If the radiated signal is acquired with a detector that is much slower than the FWM signal (most simply by a photo diode), the resulting signal seizes the time-integrated intensity of the FWM signal (TI-FWM) although a pump-probe scheme is employed. Correctly speaking, 'Time-resolved FWM' implicates that
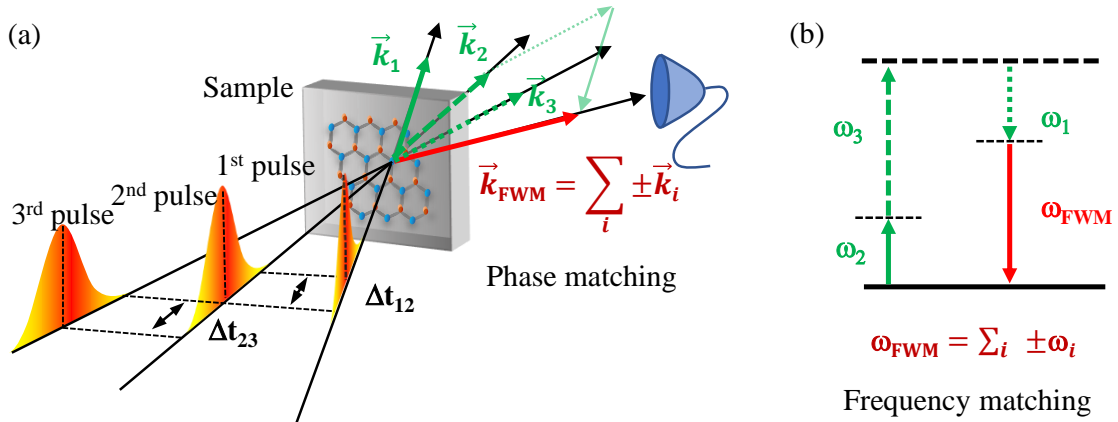
**Figure 3.12: Principle of time-resolved four-wave mixing.** (a) Schematic setup for three-beam FWM. Three different laser pulses illuminate the sample with controllable time delays between each other. A third-order polarisation is created thereby which causes the FWM signal. The radiation direction of the FWM signal is determined by the chosen phase matching condition $\vec{k}_{FWM} = \vec{k}_2 + \vec{k}_3 - \vec{k}_1$. (b) Energy conservation at FWM. A level scheme is commonly used to visualise the output energy $\omega_{FWM} = \omega_2 + \omega_3 - \omega_1$. The energy levels are indicated with dotted lines. In principle, these can be real electronic transitions (resonant four-wave mixing) but also virtual levels.

the signal itself is recorded with a temporal resolution. This can be realised by interferometric means. A detailed description of this technique can be found in [Lan06]. In the here presented work, exclusively TI-FWM experiments have been performed. A further facilitation of FWM represents 'degenerate' FWM where all three laser pulses stem from the same laser and consequently exhibit exactly the same energy and pulse duration.

The specific arrangement of the pulse sequences determines whether the population decay time $T_1$ or the dephasing time of the coherent superposition state, which can be interpreted as the system's coherence, $T_2$ is investigated. In analogy to nuclear magnetic resonance experiments, $T_1$ and $T_2$ are also referred as longitudinal and transversal relaxation times, respectively. For the investigation of the $T_1$ constant, the time delay $t_{12}$ between the first two pulses has to be kept fixed and is commonly set to zero, while for the determination of the $T_2$ time, the time delay $t_{23}$ between the second and the third pulse has to be maintained constant. The theoretical description of FWM is based on the semiconductor Bloch equations (cf. chapter 2.2.2), expanding the coupled equations of motion for the population and the polarisation up to the third order. An analytical solution only exists under the presumption of delta pulses [Sha13]. A more intuitive understanding of resonant FWM bases on the idea that the first pulse with wave vector $\vec{k}_1$ creates a coherent first-order polarisation. The second pulse with wave vector $\vec{k}_2$ interferes
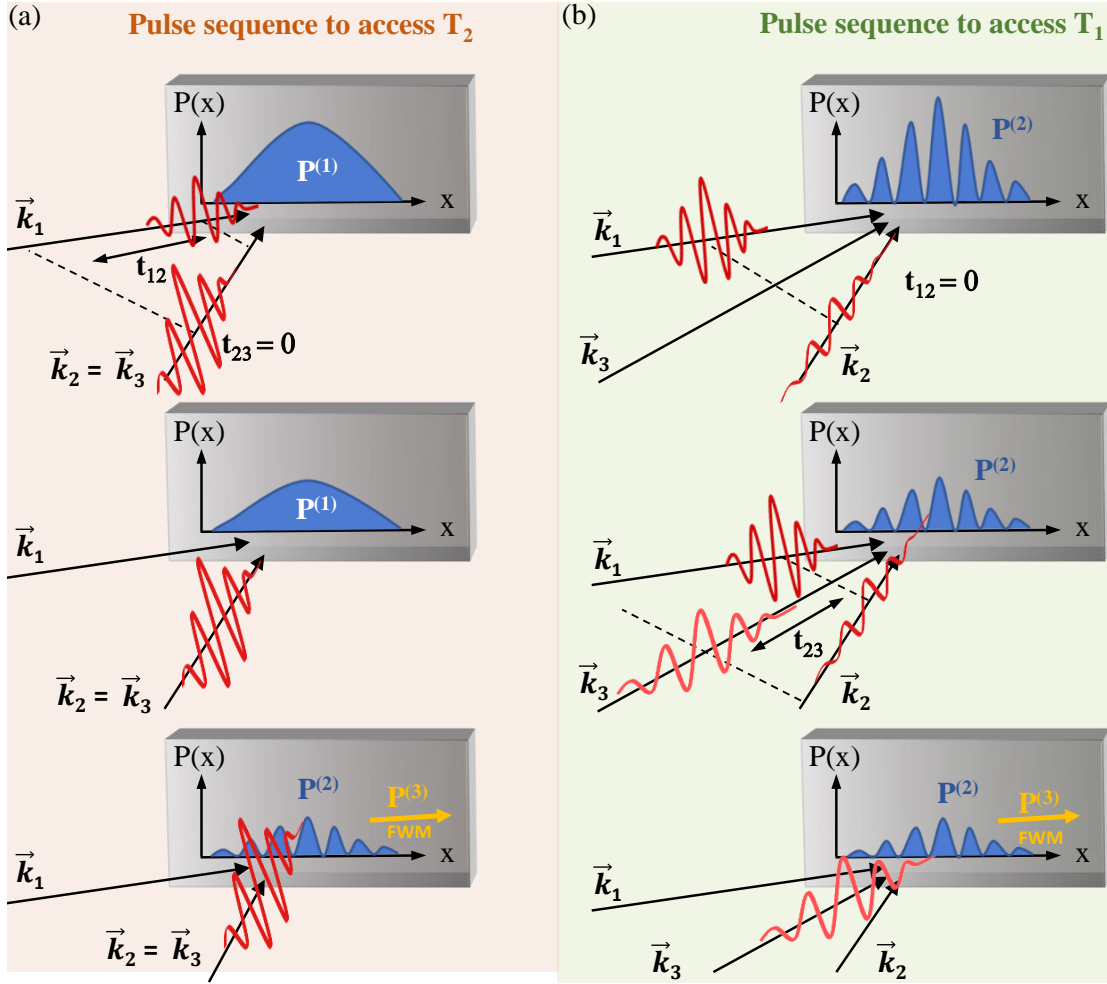
**Figure 3.13: Figurative explanation of FWM for the acquisition of the $T_2$ and the $T_1$ time.** (a) Investigation of the $T_2$ time. A first laser pulse generates a coherent polarisation P(x). The second pulses, which can be interpreted as a superposition of two identical pulses with $t_{23} = 0$, arrives at the sample after a time delay $t_{12}$. From the interference with the residual coherent polarisation, a second-order polarisation forms that can be regarded a density grating. Simultaneously, the pulse is self-diffracted on the density grating, radiating the FWM signal into the direction of $\vec{k}_{FWM}$. The quality of the formed density grating directly relies on the coherence of the ensemble, which diminishes over time, before the second pulse is incident. Consequently, the FWM signal has the $T_2$ time imprinted. (b) Determination of the $T_1$ time. Here, the time delay between the first and the second pulse is set to zero , i.e. $t_{12} = 0$. Thus, the interference of the pulses results in a flawless formation of a density grating. Subsequently, exclusively the relaxation of the ensemble causes the degradation of the grating. Accordingly, the diffraction of the third pulse is a measure of the ensemble's lifetime $T_1$.

with the residual polarisation, giving rise to a second-order polarisation that can be regarded as a density grating n($\vec{k}_1, \vec{k}_2$). The third pulse with wave vector $\vec{k}_3$ is subsequently diffracted on the grating, giving rise to a third-order polarisation

that radiates the FWM signal [Sha13]. Figure 3.13(a) visualises the specific steps for the investigation of the $T_2$ time. When the second pulse arrives, the formation of a density grating is dependent on the remaining coherence of the ensemble. The third pulse is diffracted on the density grating into the direction of $\vec{k}_{FWM}$. For this specific pulse arrangement, the intensity of the FWM signal is thus a direct measure of the ensemble's coherence and diminishes with the $T_2$ time imprinted. Conveniently, this experiment is performed in a two-beam setup, since the second pules can act virtually as two pulses. Figure 3.13(b) depicts the steps for the detection of the $T_1$ time. Therefore, the time delay between the first and the second pulse is commonly set to zero. Accordingly, coherence is inherently perfect and the resulting density grating is immaculate. Over time, the quality of the grating declines which solely is caused by the relaxation of the ensemble. The diffraction of the third pulse causes the radiation of the FWM signal which carries the information about the ensemble's lifetime $T_1$. In order to facilitate interference of pules one and two, the directions of $\vec{k}_1$ and $\vec{k}_2$ have to be different. Consequently, a three-beam set up is inevitable. Even though this picture is rather simplified, it helps to understand why setting $t_{23} = 0$ ($t_{12} = 0$) yields an FWM signal that carries the $T_2$ ($T_1$) time constant. Furthermore, it becomes apparent that for the determination of $T_1$, a three-beam setup is required since for the emergence of a interference pattern that causes the density grating, $\vec{k}_1$ and $\vec{k}_2$ have to be different. The experiments presented in this work stem from a two-beam setup. Consequently, only the coherence time $T_2$ is investigated.

The analysis of the acquired FWM data needs to be more sophisticated than for the afore discussed TRFE experiments. Since the excitation pulse as the probe pulse are not sharp in time compared to the regarded dynamics, the resulting signal $F(t)$ is given by a convolution of the instrumental function $f_{instr}(t)$ of the setup with the overlying decay function $f_{dec}(t)$.

$$F(t) = f_{instr}(t) * f_{dec}(t) \tag{3.10}$$

Assuming perfect mode-locking and omitting the chirp of the laser pulse, its temporal shape is described by a Gaussian. The according instrumental function is given by the autocorrelated function of the laser pulse:

$$f_{instr}(t) = \frac{1}{\sqrt{2\pi}\sigma} \exp\left(\frac{-(t - t_0)^2}{2\sigma^2}\right) \tag{3.11}$$

with $\sigma$ denoting the standard deviation. Neglecting density effects, a mono-exponential decay function models the decay:

$$f_{dec}(t) = A \exp\left(\frac{-t}{\tau}\right) \tag{3.12}$$

The convolution of both yields the following fitting function:

$$F(t) = y_0 + A \exp\left(\frac{1}{2}\frac{\sigma^2}{\tau^2} - \frac{t - t_0}{\tau}\right) \cdot \mathrm{erf}\left(\frac{t - t_0}{\sigma} - \frac{\sigma}{\tau}\right) \tag{3.13}$$

Here, erf() denotes the error function. The data analysis software OriginLab® provides a pre-implemented fitting function, which has been applied to all FWM data sets where decay times have been determined. An exemplary analysis of an FWM data set, evaluated with a convolution fit, is presented in figure 3.14. The
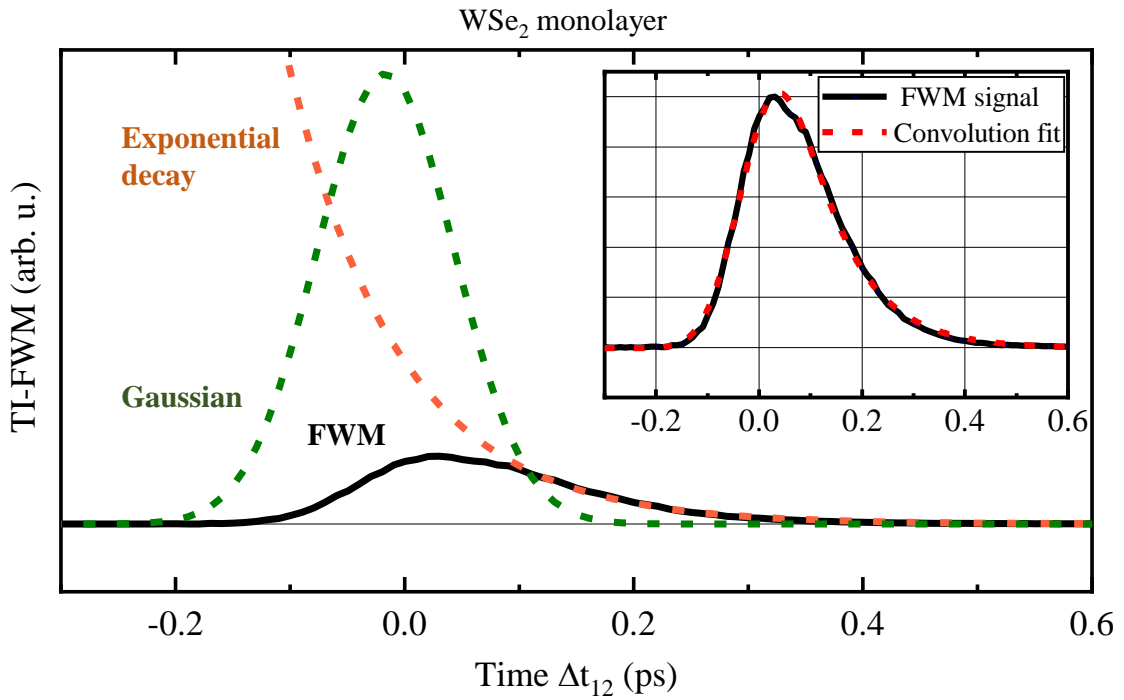


**Figure 3.14: Exemplary evaluation of TI-FWM data from monolayer WSe₂.** As the FWM signal is very short-lived, ranging in the same duration as the exciting laser pulse, the Gaussian shape of the laser pulses must be incorporated for an appropriate evaluation. The fitting function is given by a convolution of the instrumental function (autocorrelation of the applied laser pulses) and a decay function (basically an exponential). The inset shows a close-up of the FWM signal (solid black line) fitted with a convolution fit (red dotted line). Therefrom, the decay constant $\tau$ of the exponential decay can be determined. The orange and green dotted lines denote the individually plotted exponential and Gaussian functions whose convolution results in the red dotted line.

concrete shape of the decaying FWM signal depends on the type of broadening acting on the ensemble of two-level systems. Therefore, the temporal evolution of the FWM signal from which in a TI-FWM setup, only the integrated signal can be acquired, has to be reviewed in particular. For this consideration, $t_{12} := \Delta t$ and $t_{23} = 0$ is assumed. In a homogeneously broadened system, all oscillators of the system possess the same frequency which is only unsharp due to the uncertainty principle. Immediately after the arrival of the second pulse, the emission of the third-order polarisation sets in which is termed as a 'Free polarisation decay'. Integrating the FWM signal over time renders the TI-FWM signal that decays with $\sim \exp(-2\Delta t/T_2)$. Schematically, this is visualised in figure 3.15(a). Accordingly, $T_2$ is obtained by doubling the exponential decay constant of the upper presented convolution fit. Considering inhomogeneous broadening, which is the common case in our experiments, things get more complex. Due to different local environments, the individual two-level systems exhibit slightly different eigenfrequencies that are distributed normally. Thus, the single oscillators lose their phase relation comparatively fast and hence add up to zero on average. Therefore, the coherent macroscopic polarisation diminishes much faster. Nonetheless, the particular systems still oscillate with their respective eigenfrequencies. By reversing the individual phases by a factor of $\pi$, it is possible to recover the initial phase relation. In an FWM experiment, this phase shift is triggered by the simultaneous excitation of pulse 2 and 3. In principle, this process is equivalent to a coherent manipulation on the Bloch sphere that consists of a sequence of pulses with pulse area of $\pi/2$ (first pulse) and $2 \cdot \pi/2 = \pi$ (pulse 2 and 3). Here, the second pulse causes a rotation of $\pi$ on the Bloch sphere which leads to the rephasing of the individual polarisation components. As the FWM photon echo scales with $\sim \exp{-(\frac{t-2\Delta t}{T_2})}$, its integration yields an intensity $\sim \exp(-4\Delta t/T_2)$. Thus, for inhomogeneously broadened systems, $T_2$ is four times longer than the decay constant from the fit. The formation of a photon echo and it's integration is sketched in figure 3.15(b).
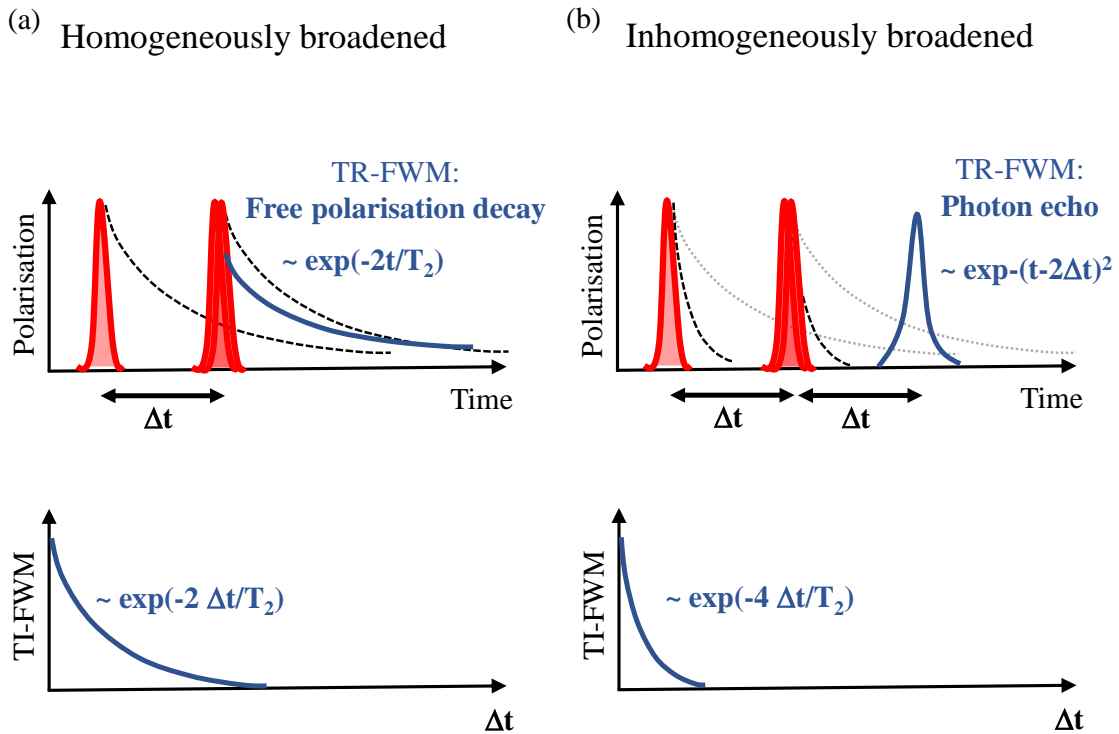
**Figure 3.15: Influence of inhomogeneous broadening on TI-FWM.** (a) FWM in homogeneously broadened systems. All oscillators have the same frequency. The black dotted lines give the evolution of the coherent polarisation which is generated by each pulse. Directly after the arrival of the second pulse, the emission of the third-order polarisation sets in which is termed as a 'Free polarisation decay'. Integrating the FWM signal over time renders the TI-FWM signal that decays with $\sim \exp(-2\Delta t/T_2)$ which is shown in the plot below. (b) FWM in inhomogeneously broadened systems. Here, the individual two-level systems exhibit slightly different eigenfrequencies. The resulting coherent macroscopic polarisation averages soon to zero (black dotted lines). Still, the individual polarisations persist (fading dotted lines). The arrival of the second pulse causes a conjugation of the individual phases such that the FWM signal manifests after an additional delay of $\Delta t$ in terms of a photon echo. Integration yields the TI-FWM intensity, decaying twice as fast as for homogeneously broadened systems. Graphs inspired by [Kli12].

# Chapter 4

# Results and discussion

The discovery of the direct bandgap in TMDC monolayers [Mak10; Spl10] attracted so much attention, that the profound physics of thin multilayer crystals remained among the shades for many years. Within the past years, the intense prospecting of moiré excitons in twisted heterostructures has evoked controversial results [Sey19; Tra19; Jin19; Ale19]. The striking discovery of superconductivity in 'Magic-angle graphene' [Cao18] has outlined the importance of the stacking arrangement as well as the number of layers even for pure materials. Recently, the focus has turned towards the investigation of multilayer crystals, disentangling inter- and intralayer excitons and hybridisation effects of different excitonic species [Aro18; Mun19; Zha23; Erk23; Tag23; Yu23]. Technically, the observation and interpretation of exciton dynamics turn out to be rather complex in multilayered structures due to the indirect band gap, spanning from $\Gamma$ in the valence band to $\Sigma$ in the conduction band.

In this thesis, it is aimed to give a comprehensive picture of the exciton dynamics in mono- and multilayer $MoSe_2$ and $WSe_2$ on the basis of transient differential absorption, time-resolved Faraday ellipticity and four-wave mixing experiments. The combination of these techniques combined with the use of external magnetic fields, renders an excellent tool box for this purpose. Comparing the results of mono- and multilayer samples allows to distinguish very clearly between layer-intrinsic properties and multilayer contributions.

## 4.1 Transient differential transmission

To start, transient differential transmission measurements are envisaged in order to determine the carrier lifetime of the $A_{1s}$ excitons. Figure 4.1 displays pump-probe measurements on monolayers of $MoSe_2$, $WSe_2$, CVD-grown $WSe_2$

(a)

Monolayer MoSe$_2$ in hBN, T = 4 K

(b)

Monolayer WSe$_2$ in hBN, T = 4 K

(c)

Monolayer CVD-WSe$_2$ in hBN, T = 4 K
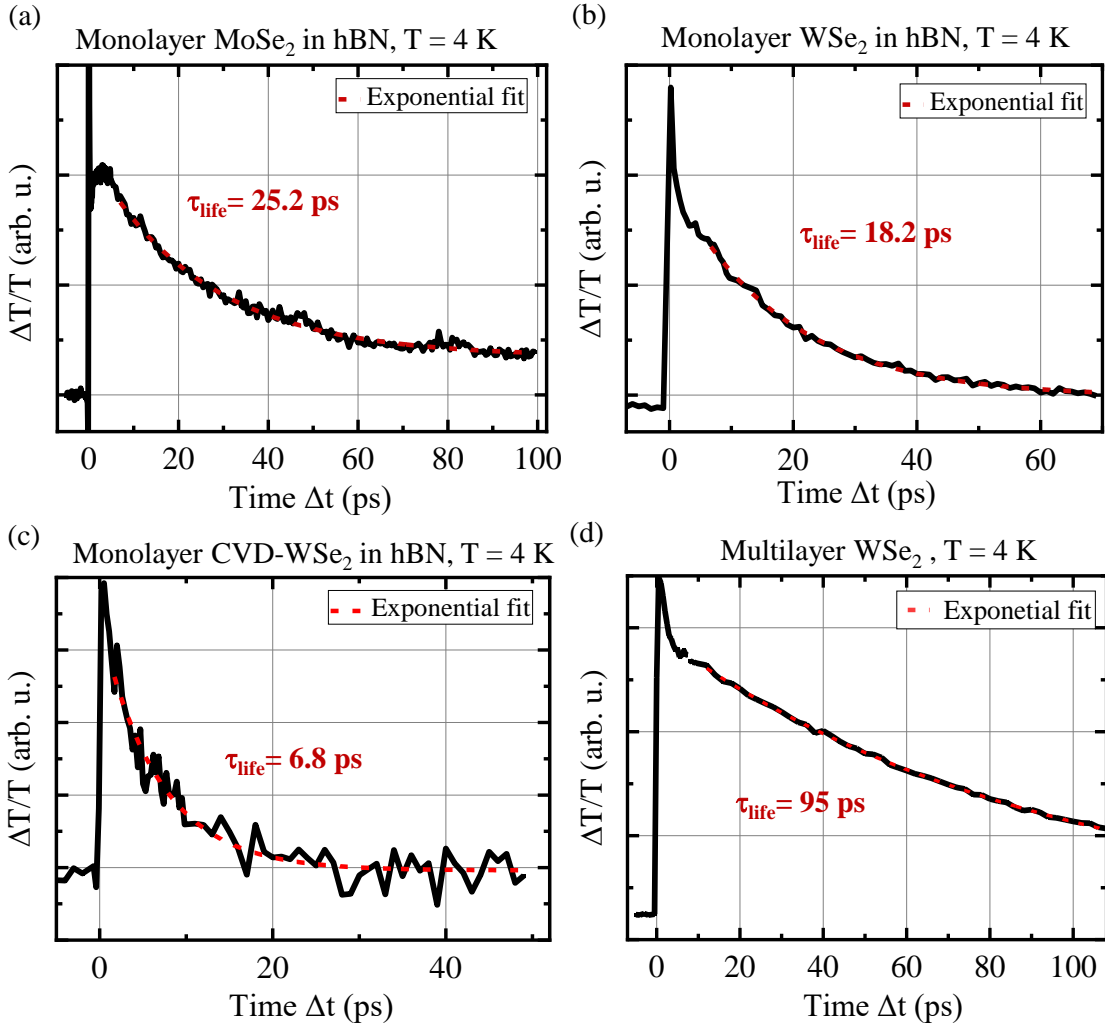
(d)

Multilayer WSe$_2$ , T = 4 K

**Figure 4.1: Exciton lifetimes from transient differential transmission measurements.** Neglecting the very fast direct radiative decay around $\Delta t = 0$, a mono-exponential fit (red dotted line) models the data accurately. The corresponding decay constants are given in the graphs. (a) Exfoliated single-layer MoSe$_2$. (b) Exfoliated WSe$_2$ monolayer. (c) CVD-grown WSe$_2$ monolayer removed from the growth substrate and encapsulated in hBN. The signal decays three times faster than in the exfoliated monolayer sample. (d) The pump-probe response of multilayer WSe$_2$ exhibits a five times longer decay time than its monolayer which can be assigned to the lowering of the $\Sigma$ valley.

and multilayer WSe$_2$. Common for all samples is the occurrence of a very fast decay in the femtosecond range followed by a slower decay evolving on a picosecond time scale. The sharp peaks around $\Delta t = 0$ reflects intrinsic direct radiative recombination of excitons, that are created inside the light cone, which directly decay radiatively before any interaction can take place. Typically, the direct radiative lifetime $\tau_{rad}$ in TMDCs ranges between 100 - 200 fs [Wan18; Moo16; Liu23]. The data quality of our transient differential transmission measurements does not

allow to precisely determine values for the direct radiative lifetime. However, it is also imprinted on the TRFE data, where this fast decay dynamics are mapped much clearer due to difference amplification. For monolayer $WSe_2$, a decay time of $\tau_{rad} = 0.15$ ps for the direct radiative lifetime of the $A_{1s}$ exciton is found which is in very good agreement with the report of Poellmann et al. [Poe15] and also with the calculated value of $\tau_{rad} = 0.16$ ps by Zhu et al. [Zhu14]. For monolayer $MoSe_2$, the fast and slow dynamics are not as well separated and make it hence not possible to extract reliable values for $\tau_{rad}$ neither from transient differential transmission nor from TRFE measurements.

In a transient differential transmission measurement, the slower decay that sets in after a few picoseconds monitors the dynamics of the carrier population that is in thermodynamical equilibrium. The according lifetime can be obtained from a a mono-exponential fit. For monolayer $MoSe_2$, a lifetime of $\tau_{life} = 25.2 \pm 0.5$ ps is found at an according exciton density of $n \sim 1.9 \cdot 10^{12}$ cm$^{-2}$ (cf. figure 4.1). These findings are in line with the transient reflectivity measurements of Anghel et al., reporting an exciton lifetime of 20 ps at an injected exciton density of $n \sim 2.4 \cdot 10^{11}$ cm$^{-2}$ at a temperature of 4 K [Ang18]. Merkl et al. report an exciton lifetime of 50 $\pm$15 ps for H-type $WSe_2$ bilayer, which has been obtained from pump-probe measurements at a temperature of 5 K, exploiting the internal 1s – 2p transition of excitons [Mer20]. Besides, Fang et al. evidence that the excitons' radiative lifetime can be tailored by the thickness of the encapsulating hBN making use of the Purcell effect [Fan19].

For monolayer $WSe_2$, our experiments reveal a lifetime of $\tau_{life} = 18$ $\pm$0.5 ps at an exciton density of n $\sim 1.3 \cdot 10^{12}$ cm$^{-2}$. This result is in very good accordance with results from literature. Cui et al. determine an exciton lifetime of 18 ps from pump-probe-based differential reflection, pumping resonantly at 750 nm and probing at 405 nm for different pump fluencies at ambient conditions [Cui14]. The insusceptibility to higher temperatures and pump fluencies can be related to the dark exciton state which is energetically located below the bright state, acting as a profound reservoir. Moody et al. measure the exciton population dynamics via TI-FWM. A fast decay of 210 fs, reflecting the intrinsic bright exciton population dynamics, is followed by a slower decay that is assigned to the thermalised exciton population with a corresponding decay constant of 17 ps [Moo15]. Inspecting the CVD-grown monolayer $WSe_2$ flake, a lifetime of $\tau_{life} = 6.8 \pm 0.5$ ps at an exciton density of about n $= 1 \cdot 10^{12}$ cm$^{-2}$ is found. The significant difference with respect to the exfoliated samples can be related to the poorer sample quality owed to the CVD growth process. The defect states and impurities that are incorporated in CVD-grown monolayers provide additional relaxation channels, causing a quicker

decay of the carrier population [Cai18]. This effect also appears in PL and in the RC data, exhibiting a comparably broad linewidth and weak optical activity.

Moving on towards multilayer WSe$_2$, a lifetime of $\tau_{life} = 95 \pm 1$ ps is found. The five times longer decay time with respect to the monolayer of the same material can be ascribed to the lowering of the $\Sigma$ valley in the CB which is favourable for the electrons to relax into. Accordingly, the resulting excitons are momentum-dark and thus comparably long-lived while the excitons' holes still prevail in the K valley, bleaching the bright A$_{1s}$ transition. Unfortunately, the transient differential transmission has not been measured for multilayer MoSe$_2$. This issue can be overcome with values from literature. Kumar et al. report values of several hundreds of picoseconds from their transient differential transmission (T = 300 K) [Kum14]. Their values are rather independent of the excitation density. In general, the prolongation of the exciton lifetime in TMDC multilayers the can be related to the lowering of the $\Sigma$ valley, facilitating the formation of momentum-indirect excitons. 'Time-resolved Photo Emission Spectroscopy' (TR-ARPES) is able to track the transfer of the excitons' electrons in momentum space from K to $\Sigma$, occurring within less than hundred femtoseconds in multilayer TMDCs [Bus19; Don21]. The results from TR-ARPES manifest the complexity of the exciton dynamics in TMDCs. The excitons' electrons exhibit much faster dynamics than the one found in the beforehand transient differential transmission measurements. However, TR-ARPES only reveals so-to-say the tip of the iceberg. Due to its rudimental sensitivity and spectral resolution, ARPES can solely map the dynamics of the unthermalised exciton population directly after its generation which is also responsible for the sharp and prominent signals at $\Delta$t = 0 in the here presented transient differential transmission measurements. The rather general question poses whether the pump-probe responses for longer times principally reflect the dynamics of the bright K - K excitons, relaxing back towards the light cone or, mostly monitor the holes of the momentum indirect $\Sigma$ - K excitons which also are blocking the K - K transition. At this point, no conclusive statement can be given.

In summary, the here found lifetimes are in good accordance with reports from literature on population dynamics investigated by pump-probe techniques. Furthermore, the knowledge about the exciton lifetimes, pumping and probing the K - K transition, serves as a valuable information to disentangle valley- and population dynamics at the K valleys as it is discussed in the next section.
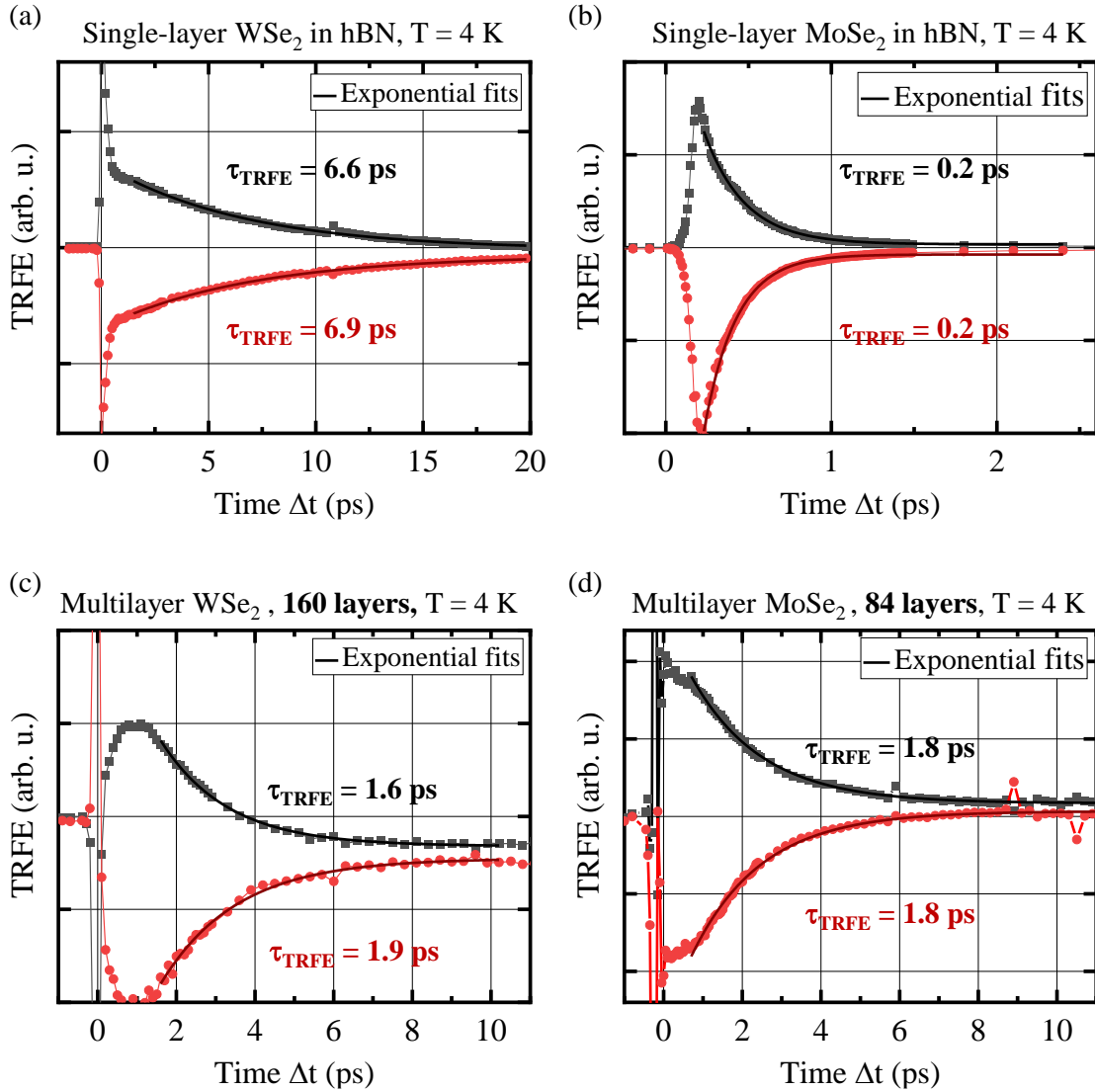
# 4.2 Time-resolved Faraday ellipticity experiments



**Figure 4.2: TRFE measurements on single- and multilayer MoSe$_2$ and WSe$_2$.** All samples have been excited at the according A$_{1s}$ exciton resonance, kept at a temperature of 4 K. (a) TRFE on single-layer WSe$_2$. The sharp peak directly after excitation reveals direct radiative recombination of the bright excitons. The subsequent valley relaxation is much slower. The small peak at 12 ps stems from a reflex of one of the pulses. (b) TRFE on monolayer MoSe$_2$. Valley relaxation appears to be much faster than on WSe$_2$ since there is no dark state that can act as a reservoir, feeding the bright state. Moreover, the very small energy splitting of the bright and dark excitons renders an additional scattering channel to the immanent long-range electron-hole interaction. (c) TRFE on multilayer WSe$_2$. Interestingly, it takes some picoseconds to form a valley polarisation. The following decay process occurs much faster than in the monolayer case. (d) TRFE on multilayer MoSe$_2$. Here, the valley relaxation process slows down compared to the single layer. Similar to bulk MoSe$_2$, a kind of build-up process is visible.

Time-resolved Faraday ellipticity can give access to the dynamics of a valley polarisation in TMDCs, or in other words, to the temporal evolution of the valley pseudospin.

The discussion is started by the presentation of TRFE measurements on single- and multilayer $WSe_2$ and $MoSe_2$ which are plotted in figure 4.2. The laser energy has been tuned to the specific $A_{1s}$ exciton resonances of the regarded sample. According to the circular polarisation of the pump pulse, the valley polarisation of the $K^+$ or of the $K^-$ valley is analysed. Without any applied external fields, both K valleys are degenerate. Consequently, the traces for $\sigma^+$ and $\sigma^-$ polarised excitation are expected to be identical except for the sign. The generated exciton densities are all below $2 \cdot 10^{12}$ cm$^{-2}$ (per layer in the multilayer samples) and thus well below the Mott density as discussed in chapter 3.2.1. Omitting the signal within the first few hundred picoseconds where direct radiative decay of excitons, as well as interference effects and non-linearities take place, the data is analysed by fitting mono-exponential decay functions for both polarisations.

For monolayer $WSe_2$, decay constants of $\tau_{TRFE} = 6.6 \pm 0.5$ ps and $\tau_{TRFE} = 6.9 \pm 0.5$ ps for $\sigma^+$ and $\sigma^-$ polarisation are found which is in very good agreement with the reported valley relaxation time of 6 ps, measured via TRKR on a bare $WSe_2$ monolayer on a $SiO_2$ substrate by Zhu et al. [Zhu14] (reprinted in figure 4.3(a)). Besides, the impact of temperature is nicely shown in this graph.

For monolayer $MoSe_2$, a valley relaxation time of $\tau_{TRFE} = 200$ fs is found for both polarisations (cf. figure 4.2(b)). This result is relatively short compared to other publications. Previous work in our own group revealed valley relaxation times of about 750 fs for bare monolayer $MoSe_2$ on sapphire investigated in the same setup as the below presented results [Hir20]. Schwemmer et. al have found a significant dependence of the intrinsic doping level of the valley relaxation times in monolayer $MoSe_2$, reporting decay times between 1 and 2 ps. Doping, i.e. resident carriers, causes a long-lived component in the TRFE signal but also affects the faster decay process that is attributed to the excitons' valley relaxation [Sch17]. Recently, Rojas-Lopez et al. published values of 2 ps for the valley relaxation time in monolayer $MoSe_2$, obtained from TRKR measurements [Roj23]. The reasons for these strong variation may arise from the particular thickness of the encapsulating hBN layers which can alter the radiative lifetime up to 10 ps [Fan19]. The much faster valley relaxation in $MoSe_2$ monolayer compared to monolayer $WSe_2$ is reminiscent of a close to zero valley polarisation, measured in cw-polarised photoluminescence on this material [Tor18]. All in all, it can be stated that for $MoSe_2$, the valley relaxation depends strongly on external factors. Furthermore, the polarisation of the background carriers may lead to a long-living spin polarisation prevailing up
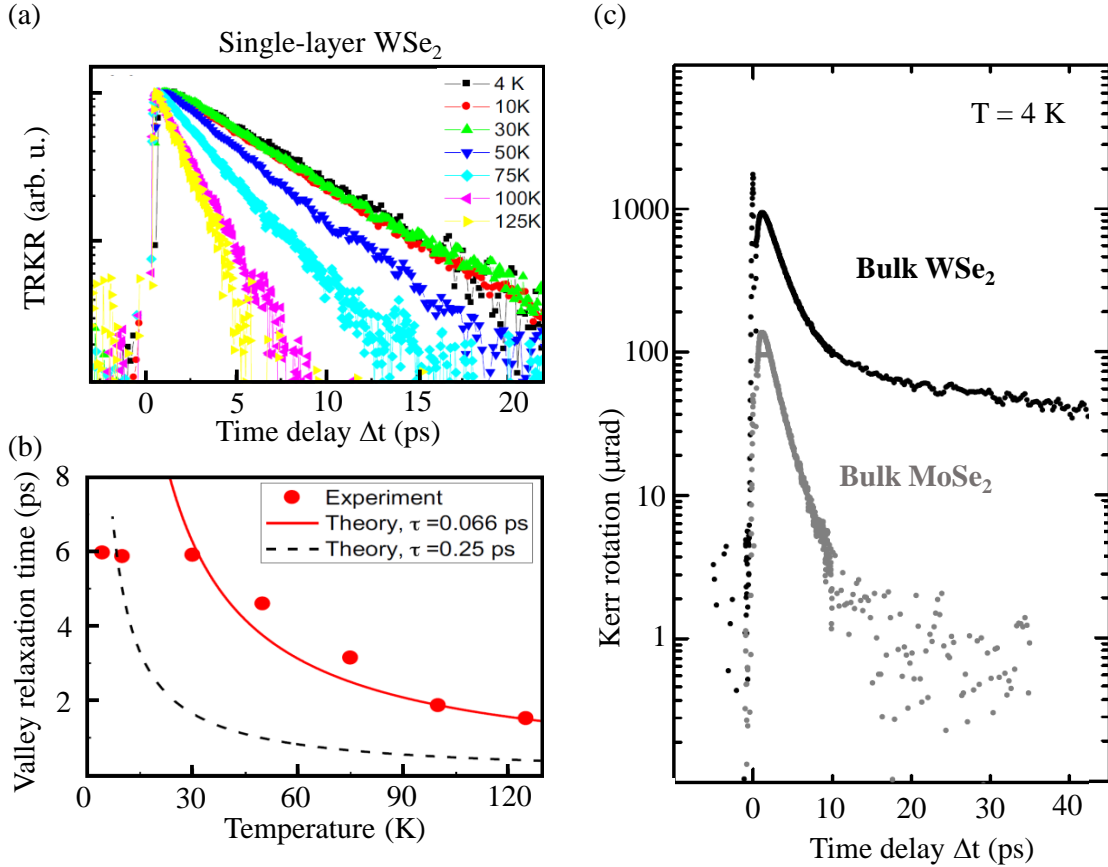
**Figure 4.3: Publications of time-resolved Kerr measurements on single- and multilayer TMDCs.** (a) TRKR measurements from single-layer $WSe_2$ on bare $SiO/SiO_2$ at an injected exciton density of $1 \cdot 10^{12}$ cm$^{-2}$ for different temperatures. (b) Corresponding valley dephasing rates from (a) modelled by Coulomb exchange interaction, including scattering on a short-range potential with presumed scattering rates $\tau$. The plots in (a) and (b) are reprinted from [Zhu14]. (c) TRKR of bulk $WSe_2$ (black) and bulk $MoSe_2$ (grey) at 4 K. Both samples consist of approximately 100 layers. Although no explicit numbers are given, the estimated valley relaxation times apparently amount to a few picoseconds concerning the fast initial decay. Figure adapted from [Gui18].

to a few nanoseconds.

Turning towards the multilayer samples, rather similar dynamics for both materials can be found. For multilayer $WSe_2$ (cf. figure 4.2(c)), valley relaxation significantly speeds up, exhibiting decay constants of $\tau_{TRFE} = 1.6 \pm 0.5$ ps and $\tau_{TRFE} = 1.9 \pm 0.5$ ps for $\sigma^+$ and $\sigma^-$ polarisation. The obtained valley relaxation times are in good accordance with the findings of Guimaraes et al., performing TRKR on bulk $WSe_2$ and $MoSe_2$ [Gui18]. Although no explicit numbers are given in the publication, similar relaxation times for both of less than 5 ps can be read out from the graph (cf. figure 4.3(b)).

Interestingly, valley relaxation slows down for multilayer $MoSe_2$ with decay times

of 1.8 ± 0.5 ps for both polarisations. The key to disentangle the underlying principles for the differences in lifetime and valley relaxation times hides within the valley structure of the regarded material systems. First, it has to be noted that monolayer $MoSe_2$ is the only material where the lowest energy exciton state is bright. Moreover, the spin-dark exciton state ranges only 1.5 meV higher [Lu20]. Due to the small energy separation and the coupling of the dark and bright exciton branches next to their degeneracy points, a fraction of dark excitons within the same valley can evolve during thermalisation [Yan20]. In contrast, the spin-forbidden exciton in monolayer $WSe_2$ is about 40 meV lower in energy than the bright exciton [Zha17; He20]. For both materials, the CB level of the $\Sigma$ valley is about equal to the level of the K valleys [Ram12; Hsu17; Mad20]. Accordingly, exciton-phonon interaction occurs. As discussed in chapter 2.2.2, phonons mediate an electron transfer from K to $\Sigma$ [Hos15; Cho17; Raj18; Wal21]. For homobilayers of both materials, the band gap becomes indirect because $\Sigma$ is lower in energy than K [Zen13; Ter14; Yeh15] and the exciton-phonon scattering is strongly enhanced [Raj18; Hel21]. Nonetheless, the optical transition occurs still from K to K. TR-ARPES experiments, as discussed the section before, monitor an ultrafast electron transfer from K to $\Sigma$ [Bus19; Don21]. Meanwhile, the holes remain in K as the phonon coupling to the states at $\Gamma$, which is shifted upwards in energies for multilayers, is very small [Mad20].

 With this considerations, the results from transient differential transmission and TRFE can be put in a reasonable context. Schematically, this is sketched in figure 4.4. Please note that in this figure, the relaxation processes for each regarded material system are displayed for only one specific spin orientation. As time-reversal symmetry dictates, the dispersion of excitons with opposite spin configuration is degenerate under simultaneous exchange of $K^+$ and $K^-$ and therefore equally valid for reversed indices. Moreover, K' is used to name the opposite valley, regardless of its specific valley index.

In monolayer $WSe_2$, the excitons' electrons can be transferred under the emission of phonons to $\Sigma$ or K' since those are spin-allowed and energetically favourable. In addition, the spin-forbidden exciton state in the same valley is populated. Thermalisation therefore causes multiple dark exciton states with the hole left in the genuine K valley. Due to their dark character, the excitons are comparably long-lived. The residual hole at the pumped K valley bleaches the investigated bright excitonic transition. The entire process is visualised in figure 4.4(a).

For monolayer $MoSe_2$, the dynamics are very different. The spin-conserved state in K' is higher in energy and thus not accessible under phonon emission. A direct transfer from K to $\Sigma$ is rather improbable due to the large spin splitting with
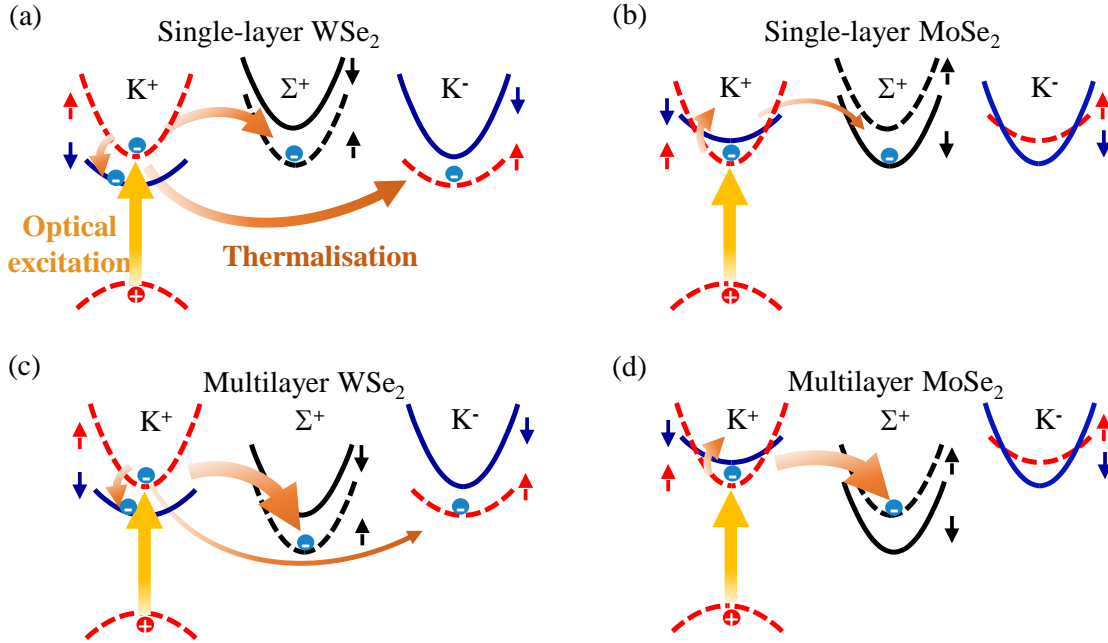
**Figure 4.4: Valley relaxation dynamics explained within a schematic valley landscape for mono- and multilayer MoSe$_2$ and WSe$_2$.** In all cases, the optical excitation of the K$^+$ valley has been chosen to keep the consideration most simple. The small vertical arrows denote the spin character of the respective band. Due to the large spin splitting in the VB, the hole states can be assumed to remain in the genuine K valley. (a) In single-layer WSe$_2$, thermalisation facilitates the formation of spin-dark excitons, as well as the creation of a momentum-dark exciton population with electrons residing in $\Sigma$ and K′, mediated by the emission of phonons. (b) In monolayer MoSe$_2$, the exciton state lowest in energy is bright. The relaxation to the opposite valley is strongly quenched since this process requires additional energy or a spin flip. Moreover, the transfer to $\Sigma$ is not spin-conserving and therefore very small. The only relaxation mechanism is the Rashba-type coupling between bright and dark excitons within the same K valley [Yan20]. The dark excitons can be transferred $\Sigma$. Thus, the dynamics are dominantly governed by the bright exciton state, giving rise to faster dynamics than in the other considered systems. (c),(d) In multilayer systems, the $\Sigma$ valley provides the overall lowest energy state for the electrons. Consequently, the dynamics in multilayers are determined by the momentum-indirect $\Sigma$ valley excitons and thus exhibit a very similar temporal evolution.

reverse ordering. However, a finite population in the upper band owed to the Rashba-type coupling of the bright and dark exciton branch [Yan20] may be created which subsequently can also form $\Sigma$ - K excitons. Consequently, no significant dark exciton population that impacts the dynamics of the bright K - K transition can form (cf. figure 4.4(b)). Thus, the injected valley polarisation diminishes fast and efficiently due to long-range electron-hole exchange interaction. Within this picture, the much faster valley relaxation in monolayer MoSe$_2$ compared to WSe$_2$

monolayer can be explained.

In the multilayer systems, the $\Sigma$ valley is by far the lowest valley in the CB, acting as the prevalent sink for the excitons' electrons. For both considered bulk materials, the formation of momentum-indirect excitons is predominant. The explicit fine structure of the CBs does not play an important role any more. As a consequence, very similar temporal dynamics can be expected (cf. figure 4.4(c) and (d)) which can also be observed in our measurements. Besides, kind of a build-up process is visible in the TRFE time trace of bulk $WSe_2$ and likewise for bulk $MoSe_2$. The underlying mechanism for this is unclear. It might be related to thermalising excitons, relaxing back into the light cone, filling the empty states left over after direct radiative recombination.

Finally, the question remains why the valley dynamics in multilayer $WSe_2$ are faster than in the single layers. A possible explanation may be that the population of K - $\Sigma$ exciton states has less impact on the pump-probe response of the bright transition than the excitons in K- K′. At first, this seems unintuitive in the electronic picture as both exciton species possess a hole residing at K. However, from the exciton picture, it appears more reasonable that the K - $\Sigma$ exciton states have fewer impact on the K - K transition since they are energetically more apart. Conclusively, it is found that the interaction of multiple layers cause a significant impact on the valley relaxation dynamics compared to a single layer, altering the relaxation times up to one order of magnitude. The different relaxation times of mono- and multilayer as Mo- or W-based TMDCs are set into a comprehensive framework by considering the valley- and exciton fine structures, as well as the layer-dependent lowering of the $\Sigma$ valley.

## 4.2.1 Valley dynamics of monolayer TMDCs in magnetic fields

As a next step, the original approach of Michael Faraday is followed, investigating the influence of magnetic fields on the polarisation of the light passing through a particular material. In out-of-plane orientation of the magnetic field, the TMDCs' K valleys shift with respect to their valley index, thus breaking the energy degeneracy. For single-layer $MoSe_2$ and $WSe_2$, the effective excitonic g factor is about $g_\perp \approx$ -4, translating to a valley splitting of approximately 0.2 meV/T [Li14]. In parallel orientation of the magnetic field with respect to the monolayer plane, theory as well as experiments evidence a g factor of $g_\parallel \sim 0$ [Zha17; Kat20]. Yet an enhanced coupling of the bright and spin-dark excitonic states emerges [Zha17; Rob17]. Accordingly, the valley polarisation dynamics in monolayer TMDCs are expected to be altered in the presence of out-of-plane magnetic
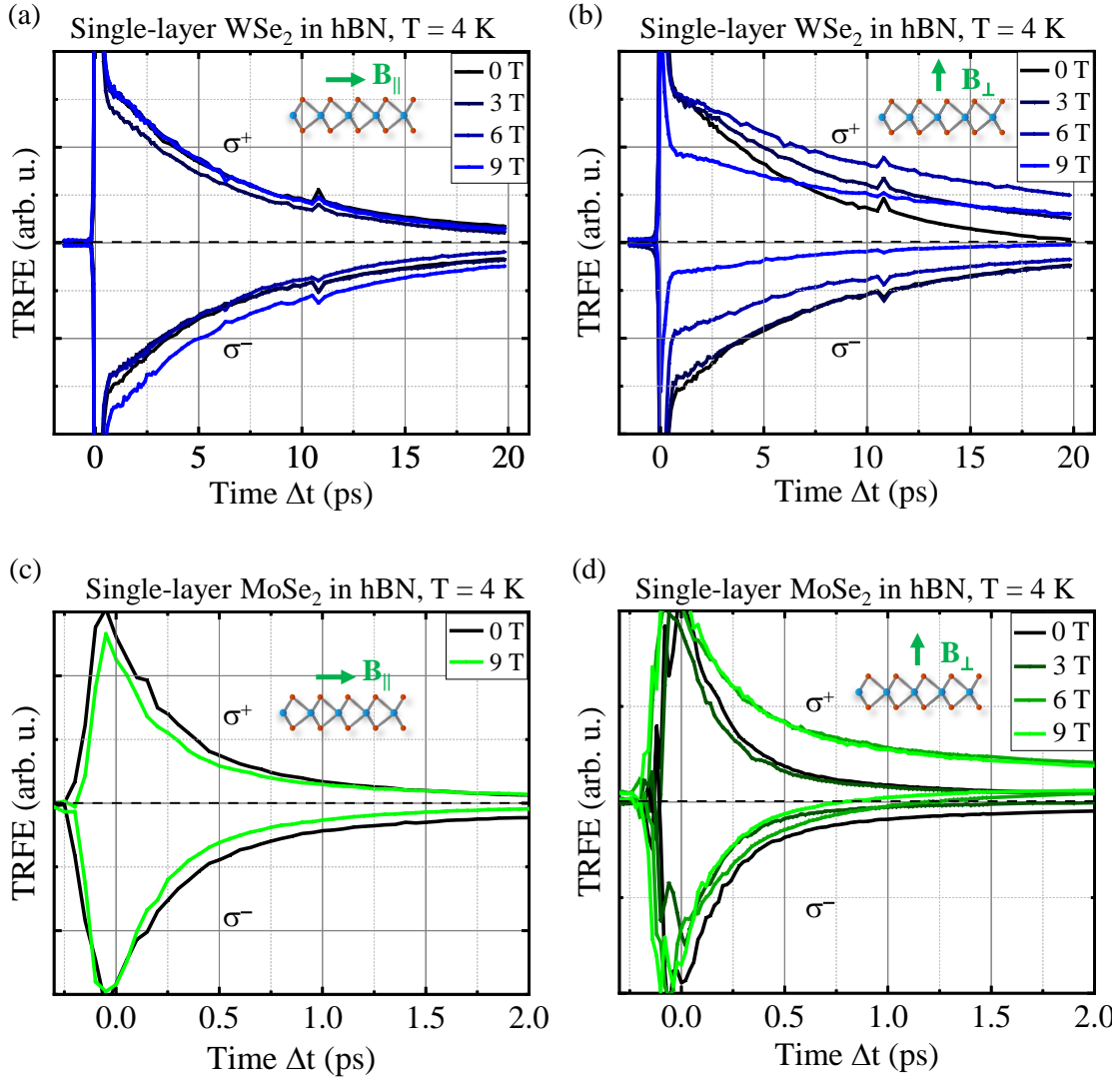
**Figure 4.5: TRFE on single-layer WSe$_2$ and MoSe$_2$ in the presence of magnetic fields.** (a) TRFE on WSe$_2$ exposed to in-plane magnetic fields. No systematic magnetic field dependence can be observed. The differences arise from the individual realignment which is needed when the magnetic field is altered. (b) TRFE on WSe$_2$ in out-of-plane magnetic fields. After thermalisation ($\Delta t > 1$ ps), the TRFE amplitude increases systematically with B. This behaviour can be related to the valley Zeeman splitting, rendering one of the valleys energetically favourable. Besides, the slopes of the TRFE traces softly decrease with increasing magnetic fields which probably is owed to a reduction of the electron-hole long-range exchange interaction that is the main driving process for valley depolarisation. (c) TRFE on MoSe$_2$ exposed to in-plane magnetic fields. The comment of (a) holds equally for MoSe$_2$. (d) TRFE at applied out-of-plane magnetic fields measured on MoSe$_2$. In principle, a similar behaviour as for WSe$_2$ is perceivable, following the same mechanisms as stated in (b).

fields, while no significant change for in-plane magnetic fields should be recordable.

Figure 4.5 presents TRFE measurement on single-layer WSe$_2$ and MoSe$_2$ for in- and out-of-plane magnetic fields up to 9 T. For each step of the magnetic field, the sample position and the focus had to be readjusted. As a result, the absolute amplitudes vary slightly and have to be interpreted with care. The data is not normalised in order to preserve all information about the original intensity. Exponential fitting either way captures the decay dynamics properly. Plots 4.5(a) and (c) show data sets of TRFE on monolayer WSe$_2$ and MoSe$_2$ exposed to in-plane magnetic fields. Apparently, the shape of the TRFE traces for different field strengths does only vary within the error margin. No systematic change is perceivable. For MoSe$_2$, only the data for 0 T and 9 T have been recorded to verify this. In contrast, the impact of out-of-plane magnetic fields becomes visible in TRFE. Starting with monolayer WSe$_2$ (cf. figure 4.5(b)), it is most notable, that the amplitudes of the valley polarisation change. While direct radiative recombination stays basically unchanged, the TRFE amplitude at $\Delta$t > 1 ps increases consistently with rising magnetic fields. For longer times ($\Delta$t > 10 ps), the TRFE traces converge to a non-zero value regardless of the initial pump polarisation, indicating a long-lived valley polarisation component. Similar systematics are perceivable for single-layer MoSe$_2$ (shown in figure 4.5(d)) even though these appear to be less consistent. The less systematic evolution of the data may be caused by the comparably small energy separation of the bright and dark exciton states in MoSe$_2$. Changing the polarity of the magnetic field, leads to the same results but with a change in the sign ot the TRFE signals which is equivalent to an exchange of valley indices (data not shown).

For a quantitative comparison, all data sets have been fitted with a single-exponential decay function. The obtained decay constants are presented in figure 4.6. The unchanged decay times evidence that the valley dynamics are not impacted by in-plane magnetic fields. For out-of-plane orientation of the magnetic field, decay times are slightly increasing. However, the increase of the valley relaxation time turns out to be less pronounced as the TRFE traces in figure 4.5 might suggest. For WSe$_2$, a distinguishable difference in the valley relaxation times for $\sigma^+$ and $\sigma^-$ pump polarisation is found (cf. figure 4.6(a)). Alike, the findings in MoSe$_2$ show a faint increase of the relaxation times (cf. figure 4.6(b)) even though, no explicit polarisation dependence is visible. Note that the impact of the diamagnetic shift, causing a total shift of the regarded transitions ($\propto B^2$), plays a negligible role because the shift counts about 1 meV for less than 10 T [Kat20] in contrast to the laser pulses widths' of about 25 meV (FWHM).

For the interpretation of the valley dynamics, the interplay of long-range Coulomb interaction and the valley Zeeman splitting is considered. As discussed in chap-
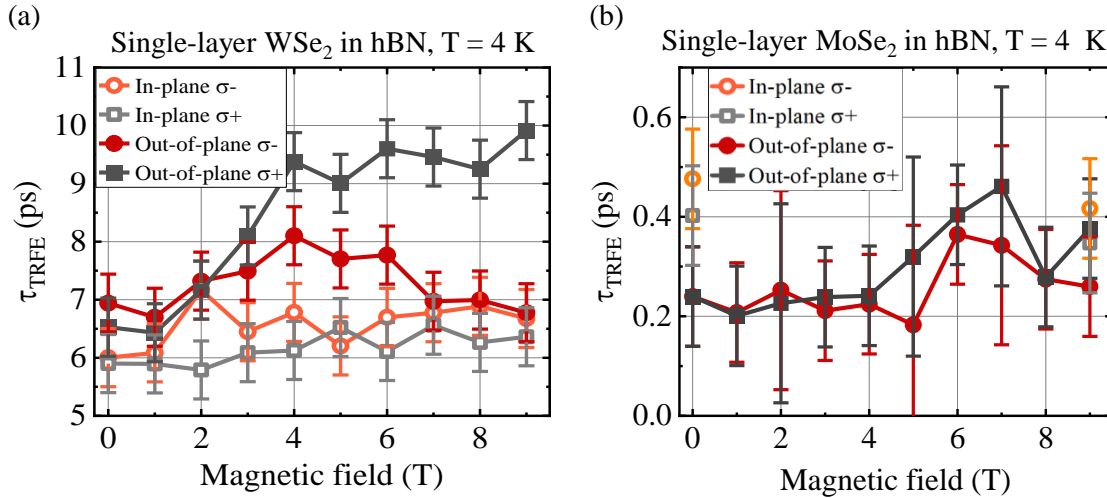
**Figure 4.6: Magnetic field dependence of the valley relaxations times of monolayer WSe$_2$ and MoSe$_2$.** The data is obtained from mono-exponential fitting of the TRFE traced presented in figure 4.2. For in-plane magnetic fields, the valley relaxation times are barely affected, reflecting an effective g factor of $g = 0$. (a) For monolayer WSe$_2$, out-of-plane magnetic fields give rise to an increase of the valley relaxation times which can be linked to the valley Zeeman splitting, lowering the energy of K$^+$ compared to K$^-$ and therefore improving the according valley lifetime. (b) In monolayer MoSe$_2$, no obvious dependence on the pump polarisation can be observed. Overall, a soft prolongation of the relaxation times can be perceived.

ter 2.2.2, LRX has been proclaimed to be the main process for valley relaxation [Gla14; Yu14; Zhu14; Hao16b]. It is viable to assume a maximal efficiency of LRX when K and K$'$ are degenerate since the virtual process of an exciton recombining in one valley and being created simultaneously in the opposite valley requests equal energy levels of both states. Accordingly, LXR can be expected to be less efficient for non-degenerate valleys, leading to a general increase of the valley relaxation times. The remarkable increase of the valley relaxation times with rising magnetic fields for $\sigma^+$ pump polarisation can be related to the valley Zeeman shift, hampering the excitons in the down-shifted valley to be transferred to the energetically up-shifted valley. The absence of the polarisation dependence on the valley relaxation in monolayer MoSe$_2$ may originate from the small energy separation of the bright and dark excitons as well as the coupling between both [Yan20].

The cause for the non-zero TRFE signal for longer delay times ($\Delta t > 10$ ps) at higher magnetic fields can be ascribed to spin-polarised resident carriers which accumulate in the energetically lowered valley [Gla12; Hsu15; Dal15; Sch17]. It should be emphasised that this is strongly dependent on the individual sample,

i.e. on the intrinsic doping by impurities and defects.

In general, it has not been easy to reproduce the valley relaxation times, as well as the shift of the valley polarisation at longer delay times. Several Master and Bachelor thesis have aimed to explore the systematics of this shift [Hir20; Fel22; Buc23]. The measurements are subjected to unavoidable variations of the sample position, focus and polarisation which is owed to the realignment of the setup for every magnetic field step. Consequently, it has been attempted to overcome these inconveniences in the data analysis. Normalisation of the data for the maximum amplitude as well as for thermalised population at around $\Delta t = 1$ ps has not been useful to overcome this issues.

In conclusion, the fingerprints of the valley Zeeman shift manifest in the spin/valley relaxation dynamics by a larger valley polarisation in the energetically lowered valley and also in a soft prolongation of the valley relaxation times. This effect can be explained by the interplay of valley Zeeman splitting and LRX. The cause for the long-lived TRFE signals at higher magnetic fields can be related to an accumulation of spin-polarised resident carriers.

## 4.2.2 Valley dynamics of CVD-grown monolayer WSe$_2$

In our experimental setup for the pump-probe experiments, it has been hardly feasible to investigate CVD-grown TMDC samples so far. The two reasons for that are the reduced optical quality of the CVD-grown samples and much more demanding, the size of the sample, covering the large laser focus of 50 microns. Antony George from the Turchanin group of the University of Jena accomplished to grow single-layer WSe$_2$ flakes with a lateral size up to 50 μm which he kindly provided to us. Along with the hot-pick-up method [Pur18] that allows to improve the sample quality by removing the flake from the growth substrate and intercalating it in smooth hBN protection layers, this enables investigations in the split coil cryostat.

The Faraday measurements conducted on the CVD-grown sample reveal an approximately five times weaker signal with a lot of noise imprinted, but the data is still reliable enough to be evaluated with mono-exponential fits. In figure 4.7, data sets for out-of-plane magnetic fields and the respective valley relaxation times are depicted. It must be mentioned that it was not possible to adjust the setup properly for $\sigma^+$ polarised pump pulse excitation. Therefore, only results with $\sigma^-$ polarised excitation are discussed here. The valley relaxation times are found to be half as long as for the exfoliated sample. As intuition predicts, carrier lifetimes, as well as the valley dynamics are expected to be shorter for a sample with a less
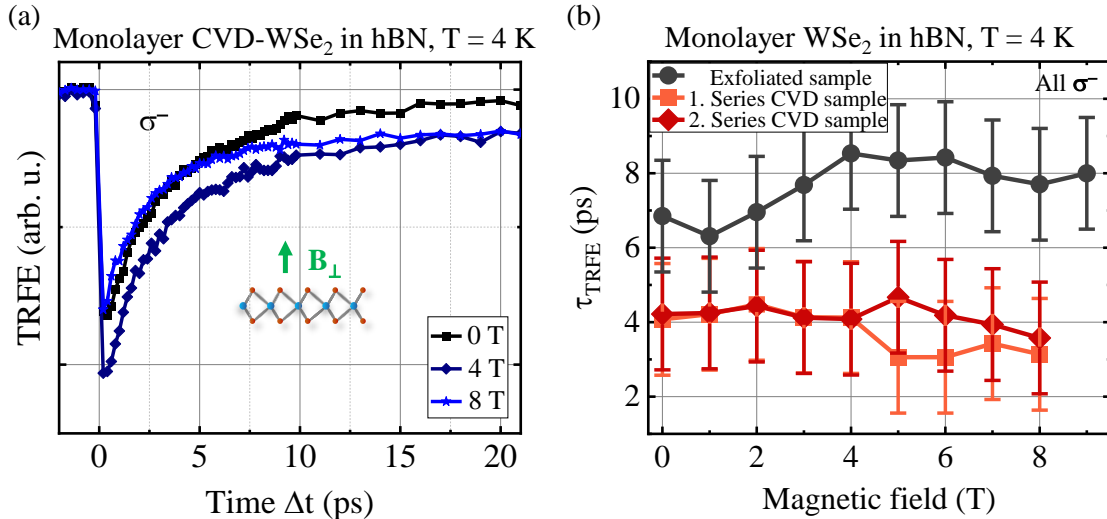
**Figure 4.7: Comparison of the valley dynamics in CVD-grown and exfoliated single-layer WSe$_2$.** (a) TRFE traces at out-of-plane magnetic fields up to 8 T for $\sigma^-$ polarised excitation in CVD-grown single-layer WSe$_2$. (b) Valley relaxation times obtained by fitting the TRFE curves with a mono-exponential fit. Valley relaxation appears to be twice as fast in the CVD-grown sample compared to the exfoliated monolayer. The difference in valley relaxation can be traced back to the strongly reduced exciton lifetime in the CVD sample.

perfect crystal structure. However, the question poses whether the crystal imperfections cause exclusive population decay or also a pure dephasing of the valley pseudospin, i.e. valley relaxation without loss of population which is denoted by $\tau_{valley}$. In order to separate both effects, Matthiesen's rule is applied. Accordingly, the extracted lifetime of $\tau_{life} = 6.8$ ps from the transient differential transmission measurements (presented figure 4.1 (c)) and the relaxation time of $\tau_{TRFE} = 4.2$ ps from TRFE are evaluated:

$$\frac{1}{\tau_{valley}} = \frac{1}{\tau_{TRFE}} - \frac{1}{\tau_{life}} \tag{4.1}$$

As a result, a value of $\tau_{valley} = 10.6 \pm 1$ ps is obtained. This perfectly coincides with the value of $\tau_{valley} = 10.6 \pm 1$ ps that is retrieved by the same approach on exfoliated WSe$_2$. The unperturbed valley dephasing time underpins the resilience of the valley pseudospin in less perfect TMCD crystals, showing that the valley dynamics are exceptionally robust and independent of the sample quality and also persist in CVD-grown samples. This remarkable finding affirms the potential application of industrially fabricated devices for spin-/valleytronics.

### 4.2.3 Ultrafast pseudospin quantum beats in multilayer WSe$_2$ and MoSe$_2$

The results, presented in this section have partially been published in our paper about 'Ultrafast pseudospin quantum beats in multilayer WSe$_2$ and MoSe$_2$' [Rai22].

In the section before, it has been shown that in-plane magnetic fields do not impact the valley dynamics of monolayer MoSe$_2$ and WSe$_2$. The TRFE experiments conducted on the respective multilayer samples reveal a strikingly different behaviour. To start the discussion, an exemplary TRFE measurements on bulk WSe$_2$ exposed to in- and out-of-plane magnetic fields of 0 T and 6 T is presented in figure 4.8. The excitation energy has been tuned to the resonance of the A$_{1s}$ exciton transition that has been determined from the white-light reflectance measurements (cf. section 3.1.4). For out-of-plane orientation, the dynamics of the TRFE signal are similar to the one of monolayer WSe$_2$. The enhanced TRFE signal at B = 6 T compared to B = 0 T can be related to the valley Zeeman shift, augmenting the exciton density in the energetically lowered valley, as discussed elaborately in the section before. In stark contrast, very pronounced oscillations appear on the TRFE signal in the presence of in-plane magnetic fields. This phenomenon can be likewise found for MoSe$_2$ as well as for both circular polarisations of the pump pulse. In order to investigate the origin of the oscillatory behaviour, a series of TRFE measurements for different excitation energies at a fixed in-plane magnetic field of B = 6 T has been conducted on multilayer WSe$_2$ and MoSe$_2$, which are presented in figure 4.9(a) and (c), respectively. Effectively, the laser energy has been scanned over the spectral window where excitonic transitions have been found in reflectance which is presented in the upper part of figures 4.9(b) and (d), indicating also the peak positions obtained from the transfer-matrix approach. For simplicity, only $\sigma^+$ polarised measurements are shown in the following. For both materials, oscillations appear in the TRFE signal when the laser energy is in resonance with the A$_{1s}$ and the A$_{2s}$ exciton transitions. The amplitude of the second oscillation cycle is evaluated and plotted against the central laser energy. For WSe$_2$, the found values can very accurately be described by a fit of two Gaussians (cf. figure 4.9(b)), which nicely resemble the relative strength in absorption obtained from the transfer-matrix modelling of the reflectance (not shown). The larger width of the resonances compared to the one obtained from the transfer-matrix modelling is owed to the spectral width of the laser pulse (25 meV). More precisely, the evaluated data features a convolution of the excitonic transitions and the laser pulse. It has to be mentioned that the A$_{1s}$ resonance position is
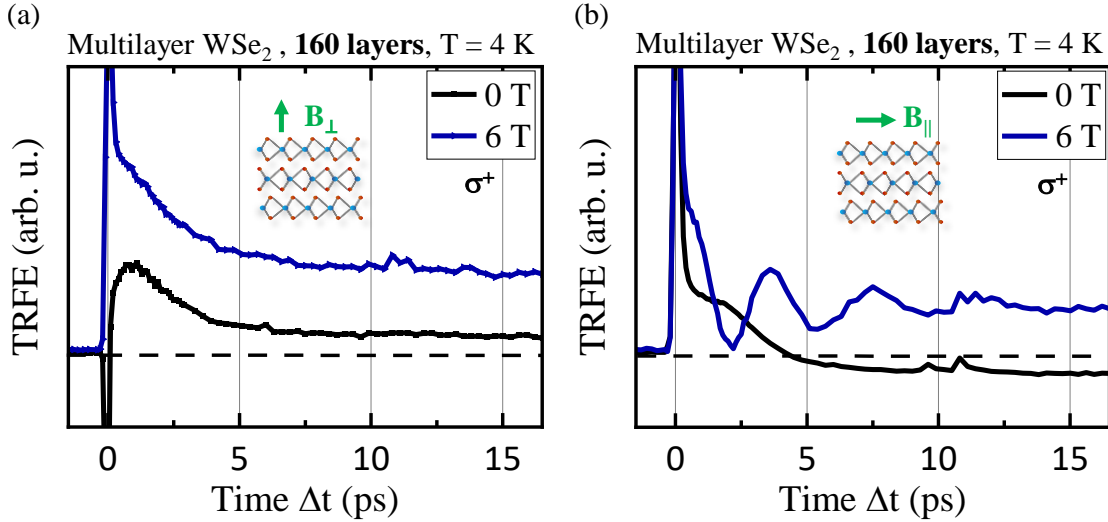
**Figure 4.8: TRFE on multilayer WSe$_2$ exposed to in- and out-of-plane magnetic fields.** The sample is resonantly excited on the A$_{1s}$ exciton transition. (a) For out-of-plane orientation, an increase of the valley polarisation for B $= 6$ T compared to B $= 0$ T can be observed. (b) For parallel orientation, the TRFE signal exhibits strong temporal oscillations, setting in after $\Delta$t $> 1$ ps. The amplitude of the oscillation diminishes on the same time scale as the TRFE signal at B $= 0$ T.

shifted by about 16 meV to lower energies in comparison to the peak position from the transfer matrix model. This may be attributed to bandgap renormalisation effects [Ste17] and/or a temperature increase under pulsed excitation. The measurements on multilayer MoSe$_2$ reveal a precise agreement of the transitions found in reflectance and the maximal oscillation amplitude in TRFE (cf. figure 4.9(d)).

Next, the influence of the magnetic field strength on the undulating TRFE signal is examined. To do so, measurement series from 0 - 9 T under resonant excitation of the A$_{1s}$ and A$_{2s}$ transitions, as determined from the before discussed energy scans, have been conducted. The according TRFE data are presented in figure 4.10 and 4.11, exciting on the A$_{1s}$ and A$_{2s}$ exciton transitions, respectively. Apparently, the modulation of the TRFE signal can be perceived for fields larger than 2 T. With increasing strength of the magnetic field, the oscillations appear more pronounced. Moreover, the oscillation frequency shortens at higher fields. It turns out that the oscillation frequency scales linearly with the strength of the magnetic field. Furthermore, the oscillation period of the MoSe$_2$ multilayer is slightly longer than for multilayer WSe$_2$. The spikes, occurring at $\Delta$t $\sim 6$ ps and 9 ps, stem from reflexes of the excitation pulse on optical elements in the setup. Before diving into the analysis, it is vital to comprehend the origin of the oscilla-
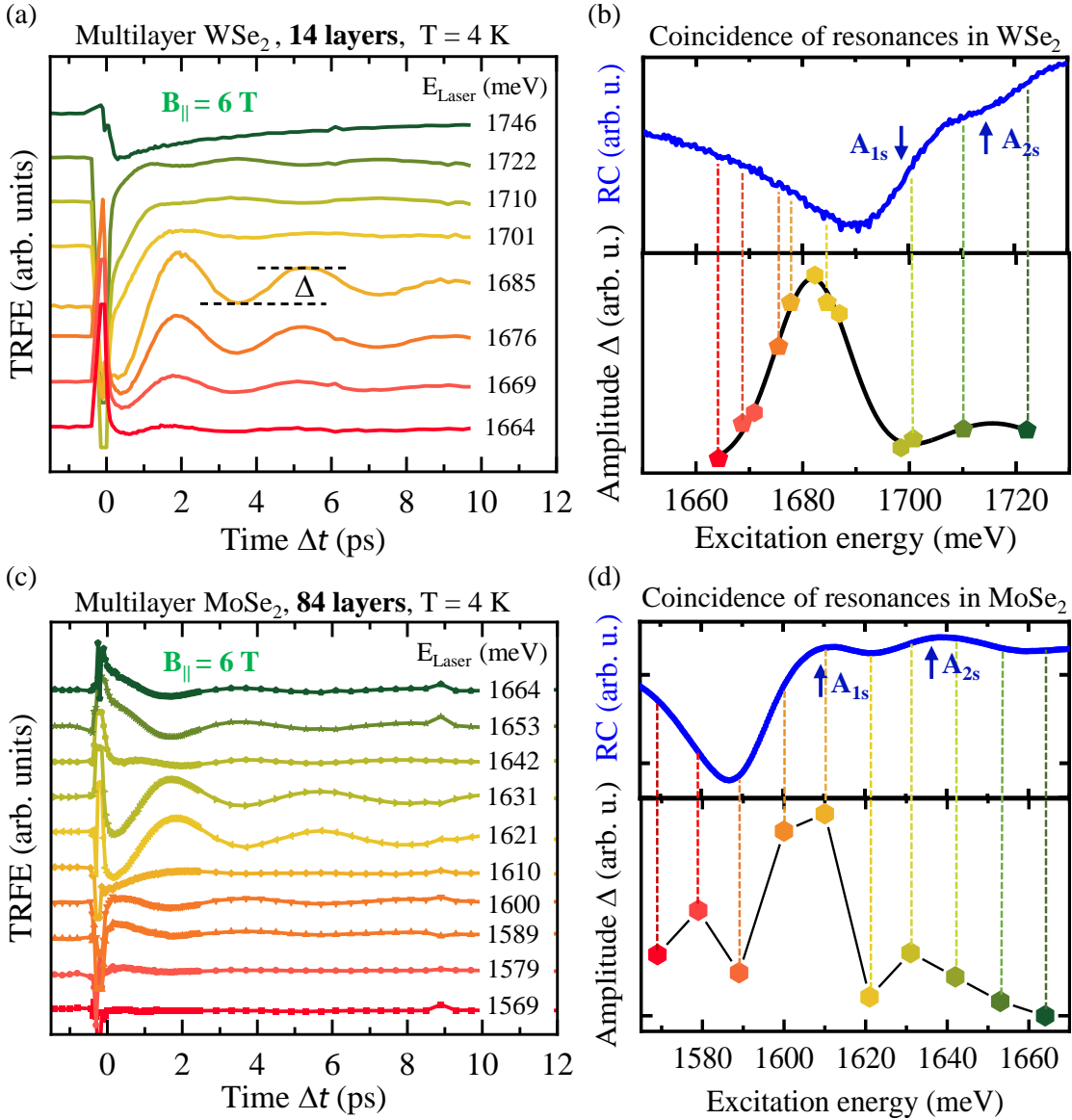
**Figure 4.9: Spectral dependence of the oscillations on the TRFE signal of multilayer WSe$_2$ and MoSe$_2$ at an in-plane field of B = 6 T.** The excitation energy is scanned over the spectral window where the excitonic resonances of WSe$_2$ (a) and MoSe$_2$ (c) are located. For certain energies, an oscillation appears in the TRFE signal. (b), (d) By plotting the according amplitudes $\Delta$ against the central laser energy, one can clearly identify two resonances in both materials. The reflectance spectra RC and the according peak positions, retrieved from the transfer-matrix approach (blue arrows), are for comparison plotted in the upper part of (b) and (d). For WSe$_2$, the maximum oscillation amplitudes from TRFE can be fitted with a double-Gaussian curve (solid black line, (b)). However, there is a mismatch of 16 meV with respect to the values from reflectance. (d) For MoSe$_2$, the amplitude of the oscillations perfectly reproduce the peak positions of the A$_{1s}$ and A$_{2s}$ excitons that have been found in reflectance.
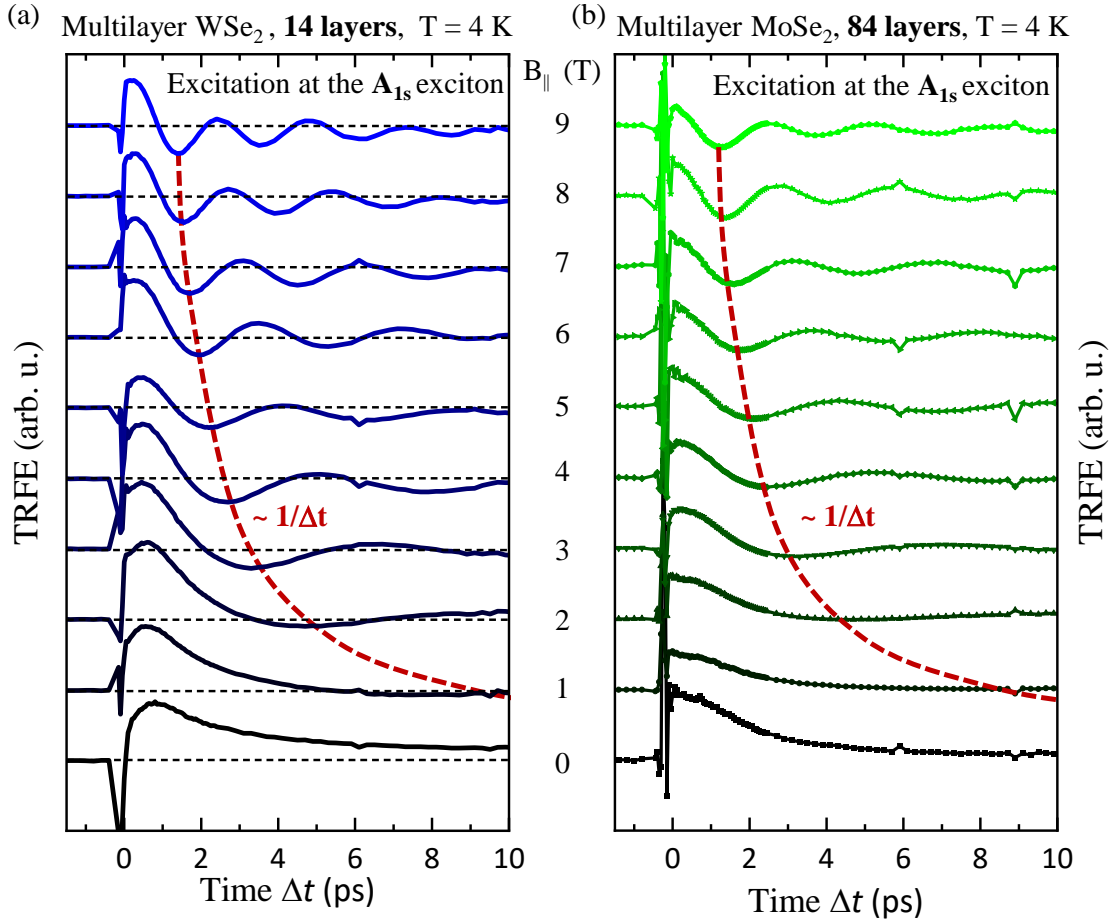
**Figure 4.10: TRFE on multilayer WSe$_2$ and MoSe$_2$ exposed to in-plane magnetic fields exciting resonantly on the A$_{1s}$ exciton transition.** Strong temporal oscillations appear whose frequencies increase linearly with the strength of the magnetic field, which is implicated by the dashed lines, depicting a $1/\Delta t$ function.

tions. In principle, the change of the sign of the TRFE signal can be interpreted as a back and forth swapping of the overall valley polarisation from K to K′ (cf. figure 4.12(a)). In other words, the excitons' pseudospin is alternating between $\tau \pm 1$. More elaborate, the electrons' and holes' spin orientation is principally out-of-plane with respect to the layers which is also evidenced in the calculations of our paper [Rai22], presented in table 2.1. The strong in-plane magnetic field leads to a coupling of the states in K and K′ and thereby causes a softening of the selection rules regarding spin [Zha17; Mol17]. This permits that the exciton population coherently oscillates between the Zeeman-split exciton states with opposite valley indices. A schematic representation thereof within the exciton dispersion is shown in figure 4.12(c). Conceptually, the coherent oscillation of the excitons' pseudospin can be regarded as a Larmor precession of the excitons' magnetic moment revolving around the external magnetic field vector as sketched in
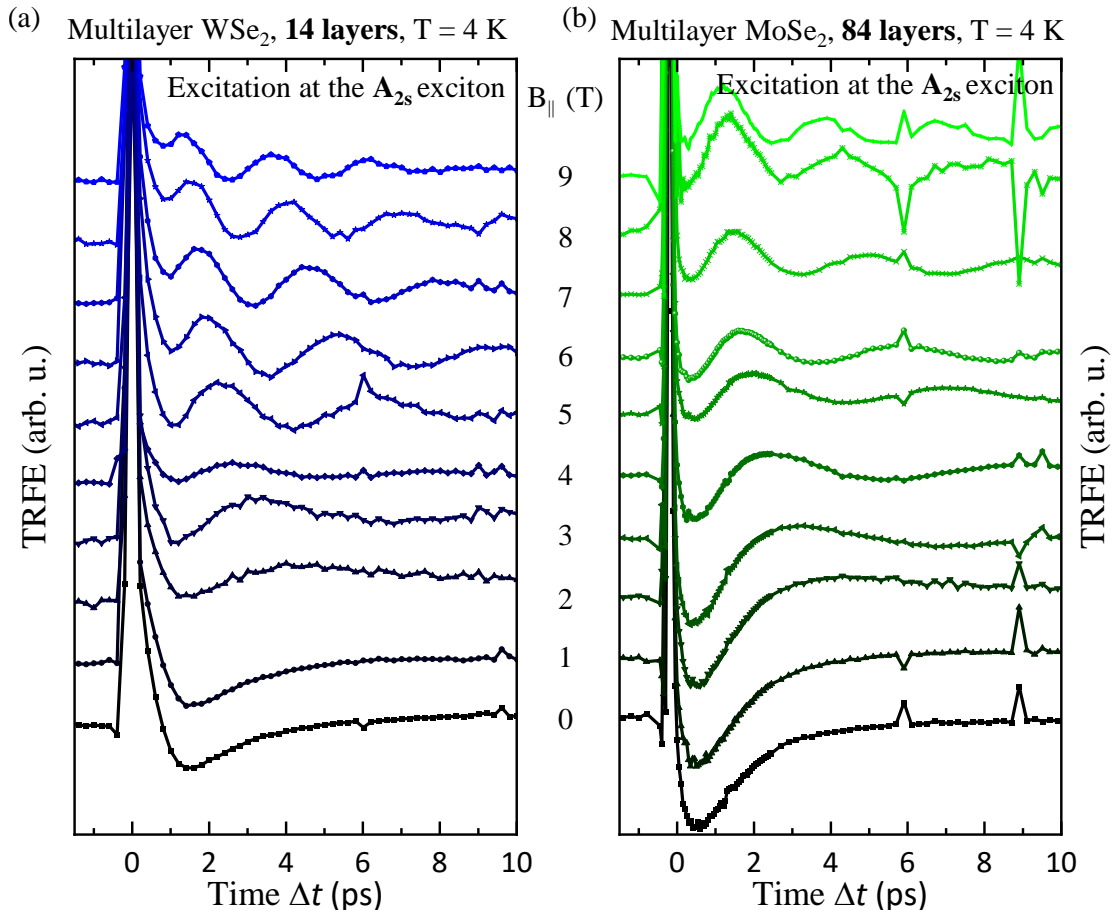
**Figure 4.11: TRFE on multilayer WSe$_2$ and MoSe$_2$ exposed to in-plane magnetic fields exciting resonantly on the A$_{2s}$ exciton transition.** Analogously to the former graph, clear oscillations appear. However, the intensity of the oscillation is less pronounced compared to those, excited at the A$_{1s}$ resonance. The spikes, appearing at $\sim 6$ ps and 9 ps, stem from reflexes of the excitation pulse.

figure 4.12(b). The external magnetic field $\vec{B}$ exerts a torque $\vec{M}$ on the magnetic moment $\vec{\mu}$:

$$\vec{M} = \vec{\mu} \times \vec{B} = g \cdot \vec{J} \times \vec{B} \tag{4.2}$$

Here, $\vec{J}$ denotes the total angular momentum which is composed of the excitons spin $\vec{S}$ and the orbital angular momentum $\vec{L}$. The effective g factor $g$ is composed by contributions from orbital angular momentum and spin. The calculations reveal that the major contribution to the in-plane g factor originates from an in-plane spin component in the valence band that is only present in bulk materials (cf. table 2.1). The precession frequency $\omega_{Larmor}$ is given by the energy difference of the two quantized states with $\tau = \pm 1$. Correspondingly, $\omega_{Larmor}$ extends to
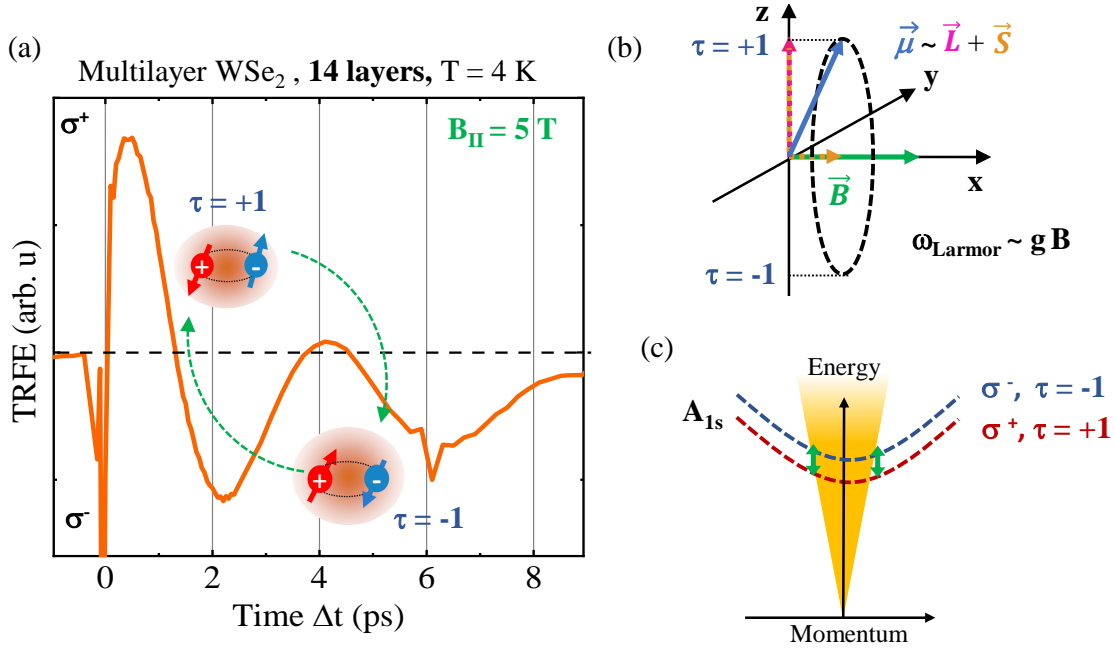
**Figure 4.12: Underlying principle of the oscillations in TRFE that appear in multilayer TMDCs exposed to in-plane magnetic fields.** (a) Typical oscillations on $WSe_2$ for $B_{||} = 5$ T. After $\sigma^+$ excitation, the TRFE trace starts to oscillate. The change of the sign of the TRFE signal indicates that the overall valley polarisation is swapping back and forth from $K^+$ to $K^-$ which implies a coherent oscillation of the excitons' pseudospins between $\tau = \pm 1$. (b) The oscillations can be regarded as a damped Larmor precession of the exciton's total magnetic moment $\vec{\mu}$ around the external magnetic field $\vec{B}$. The Larmor frequency scales with the g factor. TRFE monitors the z component of the precession with the according values of $\tau = \pm 1$. (c) Visualisation of the oscillating pseudospin in the exciton dispersion. The exciton population oscillates between the Zeeman-split $A_{1s}$ exciton states (or $A_{2s}$, depending on the respective excitation energy) with opposite valley indices.

300 - 400 GHz at $B_{||} = 9$ T, depending on the regarded material. According to Larmor's theorem, the precession frequency is independent of the angle between the magnetic moment and the external field. A detailed investigation of the angle dependency is given two sections ahead in 4.2.3. Note that the here presented measurements exploit the polar Faraday effect which is exclusively sensitive to the z component of the magnetisation [Stö06]. Besides, the envelope of the oscillating signal diminishes approximately with the same decay time $\tau$ as the excitonic TRFE signal at $B_{||} = 0$ T. This corroborates the assumption that the oscillations arise from a damped Larmor precession of the excitons' magnetic moment. In combination with the rather short time scales far apart from the nanosecond time regime, it can be excluded that the oscillations stem from spin-polarised ensembles of background charge carriers, as observed for localised electrons in $MoS_2$

and WS$_2$ monolayers [Yan15a; Dey17; Hsu15]. Moreover, the independence of the decay time of the TRFE signal from B$_{||}$ indicates that g factor fluctuations do not occur. Otherwise, a $1/$B$_{||}$ dependence of the decay time would be expected [Yan15b; Zhu20].

Similar effects to the here discovered pseudospin quantum beats have been observed in other semiconductor systems like electron spins in n-doped GaAs bulk [Kik98], hole spins in GaAs quantum wells [Gra14], or localised background charge carriers in MoS$_2$ and WS$_2$ [Yan15b], among many other examples.

In conclusion, the here found oscillations can be attributed to excitonic quantum beats of the Zeeman-split exciton levels in K and K$'$, evidencing that for multilayer TMDCs, the excitonic in-plane g factor is non-zero.

**Determination of in-plane g factors for multilayer WSe$_2$ and MoSe$_2$.**

The clear oscillations on the TRFE time traces allow for a very accurate determination of the oscillation period $T$. From the corresponding precession frequency $\omega_{TRFE} = \omega_+ - \omega_-$, the concomitant energy splitting $\Delta E$ between the exciton states with opposite pseudospin $\tau = \pm 1$ can be inferred by:

$$\Delta E = \hbar(\omega_+ - \omega_-) = \frac{h}{T}. \tag{4.3}$$

Since $\Delta E = \mu_B \, g_{eff} \, B$ describes the valley Zeeman shift, a precise determination of the oscillation period is crucial to extract the effective in-plane g factors. An exponentially damped cosine function $F(\tau, T) \propto \exp(\Delta t/\tau) \cdot \cos(2\pi\Delta t/T)$ appears to be the most accurate modelling of the oscillating TRFE signal. An illustration of a fitted TRFE time trace is presented in figure 4.15(a). For smooth measurements with a very low noise level, the fits match the data excellently. This approach has been applied to the TRFE data sets of WSe$_2$ and MoSe$_2$ that have been acquired in steps of 1 Tesla. The retrieved frequencies are plotted against the magnetic field as presented in figure 4.13. By applying a linear fit, the effective g factor can be retrieved from the slope. Values of $g_{||} = 3.1 \pm 0.2$ and $3.4 \pm 0.2$ are found in bulk WSe$_2$ for the A$_{1s}$ and the A$_{2s}$ excitons, respectively. Analogously, values of $g_{||} = 2.5 \pm 0.2$ and $2.6 \pm 0.2$ for the A$_{1s}$ and the A$_{2s}$ excitons in multilayer MoSe$_2$ are obtained. It has to be remarked that from this approach, only the magnitude of the g factor can be derived but not its sign. Furthermore, it turns out that the g factors $g_{||}$ of the A$_{2s}$ transitions are slightly larger than those of the A$_{1s}$ excitons. Probably, this can be related to enhanced hybridisation effects. The increased spatial expansion of the 2s excitons, i.e. the larger Bohr radius may
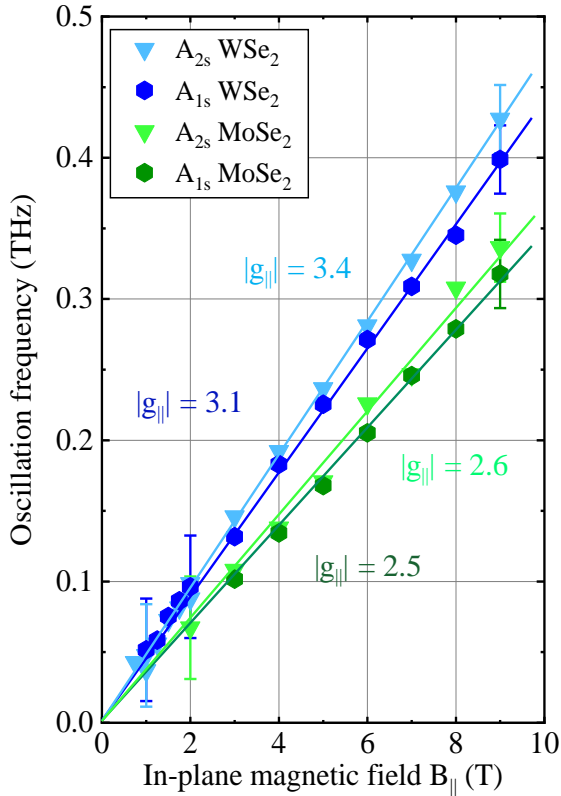
**Figure 4.13: Determination of effective in-plane exciton g factors for bulk WSe$_2$ and MoSe$_2$.** The oscillation frequencies on the TRFE signals have been extracted by an exponentially damped cosine fit. They are plotted against the in-plane magnetic field, exciting the A$_{1s}$ or the A$_{2s}$ exciton transitions (hexagons and triangles, respectively) in multilayer WSe$_2$ (blue) and MoSe$_2$ (green). Exemplary error bars for low and high fields are indicated. The here denoted g factors (error margin of $\pm 0.2$) for the respective transitions are obtained from the slope of the linear fits (solid lines). Throughout, the found values for the g factor of the A$_{2s}$ exciton transition appears to be larger than the respective values found for the A$_{1s}$ transition which may be caused by enhanced hybridisation effects.

account for a stronger involvement of hybridisation effects [Mer20].

In table 4.1, the effective in-plane g factors, determined in this work, are put in context with established values for out-of-plane field orientation and are also complemented by theoretically modelled numbers. The latter ones have been obtained by calculations based on an ab-initio approach, realised by Paulo Faría Junior. The framework of this model is discussed elaborately in chapter 2.1.3. The modelling is able to reproduce the experimentally reported out-of-plane g factors for the monolayers as well as for the multilayers. It has to be pointed out that the here applied model delivers g$_{||}$ = 0 for the monolayers. Both, spin and orbital angular momenta contributions are zero from symmetry considerations and verified numerically. For the multilayer samples, the same approach yields a non-zero g$_{||}$, attesting the experimental findings although the computed numbers are smaller than the experimentally found values. The deviation between theory and experiment may be located in the ansatz of the modelling. Even though first-principles calculations take interlayer hybridisation of electronic bands into account, the excitonic fine structure, i.e. the interplay of various types of excitons (bright, dark, grey etc.) and the resulting correlations are not regarded. As the oscillations arise form excitonic resonances, it is presumable that further hybridisation adds to the computed g factors. The investigation of excitonic correlation effects in multilayer TMDC structures turns to be rather complex and is on the

**Table 4.1: Calculated and experimentally found effective g factors.**
Computed effective g factors at the K points of the investigated materials.
The values of $g_\perp$ exp. give the range of published g factors for the respective
material systems. Paulo E. Faría Junior has conducted the calculations. The
experimental findings for $g_\parallel$ have been determined in the scope of this work
and arevpublished in [Rai22].

| | Monol. $WSe_2$ | Multil. $WSe_2$ | Monol. $MoSe_2$ | Multil. $MoSe_2$ |
|---|---|---|---|---|
| $g_\perp$ theor. | -4.10 | -2.89 | -4.30 | -1.84 |
| $g_\perp$ exp. | -4.38…-1.57 [a] | -3.4…-2.3 [b] | -4.4…-3.8 [c] | -2.7 [d] |
| $\lvert g_\parallel \rvert$ theor. | 0.00 | 0.80…1.08 | 0.00 | 1.36…1.60 |
| $\lvert g_\parallel \rvert$ exp. | **0** | $\mathbf{\pm 3.1 \pm 0.2}$ | **0** | $\mathbf{\pm 2.5 \pm 0.2}$ |

[a] [Aiv15; Sri15; Wan15a; Aro19; Liu19; För20]
[b] [Mit15; Aro18; Aro19]
[c] [Li14; Mac15; Aro19; Rob20; Wan15a; Mit16; Gor19]
[d] [Aro18]

agenda of our theory collaborator Paulo Faría Junior.

The here reported values for $g_\parallel$ are close to the published numbers for $g_\perp$ for
the respective multilayers which have been derived from magneto transmission or
reflectance measurements. For multilayer $WSe_2$, Mitioglu et al. determine an in-
plane g factor of $\lvert g_\parallel \rvert = 2.3$ for the $A_{1s}$ exciton and $\lvert g_\perp \rvert = 2.8$ for the $A_{2s}$ exciton
resonance [Mit15] (cf. figure 4.14(b)). Arora et al. report out-of-plane g factors
of $g_\perp = 3.2 \pm 0.2$ and $3.3 \pm 0.6$ for the $A_{1s}$ and the $A_{2s}$ transitions in $WSe_2$ and
$g_\perp = 2.7 \pm 0.13$ for the $A_{1s}$ resonance in bulk $MoSe_2$ [Aro18]. Reprints of these
graphs are presented in figure 4.14(a) and (c). In contrast to [Aro18], no exci-
tonic resonance has been discovered at energies above the $A_{1s}$ and $A_{2s}$ excitons
in multilayer $MoSe_2$, i.e. in the spectral region, where an interlayer exciton has
been reported (cf. figure 4.14(c)). Furthermore, Arora et al. could experimentally
and theoretically monitor the layer number dependence of $g_\perp$, starting from es-
tablished monolayer values towards multilayers with an infinite thickness [Aro19]
as presented in figure 4.14(d). Apparently, the value for $g_\perp$ is converging for more
than four layers. In this work, $g_\parallel$ for $WSe_2$ has been deduced from a sample
consisting of approximately 14 layers. Analogous measurements on a sample with
approximately 160 layers exhibit oscillation periods that range within the error
margin of the results measured on the first sample. Figure 4.15(a) shows an exem-
plary exponentially damped cosine fit of a TRFE trace measured on the thinner
multilayer sample (14 layers) at $B_\parallel = 9$ T. Despite the good coincidence of the
data and the fit, the accuracy may be illusive due to the large number of fitting
parameters. For worse data quality, especially when reflexes of the laser pulses
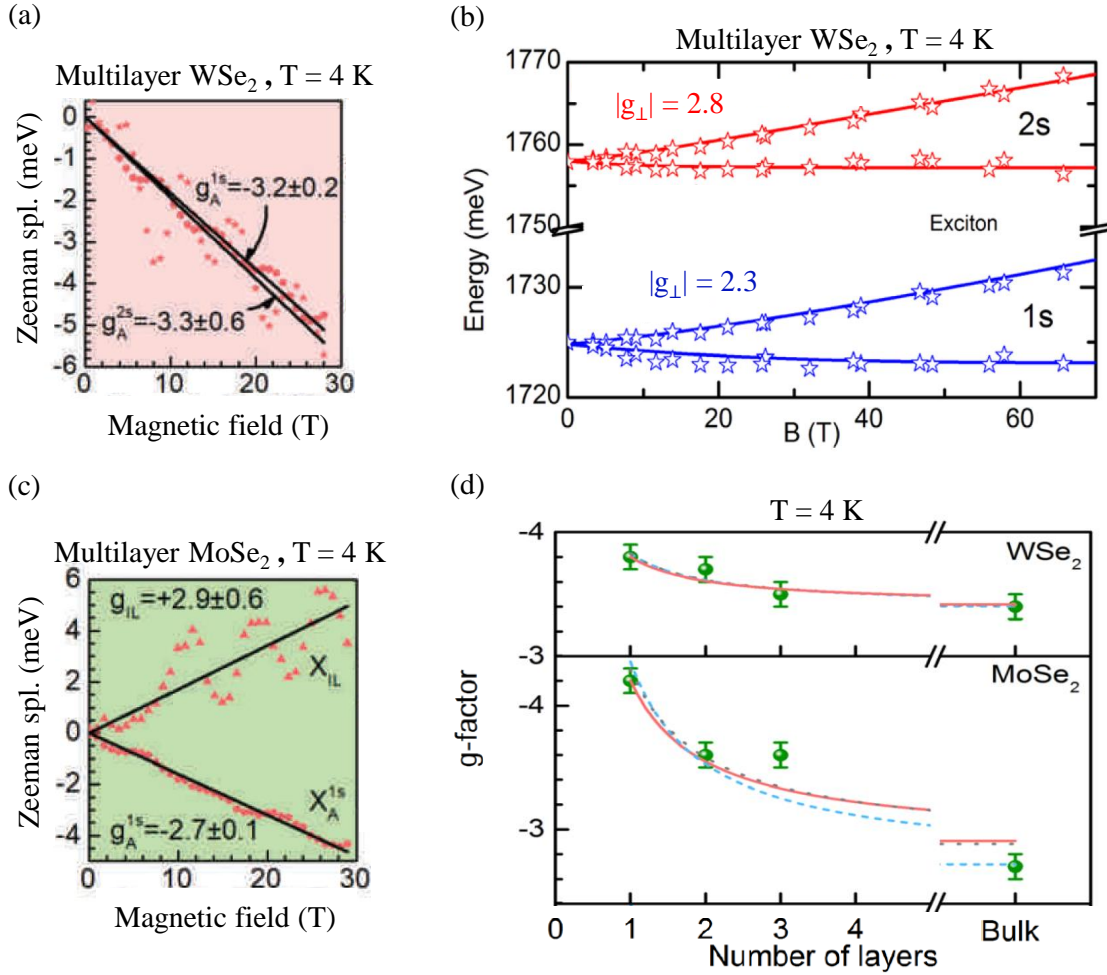
**Figure 4.14: Reoprted out-of-plane exciton g factors $g_\perp$ in bulk TMDCs.**
(a) Effective g factors for the $A_{1s}$ and $A_{2s}$ exciton obtained from reflectance measurements on a $WSe_2$ multilayer consisting of approx 45 layers. Both exciton transitions show valley Zeeman splittings of the same sign. Plot reprinted from [Aro18]. (b) Magnetic field dependence of the $A_{1s}$ and $A_{2s}$ exciton transition in bulk $WSe_2$ from transmission experiments. The solid lines are fits, modelling the diamagnetic (quadratic) shift at low magnetic fields followed by a linear Landau-like behaviour at larger field strengths. Plot adapted from [Mit15]. (c) Valley Zeeman splittings for the $A_{1s}$ exciton and the there observed interlayer exciton ($X_{IL}$) in analogy to (a). The sign of the Zeeman splitting is opposite for the two types of excitons which is the main argument for the second to be an interlayer exciton. The oscillations of the $X_{IL}$ are attributed to Faraday rotation artefacts. Graph taken from [Aro18]. (d) Layer dependence of $g_\perp$ considering the $A_{1s}$ transition in $WSe_2$ and $MoSe_2$. The lines display different theoretical models. Plot reproduced from [Aro19].

cause a second excitation as it is perceivable at $\Delta t \sim 9$ ps, an impairment of the fit accuracy occurs. Moreover, inspecting the oscillation plotted in figure 4.15(a) very carefully, a slowing-down of the oscillation can be perceived. For time delays
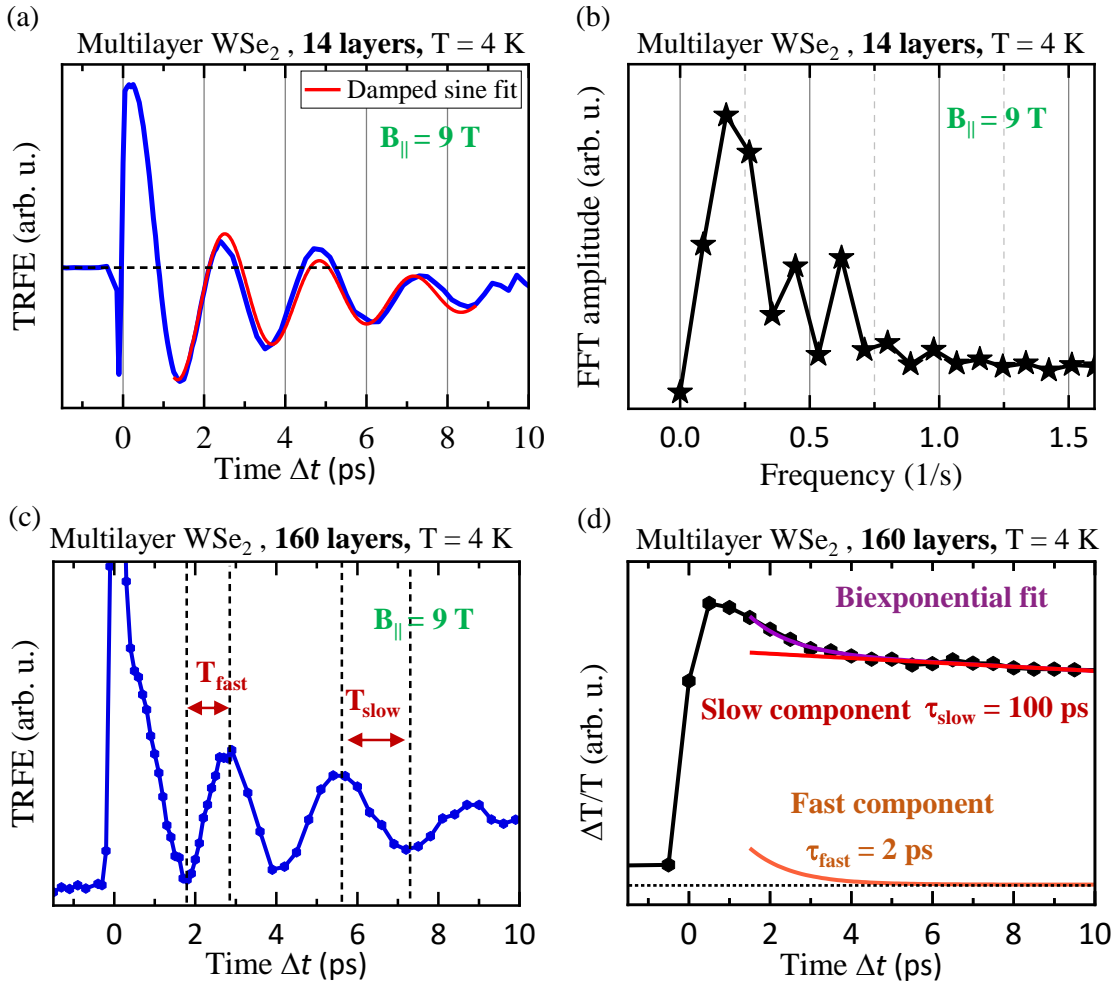
**Figure 4.15: Evaluation of the time-dependent precession frequency.**
(a) Fit by an exponentially damped cosine function. For a low-noise, the fit describes the data precisely. The accuracy diminishes considerably at an higher noise level. (b) Obtained frequency spectrum of a Fast Fourier transform analysis (with removed offset). The peak at f $\sim$ 0.2 Hz resembles the beating frequency which is also obtained by the exponential fit. The width of frequency spectrum reveals a distribution instead of a sharp peak. (c) In thicker multilayer samples, the decrease of oscillation frequency appears more pronounced. From 6 to 8 ps, the oscillation period increases by a factor of 1.5 compared to the time interval between 1 and 4 ps. (d) Transient differential transmission measurements reveal a change in the dynamics, occurring on the same time interval. A fast and a slow population decay is observable which differs by two orders of magnitude. After 4 ps, the fast decay has entirely settled. This corresponds to the moment when a decrease of the beating frequency occurs.

between 1 and 4 ps, the fit function undulates to slow while at 6 to 8 ps, the period of the fit is shorter than that of the data. For thicker multilayer samples, this effect becomes even more pronounced as plotted in figure 4.15(c). Here, one can clearly observe a change of the oscillation periods at longer time delays. In order to examine this change in frequency, a fast Fourier transform analysis has been applied to the TRFE data. The obtained frequency spectrum with removed offset is presented in figure 4.15(b). A dominant peak at f $\sim$ 0.2 Hz resembles the beating frequency. Yet the frequency distribution is rather broad, ranging from 0.2 to 0.4 Hz. Owed to low signal intensities at larger time delays that are close to the noise level, the potential appearance of a smaller peak at lower frequencies is veiled by the pronounced frequency spectrum at earlier delay times. Nonetheless, the recent investigations of our Master student Jennifer Lehner evidence a prolongation of the oscillation period at later delay times which appears to be more drastic for thicker samples consisting of more than 100 layers. This finding appears to be rather intricate as the decrease of frequency implies a time-dependent change of the g factor. A density dependence of the g factor can be excluded as our Master student Dennis Falter showed in his thesis [Fal22]. There is no significant change in the oscillation period when attenuating the excitation power by almost two orders of magnitude. Although there is no definite conclusion about the change in the period, a link to the transient differential transmission measurements can be found. The respective time trace (cf. figure 4.15.(d)) shows a fast and a slow population decay of the exciton population. After the first 4 ps, the contribution of the fast process has entirely vanished. Around this time delay, the prolongation of the undulation period occurs. In reminiscence of the exciton dynamics found time-resolved ARPES as discussed in section 4.1, it has been shown that the K-K excitons, as well as the momentum-indirect K-$\Sigma$ excitons diminish within the first 5 ps. However, the sensitivity of TR-ARPES is pushed to the limit and is most probably not able to keep track of the thermalised exciton population. The persistence of the TRFE signal for longer times evidences a valley-polarised carrier population. As the oscillations exhibit a strong resonance behaviour at the K - K exciton transition (cf. figure 4.9), it is plausible that the oscillations reflect the dynamics of carriers, residing at K. The existence of latter ones is evidenced by the clearly observable and long-lived transient differential transmission (cf. figure 4.1(d)). Potential candidates are dark excitons, exhibiting comparably long lifetimes [Rob17; Li19]. For an exciton, transferred to a spin- and/or momentum-dark state, the hole remains at K due to the large spin-splitting in the VB and thus impacts the pump-probe response of the K - K transition.

Based on this considerations, it appears plausible that the oscillation in the first

time interval (1 - 4 ps) reflects the g factor of the K - K excitons while the slightly slowed-down oscillation at later times ($\Delta t > 5$ ps) monitors the g factor of the K - $\Sigma$ excitons. In the latter case, only the g factor of the excitons' holes is detected, as the probe pulse is sensitive the K - K transition. This interpretation is corroborated by the calculations of the g factor (cf. table 2.1), revealing that the only contribution to the in-plane g factor arises from the hole spin. The difference between the computed values and our experimental observations arises presumably from excitonic hybridisation effects which are not included in the modelling. In this context it appears to be reasonable that the larger g factor of $g_{||} = 3.1$ at earlier times includes contributions from exciton hybridisation while the smaller g factor at later times is assigned to the hole component exclusively.

**Angle dependence of the pseudospin quantum beats**

After the discovery of the pseudospin quantum beats in multilayer TMDCs and the determination of the in-plane g factors, the question emerges whether the effective g factor is isotropic, i.e. $g_{||} = g_{\perp}$. For that reason, TRFE experiments with tilted magnetic field have been conducted. To be more precise, the magnetic field and the optical path are kept constant while the sample is rotated. The strength of the magnetic field is set to B = 6 T since at this field strength, the beating signatures can be observed very clearly but the alignment of the setup is considerably easier than at the maximum field of 9 T which causes a break down of the camera that is imaging the sample plane. The measurements are performed in steps of 10° for both circular polarisations starting at a pure in-plane configuration which corresponds to a tilting angle of $\Theta = 0°$. For angles larger than 45°, the split coil magnet is revolved to out-of-plane configuration (corresponding to $\Theta = 90°$). Starting from this inclination, the sample is again stepwise rotated back to 45°. Thereby, it is possible to map every magnetic field orientation from in-plane to out-of-plane. As for out-of-plane magnetic fields no oscillations on the TRFE signal can be observed, there has to be a transition from the plain decay at $\Theta = 90°$ to the oscillatory behaviour at $\Theta = 0°$. The analysis of the oscillation periods turns out to be delicate. On the one hand, the beating signature declines due to the underlying physics. On the other hand, the tilt of the sample and the substrate with respect to the optical path causes additional stray light and reflections that impair the noise level significantly. Furthermore, the time-dependent variation of the oscillation frequency, as discussed in the section before, impacts the accuracy of a damped cosine fit remarkably. Conveniently, the oscillation period has been retrieved by analysing the zero-crossings of the
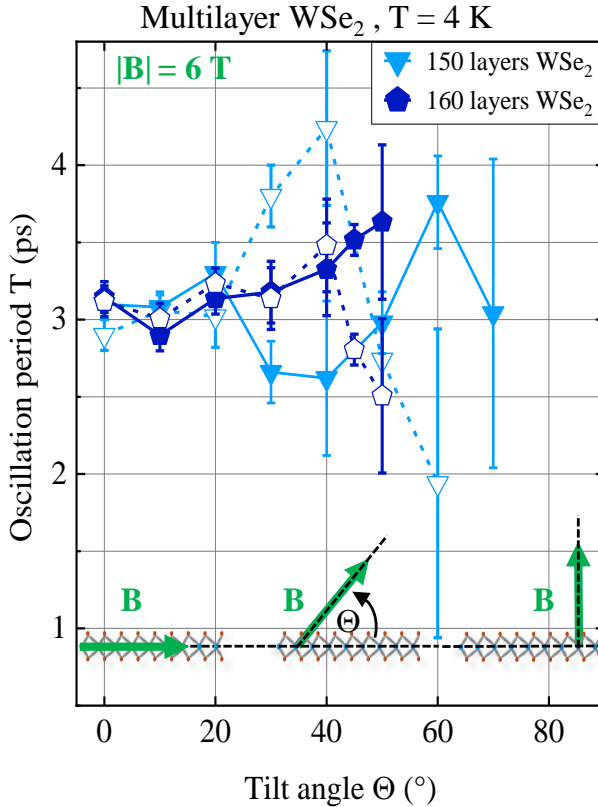
**Figure 4.16: Angle dependence of the oscillation period obtained from TRFE experiments on bulk WSe$_2$ at B = 6 T.** Two measurement series on two different samples with 150 (light blue) and 160 layers (dark blue) are presented. The solid (open) symbols denote $\sigma^+$ ($\sigma^-$) excitation. The oscillation period is retrieved by analysing the zero-crossings of the first derivative of the TRFE signals in the time interval between 2 and 4 ps and doubling the found value. The specific size of the error bars reflects the reliability of the individually determined oscillation periods. On average, no systematic change in the period can be observed.

derivative of the TRFE signals within half an oscillation cycle fixed to the time delay interval between 2 and 4 ps. The found value have been doubled in order to plot values for the full period. The thereby determined oscillation periods for $\sigma^+$ and for $\sigma^-$ excitation are plotted in figure 4.16. Beating signatures can be found up to a tilting angle of 70°. The size the error resembles the validity of the determined values. Strong deviation within the different data sets between $\sigma^+$ and $\sigma^-$ excitation are found without any systematics. On average, no remarkable impact of the specific B field orientation on the oscillation frequency and so in the g factors can be perceived. The observed behaviour follows more or less the implications of a magnetic moment precessing around the external magnetic field (cf. figure 4.12(b)). According to this model, the oscillation amplitude decreases with $A_0 \propto cos(\Theta)$ whereas the period is independent of the tilt angle. As the here found values for the in-plane g factors are very close to the reported out-of-plane g factors, the angle-dependent measurements corroborate that the effective g factor for multilayer TMDCs approaching the bulk limit is isotropic, i.e. $g_{||} \approx g_{\perp}$.

**Inter- or intralayer oscillations**

Although the origin of the pseudospin quantum beats can certainly be ascribed to excitonic transitions, it still remains elusive to figure out the specific fine structure of the excitonic transitions that are involved in the dynamics of the pseudospin quantum beats. Based on the concept of spin-layer locking [Jon14; Gon13; Raz17; Zha23] (cf. chapter 2.1.2), which states that the optical selection rules of a monolayer are preserved for the individual layers of bulk TMDC, inter-, as well as intralayer excitons are conceivable. The naturally favoured H-type stacking arrangement of TMDC multilayers implies an alternation of the valley indices (cf. figure 2.1(b)). Consequently, the K and K′ valleys of adjacent layers are located at the same value in k space. In principle, this allows for an oscillation of the exciton (as well as solely for one of its constituents) between adjacent layers with opposite valley indices without the need of momentum transfer. The magnetically-induced coupling of the opposite spin states by in-plane fields enables for the required spin flip of this intrinsically spin-forbidden transition. Thus, it is plausible that the excitons oscillate between adjacent layers, manifesting the pseudospin oscillations. A phenomenological representation of the oscillating excitons can be seen in figure 4.17(a). The larger spatial extent of excitons in multilayer TMDCs and the concomitant enhancement of hybridisation effects underpin this concept [Mer20; Erk23; Tag23]. Up to now, the exciton fine structure, meaning the occurrence of bright, grey, dark or interlayer excitons, as well as hybridisation among these states is not well understood for bulk material. Accordingly, it cannot be excluded that there is a mechanism which enables for the oscillation between the layer-inherent K valleys. Nonetheless, in this concept, it is unclear how the momentum transfer is mediated. Considering the results of the theory approach, the main contribution to the in-plane g factor in multilayer TMDCs originates from the holes (cf. table 2.1). Although in this ansatz, only the band structure, i.e. separate electrons and holes, have been considered, these finding may indicate that the hole states contribute stronger to hybridisation effects.

There are only few reports that shed light on the exciton composition in multilayer TMDCs. The theoretical considerations of Gong et al. propose a model which ascribes the oscillating motion exclusively to the holes of the excitonic complexes in bilayer TMDCs that are subjected to magnetic and electric fields [Gon13]. They predict comparably small probabilities for spin- and valley flips which corroborates the interlayer oscillation hypothesis.

Zhang et al. propose a super lattice band structure with respect to the spin characters of the bands in order to explain voltage-dependent reflectance measurements
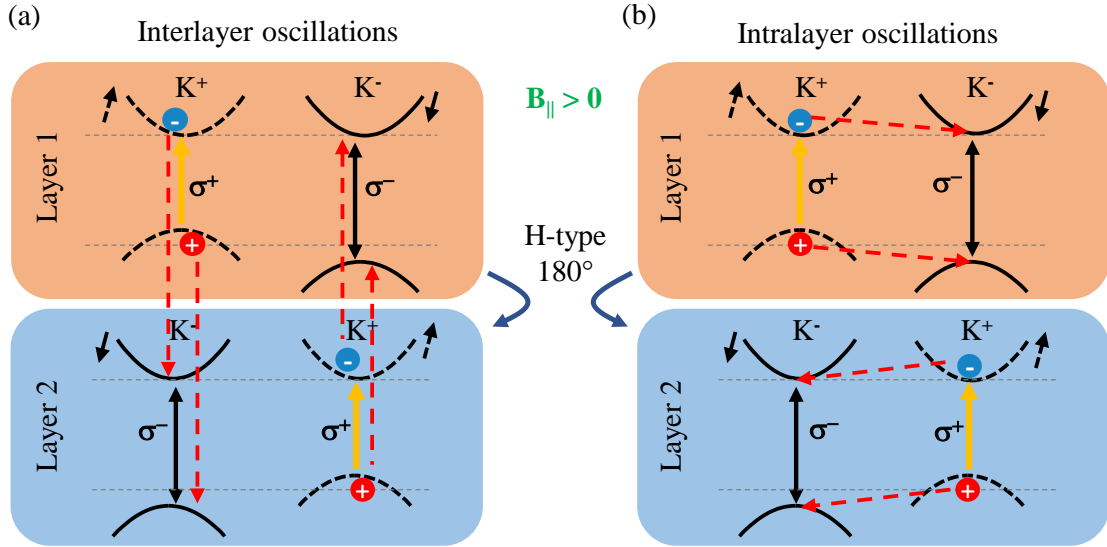
**Figure 4.17: Schematic representation of potential inter- an intralayer oscillations in an H-type bilayer TMDC.** The natural H-type stacking order in bulk TMDCs translates to a rotation by 180° in k space between the adjacent layers. For simplicity, only the bands involved in the bright transitions are depicted. Due to the non-zero in-plane g factor, a valley Zeeman splitting occurs. The dotted lines represent the energy level of the bands for B = 0 T. Spin states with opposite valley indices are coupled by the in-plane magnetic field which is indicated by the black tilted arrows. (a) Scenario of interlayer oscillations. The alternating valley structure between neighbouring layers in principle fulfils momentum conservation for excitons, hopping between the layers. (b) Alternatively, intralayer oscillations may be responsible for the change of valley index. Due to lacking knowledge on the exciton fine structure in multilayer TMDCs, this cannot be excluded. In addition, it is not clear how momentum conservation is fulfilled in this scenario.

on H-type multilayer WSe$_2$ [Zha23]. They promote the concept of dipolar excitons that form between odd or even layers. Their calculations model the hybridisation of the dipolar excitons with intralayer excitons when they are tuned towards resonance by applying perpendicular electric fields. Schematically, the proposal of dipolar excitons is displayed in figure 4.18(a). In a similar manner, Feng et al. performed voltage-dependent reflectance measurements on bi- and trilayer MoSe$_2$. They ascribe the transitions higher in energy than the neutral exciton to dipolar excitons that span over three layers [Fen22]. These findings are presented in figure 4.18(c), (d). Moreover, they determine the voltage dependent out-of-plane g factor for the dipolar exciton, revealing remarkably varying values for different voltage regimes. At charge neutrality, they measure a g factor of g$_\perp$ = -4.9 which surpasses our found value of $|g_\parallel| = 2.6$ for the A$_{2s}$ transition. Even though, a loose agreement of their RC spectrum with ours might be found (cf. figure 3.3(b)), con-
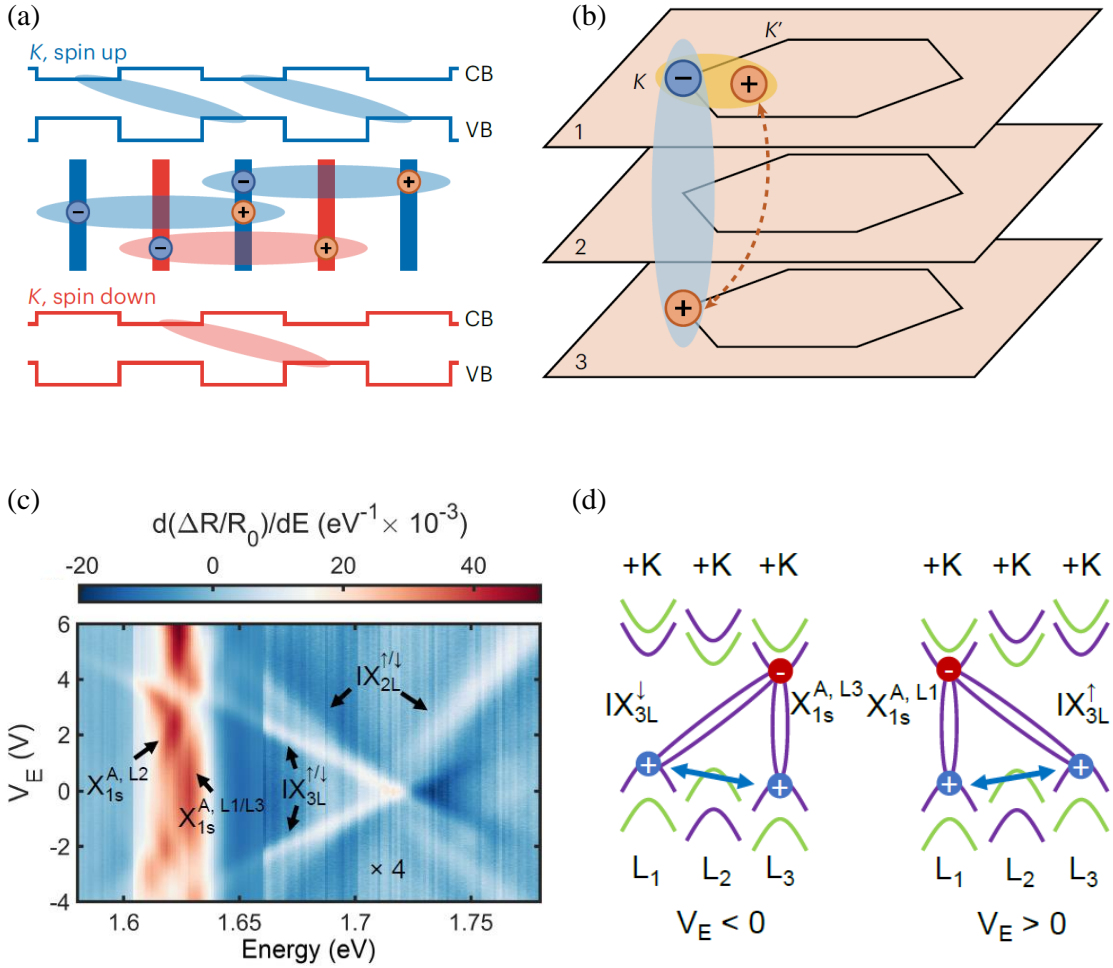
**Figure 4.18: Proposed hybridisation effects of excitons in multilayer TMDCs.** (a) A spin-valley-dependent superlattice structure concerning the spin character of the bands forms, hosting dipolar excitons (blue and red ellipses) that reside in odd or even layers. (b) Hybridisation of the dipolar excitons with bright intralayer excitons, originating from carrier hopping between layers 1 and 3. Graphs (a) and (b) are reprinted from [Zha23]. (c) Voltage-dependent reflectance spectrum of trilayer $MoSe_2$ (H-type). The features are ascribed to hybridised excitons which are schematically shown in (d) similar to the concept proposed in (a). Here, the exciton hybridisation is assigned to spin-conserving interlayer hole tunnelling between $L_1$ and $L_3$. The dipolar character allows for manipulation by applying electric fields. Figures (c) and (d) are reproduced from [Fen22].

sidering that our sample has a different intrinsic doping level and consists of much more layers, the twice as large g factor clearly indicates that the transition which we identify as the $A_{2s}$ does not correspond to the dipolar excitons proposed by Feng et al.

Slobodeniuk et al. have examined trilayer $MoS_2$ and propose likewise that electron an hole can reside in different layers [Slo19]. In analogy to the afore cited publications, they promote the idea of interlayer excitons that live either in 'odd'

or 'even' layers that may also hybridise with intralayer excitons.

Besides, there are also reports on H-type MoSe$_2$ homobilayers, suggesting hybridised interlayer excitons involving the B exciton by Feng et al. [Fen22], as well as by Sponfeldner et al. for MoS$_2$ [Spo22]. Contrarily, in the here presented work, we have not been able to observe any oscillation signature in the TRFE data of encapsulated WSe$_2$ homobilayers (not shown).

Summarising the topic of pseudospin quantum beats, we have found prominent and robust oscillation signatures of the TRFE signal for H-type multilayer TMDCs that are exposed to in-plane magnetic fields. The oscillations can be attributed to a quantum beating between the excitonic states with opposite valley index. From the beating frequency, which scales linearly with the strength of the magnetic field, the effective excitonic g factors can be deduced with a very high accuracy without the need of high-magnetic field facilities. The revelation of a non-zero in-plane g factor in bulk TMDCS constitutes a substantial discovery since monolayers themselves posses an in-plane g factor of zero which leads to the intuitive assumption to be the same for multilayers. Moreover, it is shown that the excitonic g factor is isotropic, i.e. $g_\perp = g_\parallel$. From the results of reflectance measurements along with the slightly larger g factors found for the higher-lying second oscillators, the involved excitonic transitions can undoubtedly be assigned to the A$_{1s}$ and the A$_{2s}$ exciton transition. Still, the microscopic understanding of the process that allows for a change of the valley index is not complete. Moreover, the hybridisation of exciton states plays an important role in this account. The susceptibility to magnetic and electric fields of this excitonic states may open the door for a full magneto-electrical control of the valley pseudospin. A promising step towards this vision may figure the investigation of electrically gated samples which is an ongoing project of my successor Anna Weindel and our master student Jennifer Lehner. Apart from that, our theory collaborator Paulo Faría Junior from the Fabian group with support of the group of Sivan Refaely-Abramson from the Weizmann Institute in Israel has started to model the exciton fine structure in multilayer TMDCs that goes far beyond the here applied approach. This achievement may elucidate the microscopic process and improve the precision of the modelling of exciton g factors in bulk TMDCs.

## 4.3 Time-integrated degenerate four-wave mixing

The project of four-wave mixing has been the lure that brought me to this science group as it has been the initial proposal for my master thesis in 2018. The idea of investigating excitonic quasi particles by means of non-linear optics seemed very appealing to me, since these two topics for its own are already very fascinating. From a more scientific point of view, the investigation of exciton dynamics by FWM delivers the very fundamental and unambiguous time constants $T_1$ and $T_2$, as discussed in the second chapter 2.2.2.
Owed to the complexity of the experimental technique and also the difficulty of data analysis, the here presented are challenging to interpret. The first part of this section focusses on the exploration of the FWM response of monolayer $MoSe_2$ and mono- and multilayer $WSe_2$ exposed to external magnetic fields. Furthermore, FWM experiments with different polarisation sequences have been conducted in order to investigate the coherent interaction of different exciton species, as well as the influence of multiple particle correlations.

### 4.3.1 TI-FWM on $MoSe_2$ and $WSe_2$

This section begins with the discussion of an exemplary degenerate TI-FWM measurement. Figure 4.19(a) schematically depicts the measurement technique of two-beam TI-FWM. As discussed in the method section 3.2.3, an FWM signal can be generated also with two temporally delayed pulses. Moreover, the two pulses stem from the same laser and are therefore degenerate, i.e. $\omega_1 = \omega_2 =: \omega$. For convenience, the phase matching condition $\vec{k}_{FWM} = 2\vec{k}_2 - \vec{k}_1$, implying that the FWM signal $\omega_{FWM} = 2\omega_2 - \omega_1 = \omega$ possesses the same frequency as the exciting laser, has been selected. In figure 4.19(b), the TI-FWM signal of monolayer $MoSe_2$ is plotted. Apparently, the duration of the FWM signal is in the same order of magnitude as the instrument function which is given by the cross-correlation of both pulses. The analysis of the data is accomplished by fitting a convolution of a Gaussian pulse with an exponential decay function to it. Therefore, the signal is distinguishable from the instrument response and a reliable decay time $\tau$ can be extracted. The assumption of an inhomogeneously broadened exciton population is valid since the large laser spot (50 μm diameter) covers areas of varying sample quality. Accordingly, the exponential's decay constant $\tau$ is multiplied by a factor of 4 which yields the according coherence time $T_2$, as elaborated in chapter 3.2.3. First, the carrier density dependence on the coherence time $T_2$ is examined. Therefore, the power of both beams is stepwise reduced over more than one order of
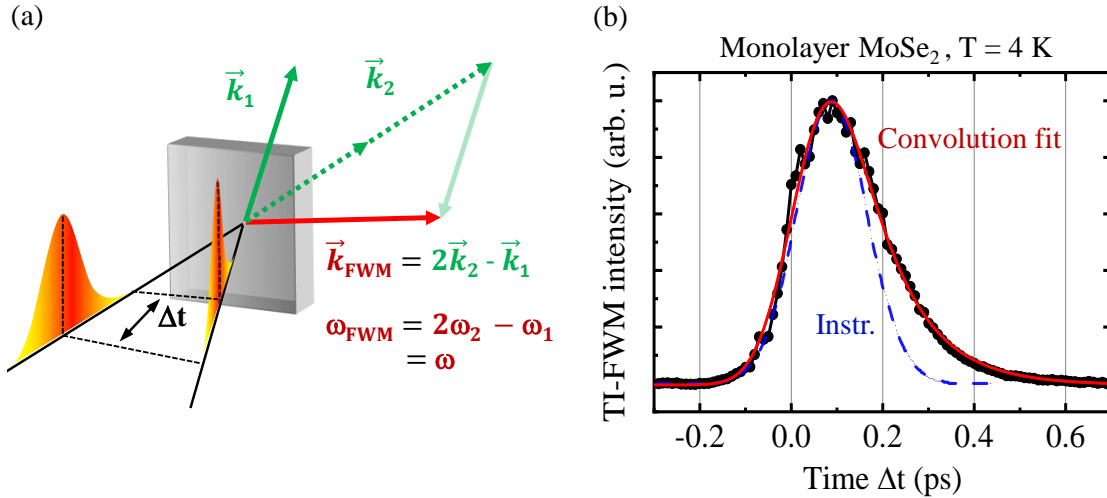
**Figure 4.19: Time-integrated degenerate two-beam FWM.** (a) Reduced schematic representation of the here applied FWM technique. Pulse 1 and 2 stem from the same laser. The signal, fulfilling the phase matching condition $\vec{k}_{FWM} = 2\vec{k}_2 - \vec{k}_1$ and thus exhibiting the same frequency $\omega$ as the driving pulses, is acquired by an avalanche photo diode. (b) Representative FWM signal measured on monolayer $MoSe_2$. The dashed blue line gives the instrument function while the solid red line represents a convolution fit.

magnitude. For every measurement, absorption measurements of the beams have been conducted in order to determine the on-site value of the absorbed power as explained in chapter 3.2.1. The FWM data sets for monolayer $MoSe_2$ and $WSe_2$ for different excitation densities are presented in figure 4.20. The respective excitation density and the according $T_2$ time can be discerned from the insets. For monolayer $MoSe_2$, the found $T_2$ times range between 400 fs and 800 fs for population densities of n $= 10^{12} - 10^{11}$ cm$^{-2}$. For single-layer $WSe_2$, a particularly stronger density dependence is discovered. Here, the $T_2$ times span from 60 to 650 fs for densities from n $= 7 \cdot 10^{11}$ cm$^{-2}$ down to $5 \cdot 10^{10}$ cm$^{-2}$. In literature, the $T_2$ time is often presented as a linewidth $\gamma = 2\hbar/T_2$, resembling a linear power dependence [Bol85]. Accordingly, our results are plotted in figure 4.21(a) and (c) for monolayer $MoSe_2$ and $WSe_2$, respectively. Figures (b) and (d) show comparable results from literature. Our findings for monolayer $MoSe_2$ are in very good agreement with the findings of Boule et al. (cf. figure 4.21(b)) who performed TR-FWM [Bou20], whereas our results for $WSe_2$ only partially coincide with the report of Moody et al. (cf. figure 4.21(d)) who performed 2D spectroscopy experiments [Moo15]. While the the results of monolayer $WSe_2$ are in good accordance at low excitation densities, a remarkably discrepancy appears for higher densities. A reason for the deviations at higher densities may emanate from the method to determine the amount of the exciton densities. Moody et al. specify the exciton
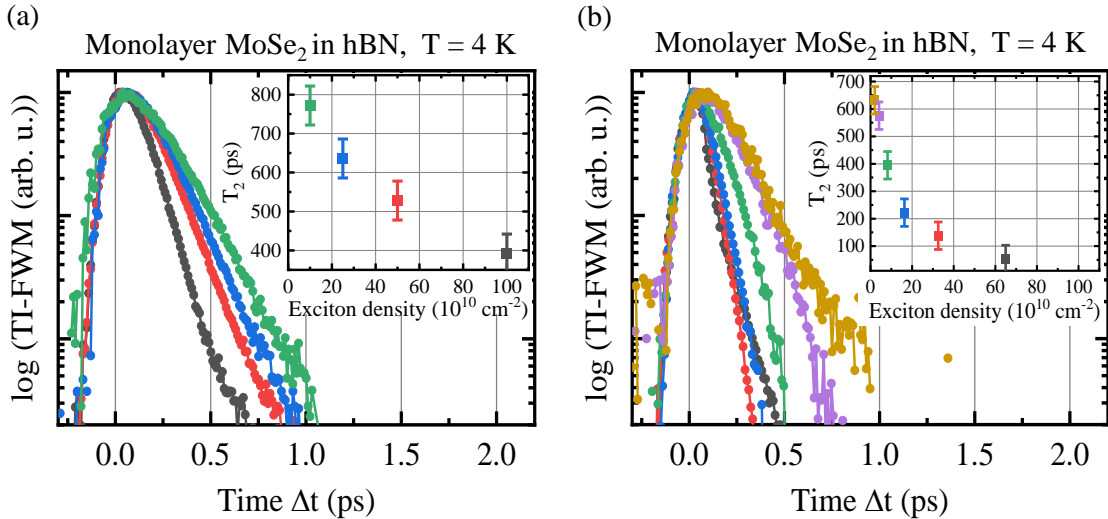
**Figure 4.20: Density dependence of the FWM signal for monolayer MoSe$_2$ and WSe$_2$.** The decay time of the FWM signal shortens at elevated exciton densities. In the insets, the extracted T$_2$ times are denoted. The colour-coding of the insets indicates the exciton densities for the respective FWM traces. (a) For MoSe$_2$, a doubling of T$_2$ occurs by reducing the carrier density by one order of magnitude. (b) For WSe$_2$, the density dependence of T$_2$ is more significant, changing by a factor of 5 within one order of magnitude of attenuation.

density by a fixed absorption coefficient of 12% (cf. supplementary of [Moo15], Note 2). In the here presented work, absorption measurements evidence a strongly quenched absorption of about 1% of the total incident power at elevated exciton densities. Consequently, the densities given in Moody et al. might be overestimated. Including this aspect, our results are in reasonable agreement. In general, the density-dependent linewidth broadening, i.e. the reduction of T$_2$, is assigned to exciton-induced decoherence [Hon89; Wan93; Moo15; Jak19; Bou20]. The enhanced exciton-exciton interaction, which is about one order of magnitude larger than in conventional semiconductor systems [Wag97], can be traced back to a reduced dielectric screening [Kel79]. Figuratively speaking, the reduced dielectric screening makes the excitons feel the Coulomb interaction among each other much stronger. However, the question remains why the TI-FWM signal of monolayer WSe$_2$ is much more susceptible to a variation of density than single-layer MoSe$_2$. Intuitively, the situation would be expected to be reversed since the lowest exciton state in WSe$_2$ is dark and could serve as an efficient buffer reservoir.

In summary, our findings of the density dependence on the coherence time T$_2$ accurately resemble a linear increase of the corresponding homogeneous linewidth and do well connect to other publications on this issue.
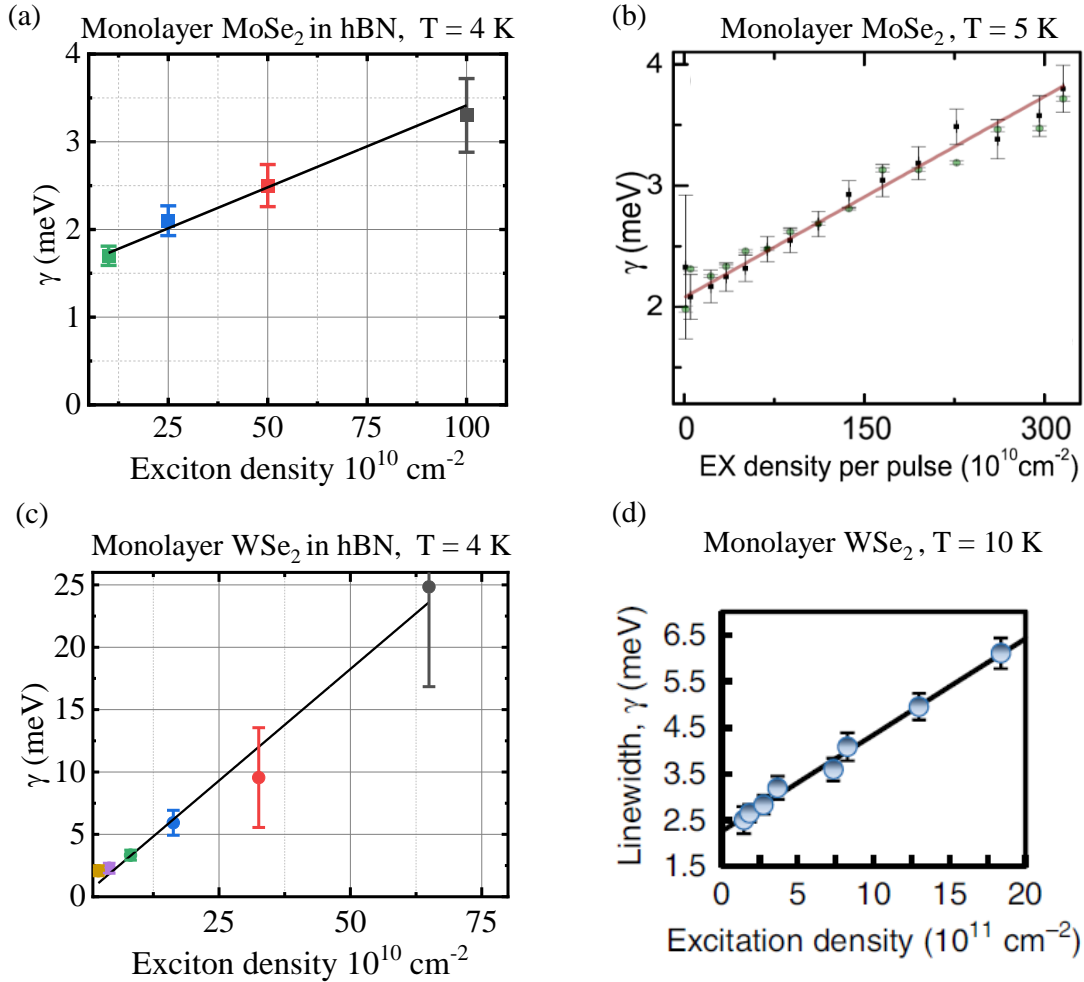
**Figure 4.21: Comparison of the retrieved homogenous linewidths $\gamma$ with literature.** As the $T_2$ time directly determines the homogenous linewidth by $\gamma = 2\hbar/T_2$, it can be also plotted as a function of exciton density, revealing a linear behaviour. (a) The extracted values for monolayer $MoSe_2$ from this work are in good accordance with the findings of Boule et al., shown in (b) [Bou20]. (c) A more pronounced density dependence of the linewidth is found for monolayer $WSe_2$ which has also been reported by Moody et al. whose results are reproduced in figure (d) [Moo15]. However, this increase is 20 times stronger compared to $MoSe_2$ while the results of (b) and (d) differ by only a factor of 5.

## 4.3.2 TI-FWM in magnetic fields

In these investigation it is aimed to study the influence of out-of-plane magnetic fields on the coherence time $T_2$. As already discussed, out-of-plane magnetic fields break the valley degeneracy, inducing a valley Zeeman splitting. Considering the dynamics monitored by FWM in a microscopic picture, it has been shown that the two-particle correlations (excitons) contribute to the FWM signal for positive delay times whereas four-particle correlation (biexcitons) effects give rise to FWM
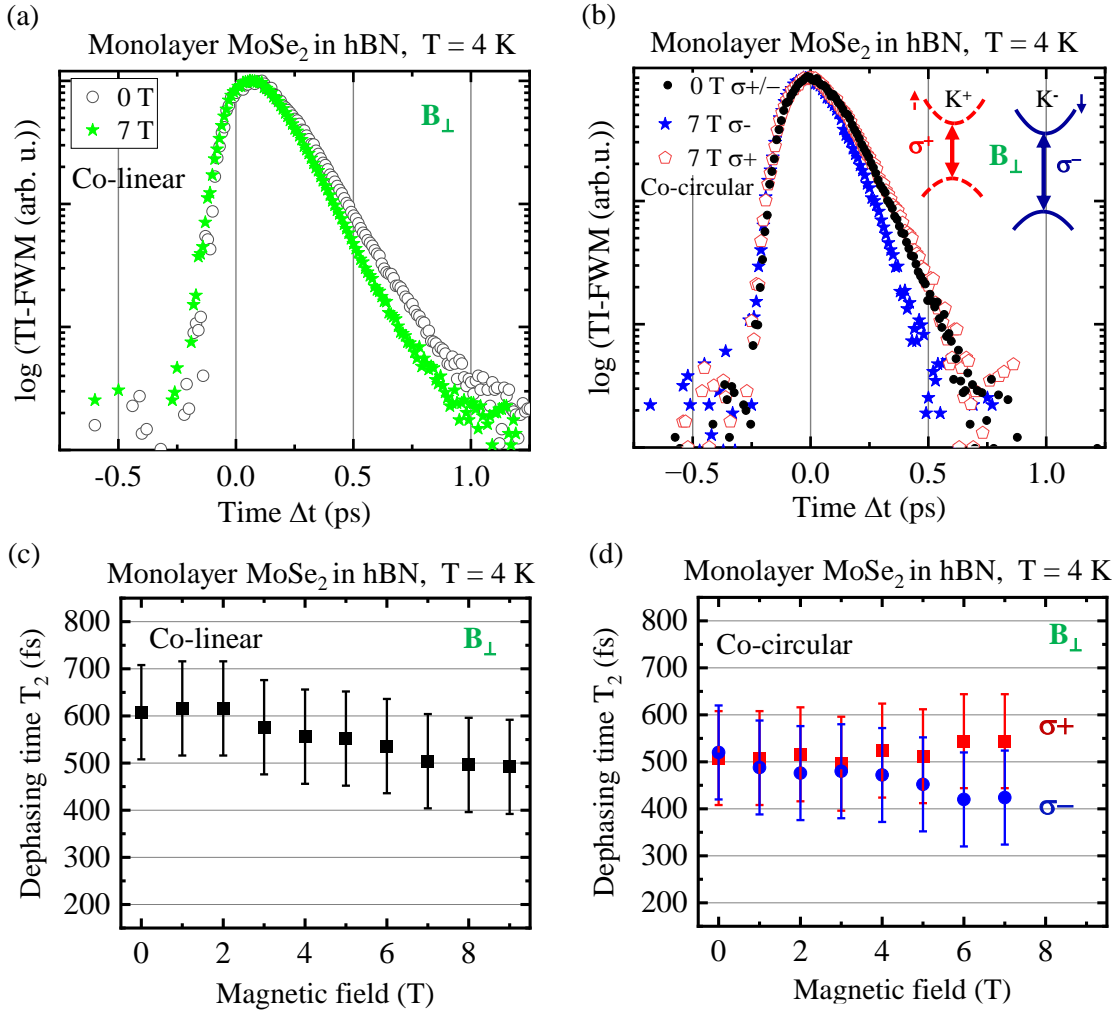
91

(a)

Monolayer MoSe$_2$ in hBN,  T = 4 K

(b)

Monolayer MoSe$_2$ in hBN,  T = 4 K

(c)

Monolayer MoSe$_2$ in hBN,  T = 4 K

(d)

Monolayer MoSe$_2$ in hBN,  T = 4 K



**Figure 4.22: TI-FWM measurement on monolayer MoSe$_2$ exposed to out-of-plane magnetic fields.** In general, coherence turns out to be longer for co-linear polarisation than for co-circular. The magnetic field causes a shortening of coherence for linear polarisation. The inset on the right shows the effect of valley Zeeman splitting. Here, the energy separation in the K$^-$ valley is less favourable, causing a faster loss of coherence compared to the K$^+$ valley. The according values for T$_2$ for the respective polarisations are plotted in (c) and (d). For co-linear polarisation, T$_2$ is on average 100 fs longer than for co-circular excitation. Moreover, for co-circular polarisation a decrease of the $\sigma^-$ polarised exciton coherence can be observed while for $\sigma^+$ polarisation, the values for T$_2$ remain basically constant.

signals at negative time delays [Feu91; Wan94; Mai94; Kne98; Che01; Hao17]. Strong magnetic fields have been found to impact the non-linear response of excitonic and biexcitonic transitions in TMDCs [Ste18b; Map22].

In all measurements that are presented in the following, the exciton has been resonant to the A$_{1s}$ exciton transition. The maximum power of the beam is attenuated by a factor of 4, giving rise to an exciton density of n = 2 $\cdot$ 10$^{11}$ cm$^{-2}$

because at lower excitation, the FWM signal is more long-lived but weaker in intensity as showed in the section before. For each magnetic field step, FWM traces for co-linear and co-circular polarisations are acquired. More elaborate, this implies that the first and the second pulse have the same polarisation as well as the detection scheme is exclusively sensitive to the according polarisation component of the FWM signal. FWM data sets up to 9 T in steps of one Tesla have been measured for linear, $\sigma^+$ and $\sigma^-$ polarisation sequences.

For monolayer $MoSe_2$, the dependency of out-of-plane magnetic fields on the FWM response for different polarisation sequences is investigated. Representative measurements for B = 0 T and B = 7 T are depicted in figure 4.22 (a) and (b). In co-linear configuration, a slight shortening of $T_2$ can be found at higher magnetic fields (cf. figure 4.22(c)). Interestingly, the coherence time in co-circular polarisation is approximately 100 ps shorter than for co-linear polarisation (cf. figure 4.22(d)). This difference is caused by a stronger bleaching effect for circular excitation compared to linear excitation since in the latter case, half of the absorbed power creates excitons in the opposite valley [Ste18b]. With increasing field strength, a difference in $T_2$ for the distinct circular polarisations can be perceived (cf. figure 4.22(b) and (d)). While the coherence for $\sigma^+$ polarisation slightly increase, the $\sigma^-$ polarisation clearly decrease. From the direction of the magnetic field, it can be inferred that the exciton energy in $K^+$ diminishes while it is raised in $K^-$. The faster loss of exciton coherence in $K^-$ can be explained with a transfer of bright excitons to $K^+$. Vice versa, the transfer is blocked as the valley Zeeman splitting imposes an energy barrier.

At zero magnetic fields, our results are in perfect coincidence with the findings of Jakubczyk et al. who also find a coherence time of $T_2$ = 600 fs for low exciton densities [Jak16]. Scarpelli et al. report similar values at a temperature of 77 K [Sca17]. Steven et al. have performed three-beam TI-FWM on monolayer $MoSe_2$ in magnetic fields up to 25 T (out-of-plane) which are supported by time-dependent DFT calculations [Ste18b]. Their main results are presented in figure 4.23. In their work, they present measurements with a co-linear polarisation sequence. Complementary, experiments with a cross-circular pulse sequence of $(\sigma^+\sigma^-\sigma^+\sigma^-)$ for pulse 1, 2, 3 and the detection have been performed. The latter sequence favours the formation and detection of biexcitons since the most favourable biexciton state virtually consists of two bound excitons, residing in $K^+$ and $K^-$ whereas in a co-linear alignment, mostly neutral excitons are regarded [Hao17]. The direct excitation of biexcitons which are located 20 meV below the neutral exciton is possible due to the broad-band excitation. Note that in our experimental setup, it is not possible to apply a cross-circularly polarised sequence
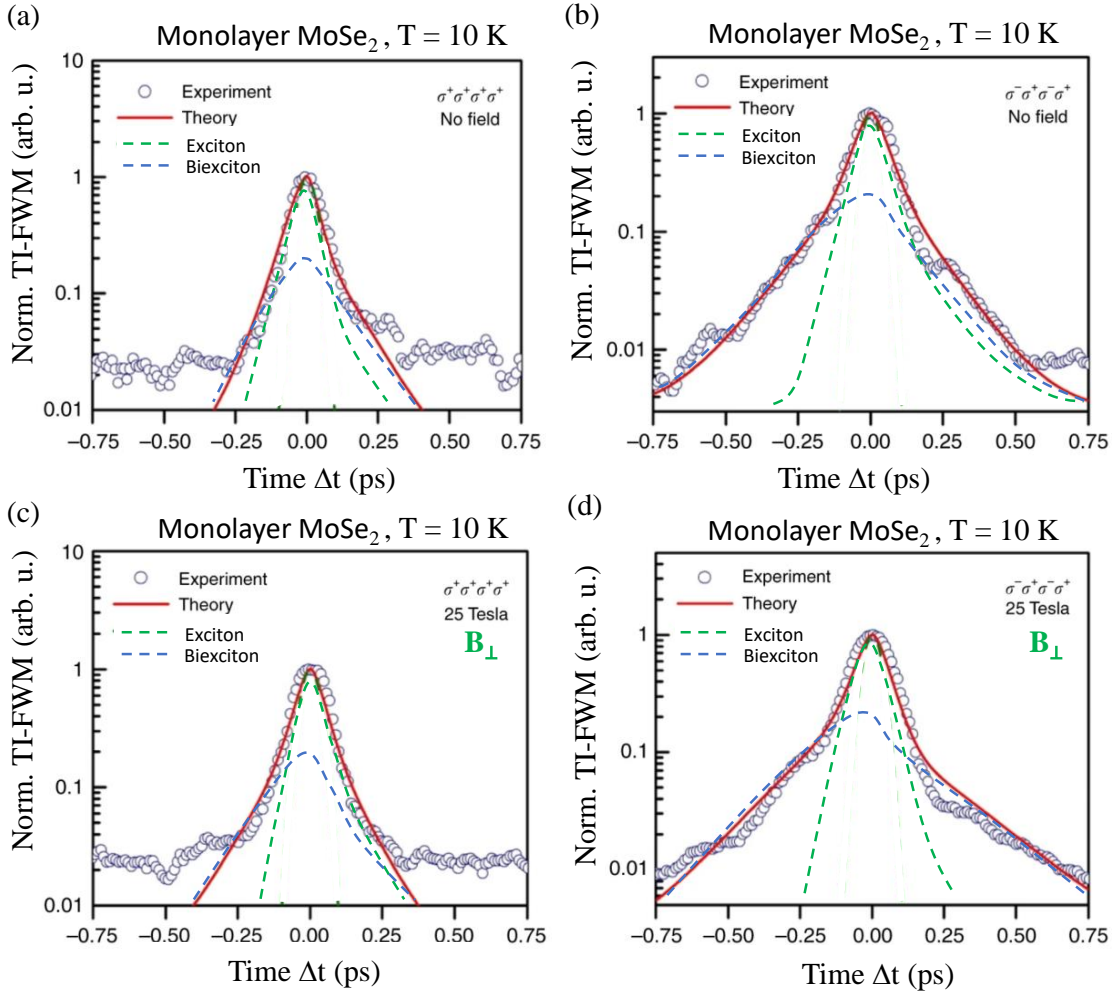
**Figure 4.23:** **Polarisation-resolved magneto TI-FWM on monolayer MoSe₂ by Steven et al.** The polarisation sequence given at the top right of every graph denotes the polarisation of the first, second and third pulse and of the detection. Time-dependent DFT calculation model the data (red solid line) consisting excitonic (green dashed line) and biexcitonic contributions (blue dashed line). (a) Co-linear TI-FWM for B = 0 T. (b) Cross-circular polarisation sequence which is susceptible to biexcitonic contributions for B = 0 T. (c) Co-linear polarisation at B = 25 T. No significant influence of the magnetic fields can be observed in the data nor in the model. (d) Cross-circular polarisation at B = 25 T. The model predicts a reduction of the excitonic component and an enhancement of the biexcitonic contribution at later delay times. Graphs modified from [Ste18b].

because it is based on a two-beam technique which implies that pulse 2 and 3 are identical and thus intrinsically possess the same polarisation. In addition, the split coil magnet is limited to magnetic fields of 10 T. Thus our findings can only partially be compared with the ones of of Stevens et al. [Ste18b]. Nevertheless, the co-linear polarised experiments can be compared at least for B = 0 T since the co-linear polarisation sequence translates to a superposition of $(\sigma^+\sigma^-\sigma^+\sigma^-)$

and $(\sigma^-\sigma^+\sigma^-\sigma^+)$. In total, our results match in most of the points. Likewise, a broader FWM signal for linear excitation than for co-circular excitation can be noticed. For a cross-circular polarisation sequence, their data exhibits a steeper flank of the FWM trace at B = 25 T compared to B = 0 T which can be clearly seen when comparing figures 4.23(b) and (d). The modelling in these figures indicates a narrowing of the excitonic contribution at high magnetic fields while the biexcitonic components, which cause the weak signal at very early and very late times, is expected to broaden in time. The change of the presented data between figure 4.23(b) and (d) is very tiny. Yet, the best perceivable features are a small signal increase at negative times, as well as the steepening of the right flank near the peak. In both accounts, our findings point towards the same direction (cf. figure 4.22(a)). Unfortunately, Stevens et al. do not show nor write anything regarding measurements with $\sigma^-$ co-circular polarisation (not even in the supplementary information).

Concluding the discussion concerning $MoSe_2$, we observe a decrease of coherence at high magnetic field which is dependent on the polarisation and can be explained by the valley Zeeman splitting. However, our results do not reveal any contributions at negative time delays and hence no fingerprints of magnetically coupled biexcitons.

On monolayer $WSe_2$, FWM experiments with co-circular polarisation have been performed applying in- and out-of-plane magnetic fields which are presented in figure 4.24. The comparably fast decay dynamics with respect to the time resolution of the setup as well as the weak susceptibility to magnetic fields allows only for a rather rudimental interpretation. For out-of-plane magnetic fields, no significant change in the FWM signal can be observed (cf. figure 4.24(a)). The corresponding $T_2$ times from fitted FWM data sets are shown in the inset for both co-circular polarisation sequences. No systematic change is visible for any of the polarisations. The here extracted coherence time $T_2 \approx 200$ fs for an intermediate exciton density of $n = 2 \cdot 10^{11}$ cm$^{-2}$ is in good agreement with the results of Moody et al. ($T_2 = 290$ fs at $n = 1.4 \cdot 10^{11}$ cm$^{-2}$ and T = 10 K) [Moo15], as well as with Dey et al. ($T_2 = 280$ fs at T = 5 K) [Dey16] and Mapara et al. ($T_2 = 250$ fs at T = 10 K) [Map22].

For in-plane magnetic fields, a slight increase of the FWM signal at positive time delays can be found as it is shown in figure 4.24(b). External in-plane magnetic fields give rise to a coupling of the spin character of the bands which leads to a brightening of the dark exciton by its hybridisation with the bright exciton [Ech16; Zha17; Mol17]. The increase of the FWM signal at positive time delays can hence be assigned to contributions of dark excitons. Given that this coupling
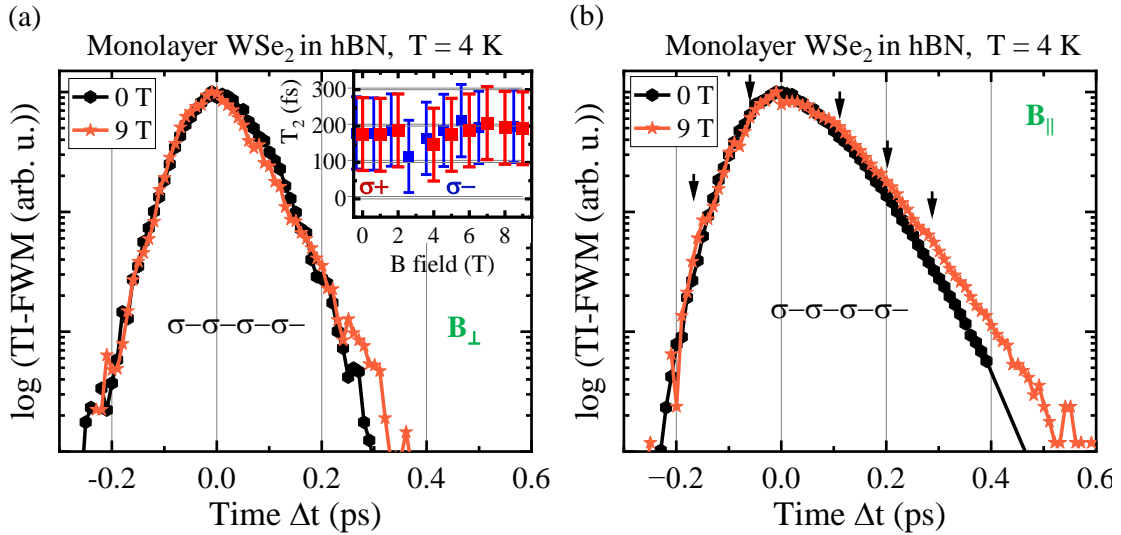
**Figure 4.24: Co-circularly polarised TI-FWM measurements at B = 0 and B = 9 exposed to magnetic fields.** (a) The FWM traces are largely immune under the influence of out-of-plane fields. The inset shows the extracted $T_2$ times from $\sigma^+$ (red) and $\sigma^-$ (blue) co-circularly polarised measurements in steps of one Tesla. (b) For in-plane fields, the signal is slightly enhanced at positive delay times comparing 0 and 9 T. The signal for $B_{||} = 9$ T carries a barely visible fingerprint of an oscillation with a period of $T_{beat} \approx 100$ fs (indicated by the black arrows) which can be ascribed to a magnetic-field induced coupling of the bright and dark exciton state.

is a coherent process, it is expected to manifest as a quantum beating. Taking an energy splitting of approximately 40 meV into account [Zha17; Mol17], the resulting beating period denotes $T_{beat} \approx 100$ fs. With this information in mind, we find a very shallow oscillation on the FWM trace of for $B_{||} = 9$ T (cf. figure 4.24(b)). Nonetheless, this signature does not appear pronounced enough for a more detailed analysis.

Mapara et al. report the emergence of a beating on their TI-FWM signal of monolayer WSe$_2$ for co-circular excitation and in-plane magnetic fields up to 25 T [Map22]. For comparison, their main results are presented in figure 4.25. Contrarily, our measurements do not reveal an enhancement of the signal at negative time delays (cf. figure 4.25(a) and (b)). A reason for the poor occurrence of the beating signature might be the lower field of 9 T instead of 15 T. According to the modelling of Mapara et al., a linear shift of the bright and dark exciton towards each other is assumed which allows for the hybridisation of both states. Hybridisation is estimated to be strongest at B = 15 T [Map22]. Following this interpretation, the emergence of a beating signature should also be clearly observably at a field strength of B = 9 T. Furthermore, the accuracy of our presented data is much higher, spanning over more than three orders of magnitude than
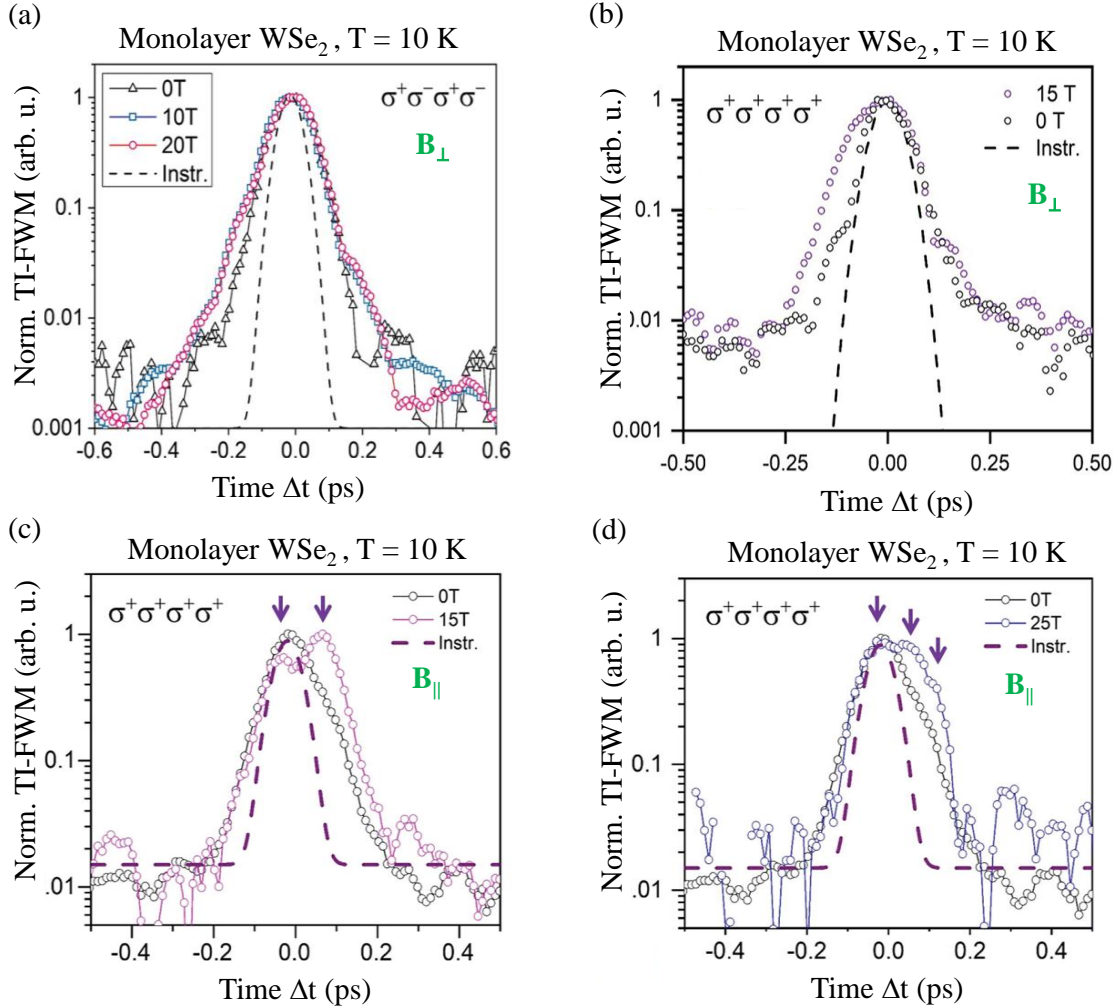
**Figure 4.25: Polarisation-resolved TI-FWM on monolayer WSe$_2$ exposed to in- and out-of-plane magnetic fields by Mapara et al.** The polarisation sequence given at the top right of every graph denotes the polarisation of the first, second, third pulse and of the detection while the dashed line denotes the time resolution limit. (a) For a cross-circular polarisation sequence, which is explicitly sensitive to biexcitonic contributions, the FWM signal reveals no dependence on the out-of-plane magnetic field. (b) In co-circular polarisation, a signal increase at negative times appears at elevated magnetic fields, which is ascribed to the hybridisation of the bright and dark exciton, reaching its maximum coupling strength at B = 15 T. (c), (d) For co-linear polarisation with applied in-plane magnetic field, a beating signature emerges which is assigned to a coherent coupling between bright and spin-dark exciton states in the same valley. As the hybridisation exhibits a resonance behaviour which is maximal at B = 15 T, the beating amplitude decreases again at higher magnetic fields as shown in (d). Graphs reprinted from [Map22].

the one of Mapara et al. Nevertheless, the evidence of a quantum beating in our measurements is debatable. Apart from that, we do not notice an impact of the magnetic field for a linear polarisation configuration which is in line with the re-
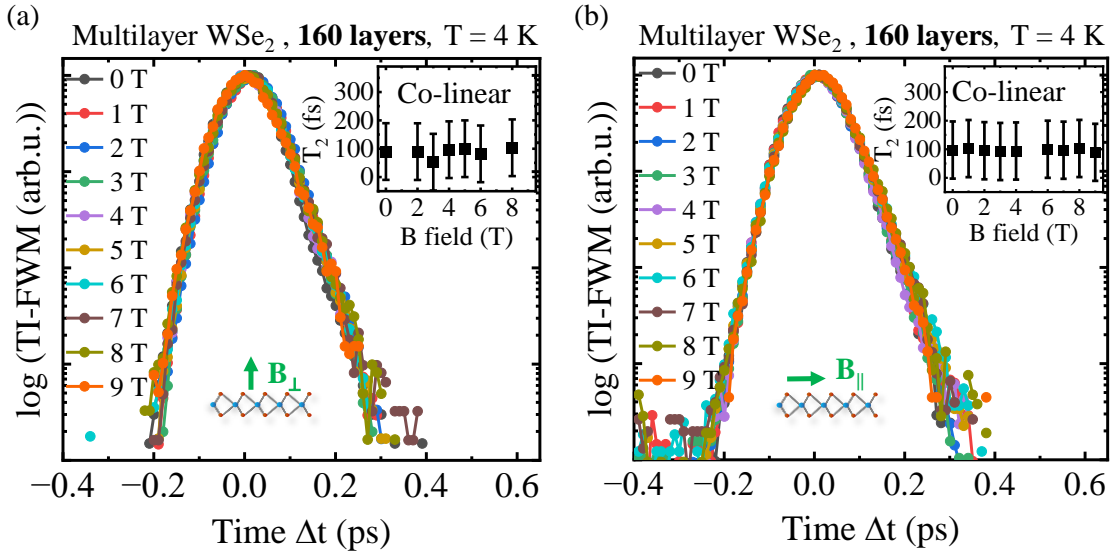
**Figure 4.26: TI-FWM on multilayer WSe$_2$ exposed to magnetic fields.**
The co-linear excitation in principally allows for the formation of all excitonic complexes. Insets indicate the retrieved coherence times for the respective magnetic field strengths. (a) The valley Zeeman shift which occurs in out-of-plane configuration does not remarkably affect the FWM signals. (b) For in-plane fields, the valleys are shifted and in addition a coupling of different spin states emerges. Nonetheless, no influence of the magnetic field is observable.

sults for cross-circular polarisation by the afore cited publication. Overall, we see only few impact of the magnetic field on the FWM signal of monolayer WSe$_2$. In principle, an exciton-trion beating for in-plane fields can be attested, although its appearance it very faint.

Sparked by the coupling effects triggered by in-plane magnetic fields in TMDCs, FWM experiments on multilayer samples exposed to magnetic fields seemed to be very exciting. Unfortunately, the FWM signal of bulk WSe$_2$ ($\sim$ 160 layers) turns out to decay very rapidly with an according coherence time of T$_2$ = 100 $\pm$ 100 fs. Despite of the expectations, the FWM signal remains unaffected by in- and out-of-plane magnetic field. According data sets from 0 to 9 T in co-linear polarisation configuration, which in principle comprises all possible polarisation sequences, are depicted in figure 4.26. A possible explanation for the comparably short coherence times may be the doubled excitation power, applied in our experiment, compared to the investigations on monolayers. The increase of power has been decided in order to obtain a carrier density distribution within the individual layers that is centred around the value n = 2 $\cdot 10^{11}$ cm$^{-2}$ in analogy to the densities that have been excited in the monolayer samples. Assuming linear absorption, the intensity of the light within a medium drops exponentially according to the law of Beer-Lambert. The studied WSe$_2$ sample consists of $\sim$ 160 layers. Therefore, the

carrier density ranges from n = 3.5 $\cdot 10^{11}$ cm$^{-2}$ in the first layer down to n = 1 $\cdot 10^{11}$ cm$^{-2}$ in the last layer of the sample which in monolayer WSe$_2$ corresponds to coherence times of T$_2$ = 100 - 400 fs (cf. figure 4.20). As the intensity of the FWM signal scales to the power of three of the electric field, the detected data set resembles particularly the response of the most strongest excited layers.

The shortening of the coherence time, as the value for its own are controversial to the work of Dey et al. who report a prolongation from 280 fs (monolayer) to 420 fs (bulk) [Dey16]. They assign the increase of coherence to the pristine confinement of the individual layers inside of the bulk crystal. Unfortunately, the thickness of the bulk sample is not mentioned in [Dey16], nor in the supplementary information. Besides, Helmrich et al. measure in their TR-FWM a coherence times of T$_2$ = 50 fs for bilayer MoSe$_2$which is six times smaller than their determined coherence time for monolayer MoSe$_2$ [Hel21]. In the publication, they ascribe the ultrafast decay of coherence to the (incoherent) transfer of the exciton's electron to the $\Sigma$ valley which is corroborated by time-dependent theoretical modelling. They emphasis that the much faster dynamics compared to for instance TR-ARPES as discussed in section 4.1, stem inherently from the FWM method, which exclusively captures the coherent regime whereas generic pump-probe techniques generally acquire also incoherent contributions. Although in our experiment, multilayer WSe$_2$ instead of bilayer MoSe$_2$ is considered, this argument should be equally valid since the $\Sigma$ - K exciton transition is also lower in energy than the K - K transition.

Concluding the discussion about FWM on multilayer WSe$_2$, our results are not contradicting to literature albeit the very short-lived FWM signal barely permits the observation of multiple particle interaction or coherent coupling. Besides, most of these regarded processes presumably take place on longer time scales.

### 4.3.3 Beating signatures found by TI-FWM

Apart from the examinations on the influence of magnetic fields, FWM experiments with different excitation energies and diverse polarisation sequences have been conducted. The spectral width of the applied laser pulses enables for a simultaneous coherent excitation of multiple excitonic complexes. Regarding monolayer MoSe$_2$, the trion and biexciton figure possible bright states that in principle may interact coherently with the neutral A exciton. TI-FWM measurements with resonant excitation on the A$_{1s}$ exciton transition are presented in figure 4.27. For co-circular ($\sigma^+\sigma^+\sigma^+\sigma^+$) and co-linear ($\rightarrow\rightarrow\rightarrow\rightarrow$) polarisation, no relevant difference between the FWM traces can be observed. Even the polarisation rotation of
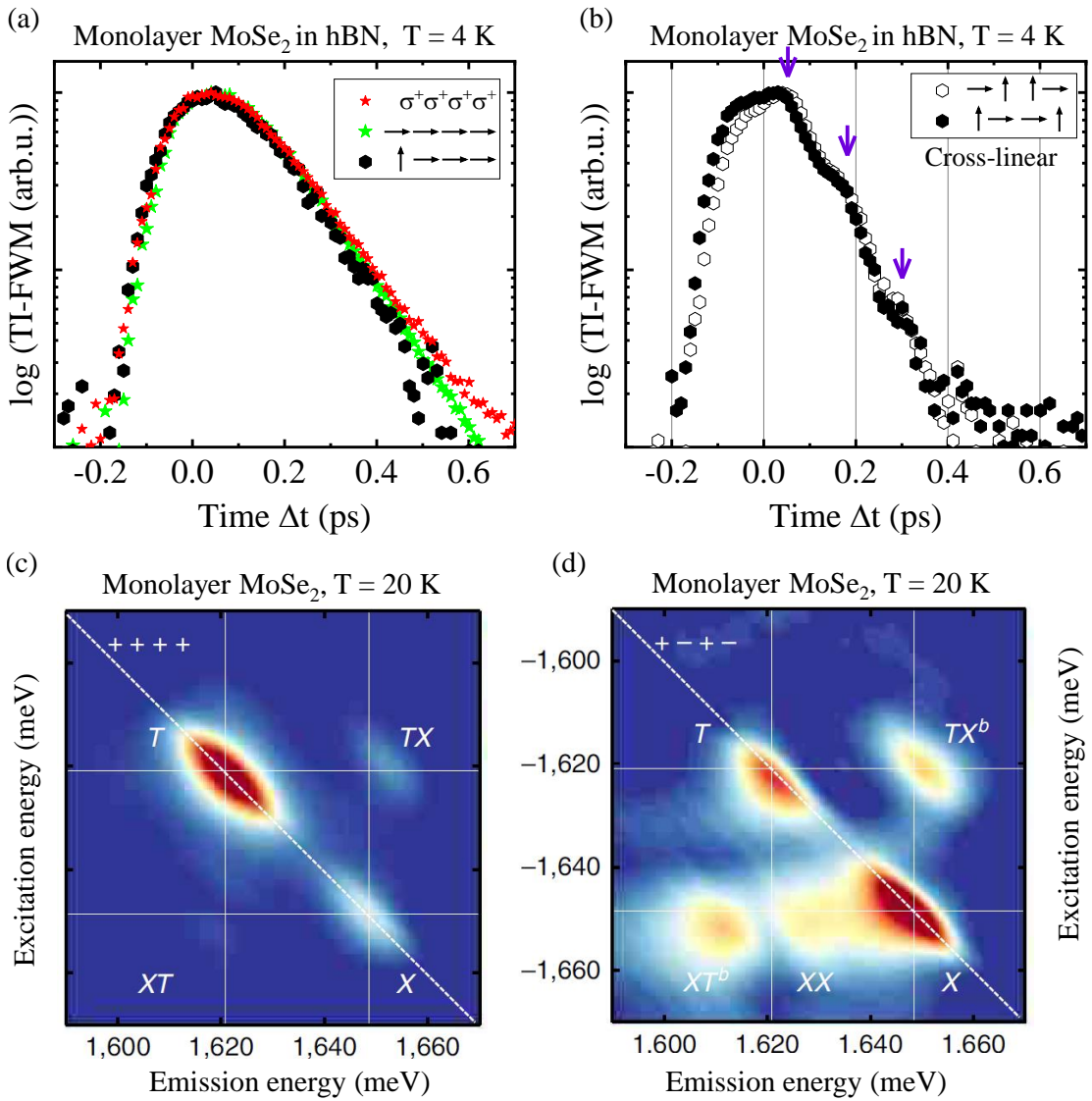
**Figure 4.27: Exciton-trion quantum beats in monolayer WSe₂ revealed by TI-FWM complemented by seminal references.** In the legend, the first three items denote the polarisation of pulse 1, 2 and 3 while the fourth item represents the polarisation component to which the detection is sensitive to. Linear polarisation is indicated by horizontal or vertical arrows. (a) TI-FWM measurements on monolayer MoSe₂. For co-circular ($\sigma^+\sigma^+\sigma^+\sigma^+$) and co-linear ($\rightarrow\rightarrow\rightarrow\rightarrow$) polarisation and also for a partially crossed sequence ($\uparrow\rightarrow\rightarrow\rightarrow$), no remarkable difference in the FWM traces occurs. (b) In stark contrast, a clear modulation of the FWM signal appears for ($\uparrow\rightarrow\rightarrow\uparrow$). This is equally observed for ($\rightarrow\uparrow\uparrow\rightarrow$). The modulation can be ascribed to a quantum beating with a period of $T_{beat} = 130 \pm 10$ fs and a corresponding energy splitting of $\Delta E = h/T_{beat} = 31.5 \pm 2.5$ meV which uncovers the negatively charged trion as the involved transition. (c), (d) The multidimensional spectroscopy maps (TR-FWM) by Hao et al. unfold an exciton-trion beating with a period of $T_{beat} = 130$ fs [Hao16a] which mainly is present for a cross-circular polarisation sequence [Hao17].

the first pulse ($\uparrow\rightarrow\rightarrow\rightarrow$) does only marginally affect the shape of the FWM trace (cf. figure 4.27(a)). This strikingly changes for a cross-linear polarisation sequence ($\uparrow\rightarrow\rightarrow\uparrow$) which is presented in figure 4.27(b). A clear modulation on top of the FWM signal appears which unequivocally can be identified as a quantum beating due to its periodic character, unfolding an oscillation period of $T_{beat} = 130 \pm 10$ fs. As expected, the same behaviour is observed for a turned polarisation ($\rightarrow\uparrow\uparrow\rightarrow$). The corresponding energy splitting of the states that give rise to the beating reveals $\Delta E = h/T_{beat} = 31.5 \pm 2.5$ meV and thereby unveils the negatively charged trion as the coupled transition [Ros13; Cou17]. Please note that in the here used two-beam FWM setup, the second and the third polarisation item is indispensably identical.

It has to be mentioned that a coherent coupling of the A exciton and the negatively charged trion in monolayer MoSe$_2$ has already been reported by several groups. First, Singh et al. report a coherent electronic coupling between excitons and trions which is deduced from two-colour pump-probe pump-probe differential reflectivity [Sin14]. It has to be emphasised that in their experiments, also a cross-linearly polarisation sequence has been employed in order to minimise noise. In addition, Jakubczyk et al. observe an exciton-trion beating in TI-FWM experiments [Jak16]. Their found beating period of $T_{beat} = 140$ fs is in very good accordance with ours. However, they do not comment on the specific polarisation which has been applied in their experiments. Furthermore, the multidimensional spectroscopy maps of Hao et al., which represents essentially spectrally resolved TR-FWM, equally evidence an exciton-trion beating with a period of $T_{beat} = 130$ fs [Hao16a]. The FWM response appears much more enhanced for a cross-circular polarisation sequence. Figures 4.27(c) and (d) show the main results of Hao et al. for co- and cross-circular excitation, respectively. As usual for 2D coherent spectroscopy, the excitation energy of the pulses is plotted against the emission frequency of the FWM whose intensity is given by the colour coding. Interestingly, the beating which manifests as off-diagonal element in the 2D spectroscopy map, exclusively emerges for a linearly cross-polarised pulse sequence. In addition, Shepard et al. perform gate-dependent interferometric dephasing time measurements on an encapsulated MoSe$_2$ monolayer and report coherent interactions with both trion species. They find beating periods of $T_{beat,X^-} = 162$ fs and $T_{beat,X^+} = 175$ fs for the negatively and positively charged trion, respectively [She17]. Most recent, the very detailed work of Rodek et al., conducting time-resolved three-beam FWM, elucidates the coherent exciton-trion coupling as a function of the free carrier density [Rod23]. They find a beating for a co-linear polarisation alignment which can be tuned by the gate voltage.
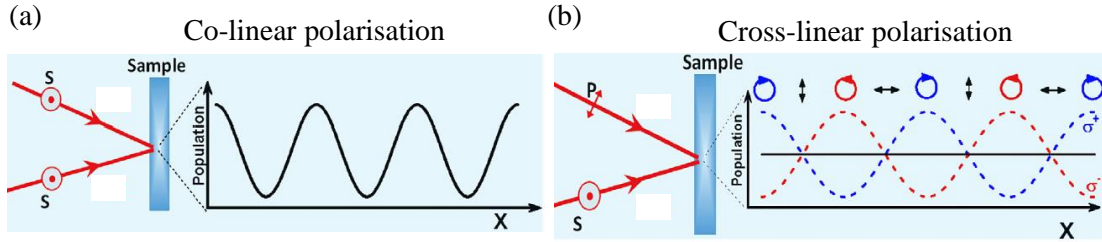
(a) Co-linear polarisation   (b) Cross-linear polarisation



**Figure 4.28: Formation of a spin grating due to cross-linear excitation** (a) For two linearly polarised plane waves that are incident under a certain angle, interference occurs, resulting in a spatially modulated density distribution. (b) In contrast, cross-linear polarisation of both waves give rise to a constant intensity but with spatially changing helicities that create an exciton population with alternating valley index. As a consequence, the polarisation of a linearly polarised beam which is diffracted on such a spin grating is rotated by 90°. Graphs reprinted from [Mah18].

In summary, the exciton-trion quantum beats in monolayer $MoSe_2$ have been no unprecedented discovery. Nonetheless, the intriguing aspect of our experiment hides in the particular polarisation sequences. At this point, it is unclear why exclusively the cross-linear polarisation sequence ($\rightarrow\uparrow\uparrow\rightarrow$) or vice versa causes a beating because in general, every combination of linear polarisation comprises $\sigma^+\sigma^-\sigma^+\sigma^-$ and $\sigma^-\sigma^+\sigma^-\sigma^+$. The fact, that we do not observe a beating signature for a co-linear polarisation alignment indicates that also the phase of the circular components of the laser pulses play a crucial role. A possible explanation for the absence of a beating in figures 4.27(a) and (c) might be the coexistence of two destructively interfering quantum beatings. For cross-linear pump-probe experiments, a spin grating forms instead of a population density grating which unfolds at co-linear polarisation as it has been proposed by multiple groups [Cam96; Wan13; Mah18; Kuh20]. A visualisation of the emergent spin grating is depicted in figure 4.28. In the case of linearly cross-polarised beams, the interference of two beams results in a homogeneous intensity but with spatial varying polarisation of $\sigma^- \uparrow \sigma^+ \rightarrow \sigma^-$... and so forth instead of a modulated intensity that forms under co-linear polarisation. Consequently, the cross-linear polarisation causes a constant exciton population with alternating valley index. The polarisation of a vertically polarised beam, interacting with such a grating, is changed to a horizontal polarisation and vice versa (assuming perfect Pauli-blocking) [Mah18].

In our experiments, the formation of the spin grating appears to figure the parameter that decides over the coherent exciton-trion interaction. As it is only possible to detect a beating with a detection that is orthogonal to the second pulse (which is virtually also the third) it is reasonable that the spin grating leads

to a turn of polarisation as discussed above. Beyond this statement, it is hard to phenomenologically draw a comprehensive picture that elucidates how the spin grating facilitates the coherent exciton-trion interaction. Most probable, elaborate theoretical modelling is needed to capture the complete mechanism.

In analogy to the investigations on monolayer MoSe$_2$, TI-FWM measurements on single-layer WSe$_2$ have been conducted. A series with different excitation energies and polarisation sequences are presented in figure 4.29. A very pronounced beating signature on the TI-FWM signal appears when the central laser energy is tuned to lower energies, i.e. towards the spectral position of the trion. The maximal beating signature is found for a central laser energy of 1722 meV which ranges exactly in-between exciton and the negatively charged triplet state trion [Jon13]. In contrast to monolayer MoSe$_2$, the dependence on the polarisation of excitation and detection is much more relaxed. An oscillation on the signal can be discerned for linear polarisation which augments at co-circular polarisation. The obtained beating period of T = 140 fs corresponds to an energy splitting of $\Delta E$ = 30 meV which coincides with the reported values for the difference in binding energy $\Delta E_{X_0 - X_T^-}$ = 30 meV of the exciton and the negatively charged trion [Li18; He20]. Besides, we note that biexcitons do not play a role in the here found phenomena because the formation of biexcitons is strongly suppressed for co-circular excitation [Ste18a].

In literature, there are very few reports about coherent exciton-trion interaction in monolayer WSe$_2$. Boule et al. perceive a beating in their TI-FWM data which they ascribe to the interaction of the $A_{2s}$ and $A_{3s}$ exciton state although the energy difference only poorly matches with the respective transitions [Bou20]. Moreover, the according oscillator strengths are very small. Dissimilar, no beating signatures can be remarked in our investigations for higher excitation energies. Instead, the here observed quantum beating unfolds for energies below the $A_{1s}$ exciton transition. As there are very few reports about FWM on WSe$_2$, it is helpful to concern literature about FWM performed on WS$_2$ because the valley structure is similar to WSe$_2$. Jakubczyk et al. have performed three-beam FWM, reporting a beating of the singlet and triplet trion for co-linear excitation [Jak18]. Apart from that, they do not notice any signs of an exciton-trion beating meanwhile they do not show results for co-circular polarisation which strongly boosts the exciton trion beating as it occurs in our measurements.

Concluding over the section, for both, MoSe$_2$ and WSe$_2$, a coherent coupling of exciton and trion, which are unequivocally identified by the energy splitting of the respective exciton and trion transitions, have been observed. While for MoSe$_2$, the exciton-trion coupling has been evidenced several times in literature, it ap-
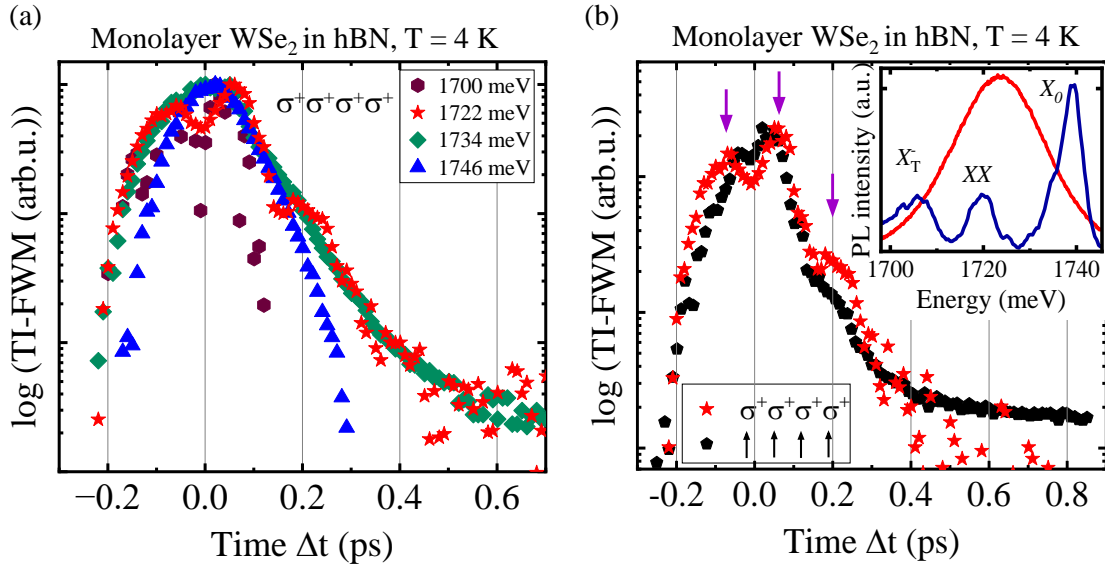
**Figure 4.29: Exciton-trion quantum beats in monolayer WSe$_2$ revealed by TI-FWM.** The four-fold polarisation sequence denotes the polarisations of pulses 1, 2, 3 and the detection. Linear polarisation is indicated by small black arrows. Spectra of the laser pulse (red) and the PL of the sample (blue) are depicted in the inset of (b). (a) An energy scan of the excitation energy (co-circular polarisation) evidences a quantum beating for energies at 1722 meV, well below the energy of the neutral exciton $X_0$. The spectral position of the laser pulse is kept at this energy where the beating amplitude is supreme. (b) For a co-linear polarisation alignment (black dots), the beating appears to be suppressed. Violet arrows indicate the maxima of the beating pattern. The obtained beating period of 140 fs corresponds to an energy splitting of 30 meV, matching perfectly the energy separation of the negatively charged trion $X_T^-$ and the neutral exciton $X_0$. Besides, biexcitons do not play a role in the here found mechanism because the formation of biexcitons is strongly quenched for co-circular excitation.

pears to be an unprecedented effect in WSe$_2$. For both cases, the polarisation of excitation and detection turns out to be crucial for the emergence of the quantum beating. Up to this point, it is difficult to embed the polarisation dependence into the actual landscape of FWM experiments. Theoretical modelling and further experimental results are imperative to unravel this issue.

# Chapter 5

# Conclusion and outlook

The last chapter is aimed to summarise over the distinct subjects of this PhD thesis and discuss future perspectives based on the results of this doctoral research study.

To start with, the determination of the sample temperature on sapphire substrates, making use of the sharp and intense PL emission lines from the unavoidable $Cr_3^+$ doping in this material has been presented. The evaluation of the two thermally populated ruby peaks serve as a powerful and simple approach to precisely determine the in-situ sample temperature, especially in the range of 30 - 100 K. Thereby, the common issues of bad thermal contact and laser heating can be assessed by optical means and an effective sample temperature can be determined. The scope of this thesis has been the investigation of the temporal dynamics exciton in mono- and multilayer TMDCs via transient differential transmission, time-resolved Faraday ellipticity and time-integrated four-wave mixing experiments, including sample fabrication, as well as their characterisation via photoluminescence and reflectance. Based on the findings of transient differential transmission and TRFE, a comprehensive picture of the the intricate valley dynamics of mono- and multilayer $MoSe_2$ and $WSe_2$ can be drawn. More specific, the different relaxation times are put into a reasonable context by considering the valley- and exciton fine structures, as well as the layer-dependent lowering of the $\Sigma$ valley. Moreover, the influence of in- and out-of-plane magnetic fields on the valley dynamics have been studied. Fingerprints of the valley Zeeman shift on the spin/valley relaxation dynamics are observed which manifest in a soft prolongation of the valley relaxation times. As an outstanding result among these findings, it is revealed that in CVD-grown monolayer $WSe_2$, the exciton lifetime is significantly reduced compared to exfoliated samples while the valley dephasing time remains completely unaffected. This behaviour has not been reported so far and points out that the

valley polarisation dynamics of CVD-grown TMDCs are exceptionally robust, affirming the potential of industrially produced devices for spin- or valleytronics.

The most prominent result of this thesis constitutes the discovery of ultrafast pseudospin quantum beats for H-type multilayer TMDCs exposed to in-plane magnetic fields. The existence of the beating implicates a valley Zeeman splitting which has never been observed for bulk TMDCs at in-plane magnetic fields so far. From the beating frequency, the effective excitonic g factor can be deduced with a very high accuracy without the need of high-magnetic field facilities. Moreover, it is shown that the excitonic g factor is isotropic.

Concluding over the last section about four-wave mixing spectroscopy, the results of the degenerate two-beam TI-FWM experiments integrate well in the established achievements on this topic. First, the influence of external magnetic fields on the coherent dynamics has been investigated. The analysis of the $T_2$ time does not reveal a significant enhancement or change of the dynamics. Besides, no signs of magnetically triggered multiple particle interactions have been observed. An exception has been found for monolayer $WSe_2$ where weak fingerprints of a magnetically induced coupling of the bright and dark exciton states is detected. Second, the impact of different polarisation sequences of the pulses that trigger the FWM response, as well as the polarisation component to which the detection is sensitive to, has been explored. For both monolayer materials, a coherent exciton-trion coupling, manifesting in a quantum beating, is detected. While for $MoSe_2$, a coherent coupling of exciton and trion has already been reported multiple times, it appears to be largely unexplored in $WSe_2$. For both cases, the polarisation of excitation and detection turns out to be decisive for the emergence of a quantum beating.

Moving towards future considerations, one of the most promising visions figures the full magneto-electrical control of the valley pseudospin in multilayer TMDCs. Hybridised exciton states in multilayer TMDCs are highly susceptible to external electric fields since they exhibit comparably large dipole moments along with much longer lifetimes than neutral intralayer excitons [Tag23]. The mutual application of electric and magnetic fields can be exploited to tune an excitonic transition, i.e. the contribution of hybridisation, allowing for a manipulation of excitonic g factors over more than one order of magnitude [Fen22; Far23]. With regard to the concept of valley pseudospin, a precise manipulation of this character is perceivable [Gon13; Li20; Alt22]. Technically, the manipulation of the exciton's pseudospin might be realised by a temporal sequence of electric and magnetic fields. This achievement would promote the concept of valley pseudospin significantly towards the fields of spintronics and quantum computing. More concrete,

106

this idea requests the fabrication and investigation of electrically gated samples which is already close to be realised by my successor Anna Weindl and our master student Jennifer Lehner. A major prospect beyond this work figures the deeper understanding of the nature of hybridised and/or dipolar excitonic states and its dynamics occurring in TMDC multilayers. With respect to this thesis, it remains open to clarify the origin of the pseudospin quantum beats at a microscopic level. Addressing this question, the production and investigation of high-quality R-type multilayers might shed light on this issue since for this stacking order, interlayer oscillations are momentum-forbidden. To complete the analysis of the pseudospin quantum beats, a more elaborate study of the dependence on the layer number could generate insights on the prevalent hybridisation processes since most of the recent investigations are realised on homobilayer systems [Erk23; Tag23; Hua22]. From a theoretical point of view, the modelling of the exciton fine structure in multilayer TMDCs, as well as their susceptibility to external magnetic fields is vital to elucidate the underlying principles.

Concerning future FWM experiments, the investigation of TMDCs in strong magnetic fields still hides a lot of intriguing phenomena since currently, there are very few reports available which, in addition, are based on rather rudimental data quality. Even more interesting may be the investigation of TMDC heterostructures where a TMDC is combined with a magnetic van der Waals material [Lee21; Wil21]. For instance, the antiferromagnetic semiconductor CrSBr recently has gained considerable attention [Kle22; Liu23; Ser23]. The possibility of switching its antiferromagnetic state to a ferromagnetic order by applying external magnetic fields, as well as the inverted band gap (type 3 band alignment) that appears in combination with a TMDC [Ser23] renders a very fascination scientific field. FWM on such a heterostructure may deliver important insights, illuminating the influence of proximity-induced magnetic fields on the coherent exciton dynamics.

Coming to an end, I would like to outline the complexity but also beauty of the excitonic landscape in multilayer TMDCs. The existence of spin-layer locking joined with the ability to control the excitonic properties via external fields establishes a prolific platform for generic concepts exploiting the valley pseudospin.

# Bibliography

[Aiv15]    G. Aivazian, Z. Gong, A. M. Jones, R.-L. Chu, J. Yan, D. G. Mandrus, C. Zhang, D. Cobden, W. Yao, and X. Xu. *Magnetic control of valley pseudospin in monolayer WSe2*. Nature Physics **11**, 148–152 (2015).

[Ale19]    E. M. Alexeev, D. A. Ruiz-Tijerina, M. Danovich, M. J. Hamer, D. J. Terry, P. K. Nayak, S. Ahn, S. Pak, J. Lee, J. I. Sohn, M. R. Molas, M. Koperski, K. Watanabe, T. Taniguchi, K. S. Novoselov, R. V. Gorbachev, H. S. Shin, V. I. Fal'ko, and A. I. Tartakovskii. *Resonantly hybridized excitons in moiré superlattices in van der Waals heterostructures*. Nature **567**, 81–86 (2019).

[Alt22]    M. M. Altaiary, E. Liu, C.-T. Liang, F.-C. Hsiao, J. van Baren, T. Taniguchi, K. Watanabe, N. M. Gabor, Y.-C. Chang, and C. H. Lui. *Electrically Switchable Intervalley Excitons with Strong Two-Phonon Scattering in Bilayer WSe2*. Nano letters **22**, 1829–1835 (2022).

[Ang18]    S. Anghel, F. Passmann, C. Ruppert, A. D. Bristow, and M. Betz. *Coupled exciton-trion spin dynamics in a MoSe 2 monolayer*. 2D Materials **5**, 045024 (2018).

[Ara09]    M. A. C. de Araújo, R. Silva, E. de Lima, D. P. Pereira, and P. C. de Oliveira. *Measurement of Gaussian laser beam radius using the knife-edge technique: improvement on data analysis*. Applied optics **48**, 393–396 (2009).

[Aro15]    A. Arora, M. Koperski, K. Nogajewski, J. Marcus, C. Faugeras, and M. Potemski. *Excitonic resonances in thin films of WSe2: from monolayer to bulk material*. Nanoscale **7**, 10421–10429 (2015).

[Aro16]    A. Arora, R. Schmidt, R. Schneider, M. R. Molas, I. Breslavetz, M. Potemski, and R. Bratschitsch. *Valley Zeeman Splitting and Valley Polarization of Neutral and Charged Excitons in Monolayer MoTe2 at High Magnetic Fields*. Nano letters **16**, 3624–3629 (2016).

*Bibliography*

[Aro17]     A. Arora, M. Drüppel, R. Schmidt, T. Deilmann, R. Schneider, M. R. Molas, P. Marauhn, S. Michaelis de Vasconcellos, M. Potemski, M. Rohlfing, and R. Bratschitsch. *Interlayer excitons in a bulk van der Waals semiconductor*. Nature communications **8**, 639 (2017).

[Aro18]     A. Arora, T. Deilmann, P. Marauhn, M. Drüppel, R. Schneider, M. R. Molas, D. Vaclavkova, S. Michaelis de Vasconcellos, M. Rohlfing, M. Potemski, and R. Bratschitsch. *Valley-contrasting optics of interlayer excitons in Mo- and W-based bulk transition metal dichalcogenides*. Nanoscale **10**, 15571–15577 (2018).

[Aro19]     A. Arora, M. Koperski, A. Slobodeniuk, K. Nogajewski, R. Schmidt, R. Schneider, M. R. Molas, S. M. de Vasconcellos, R. Bratschitsch, and M. Potemski. *Zeeman spectroscopy of excitons and hybridization of electronic states in few-layer WSe 2 , MoSe 2 and MoTe 2*. 2D Materials **6**, 015010 (2019).

[Aus93]     D. H. Auston. *Ultrashort Laser Pulses: Generation and Applications*. 2nd ed. Vol. v.60. Topics in Applied Physics Ser. Berlin, Heidelberg: Springer Berlin / Heidelberg, 1993.

[Bar73]     J. D. Barnett, S. Block, and G. J. Piermarini. *An Optical Fluorescence System for Quantitative Pressure Measurement in the Diamond-Anvil Cell*. Review of Scientific Instruments **44**, 1–9 (1973).

[Bau94]     J. J. Baumberg, S. A. Crooker, D. D. Awschalom, N. Samarth, H. Luo, and J. K. Furdyna. *Ultrafast Faraday spectroscopy in magnetic semiconductor quantum structures*. Physical review. B, Condensed matter **50**, 7689–7700 (1994).

[Ber13]     T. C. Berkelbach, M. S. Hybertsen, and D. R. Reichman. *Theory of neutral and charged excitons in monolayer transition metal dichalcogenides*. Physical Review B **88** (2013).

[Bin82]     G. Binning, H. Rohrer, C. Gerber, and E. and Weibel. *Surface Studies by Scanning Tunneling Microscopy*. Physical Review Letters **40** (1982).

[Bin86]     G. Binning, C. F. Quate, and C. F. and Gerber. *Atomic Force Microscope*. Physical Review Letters **56** (1986).

[Blo46]     F. Bloch. *Nuclear Induction*. Physical Review **70**, 460–474 (1946).

[Bol85]    F. Boldt, K. Henneberger, and V. May. *Many-Body Theory for the Dense Exciton Gas of Direct Semiconductors II. Calculation of Exciton Level Shift and Damping in Dependence on Exciton Density.* physica status solidi (b) **130**, 675–687 (1985).

[Bou20]    C. Boule, D. Vaclavkova, M. Bartos, K. Nogajewski, L. Zdražil, T. Taniguchi, K. Watanabe, M. Potemski, and J. Kasprzak. *Coherent dynamics and mapping of excitons in single-layer MoSe2 and WSe2 at the homogeneous limit.* Physical Review Materials **4** (2020).

[Bre19]    S. Brem, J. Zipfel, M. Selig, A. Raja, L. Waldecker, J. D. Ziegler, T. Taniguchi, K. Watanabe, A. Chernikov, and E. Malic. *Intrinsic lifetime of higher excitonic states in tungsten diselenide monolayers.* Nanoscale **11**, 12381–12387 (2019).

[Bro24]    L. de Broglie. *XXXV. A tentative theory of light quanta.* The London, Edinburgh, and Dublin Philosophical Magazine and Journal of Science **47**, 446–458 (1924).

[Bro72]    Bromley. *The band structures of some transition metal dichalcogenides. III. Group VIA: trigonal prism materials.* Phys._C _Solid_State_Phys. (1972).

[Buc23]    E. Buchholz. „Zeitaufgelöste Faraday-Messungen an CVD-gewachsenen WSe2-Monolagen". Bachelorarbeit. Regensburg: Universität Regensburg, 2023.

[Bus19]    J. H. Buss, H. Wang, Y. Xu, J. Maklar, F. Joucken, L. Zeng, S. Stoll, C. Jozwiak, J. Pepper, Y.-D. Chuang, J. D. Denlinger, Z. Hussain, A. Lanzara, and R. A. Kaindl. *A setup for extreme-ultraviolet ultrafast angle-resolved photoelectron spectroscopy at 50-kHz repetition rate.* The Review of scientific instruments **90**, 023105 (2019).

[Byr16]    S. J. Byrnes. *Multilayer optical calculations.* 2016.

[Cad17]    F. Cadiz, E. Courtade, C. Robert, G. Wang, Y. Shen, H. Cai, T. Taniguchi, K. Watanabe, H. Carrere, D. Lagarde, M. Manca, T. Amand, P. Renucci, S. Tongay, X. Marie, and B. Urbaszek. *Excitonic Linewidth Approaching the Homogeneous Limit in MoS2 -Based van der Waals Heterostructures.* Physical Review X **7** (2017).

[Cai18]    Z. Cai, B. Liu, X. Zou, and H.-M. Cheng. *Chemical Vapor Deposition Growth and Applications of Two-Dimensional Materials and Their Heterostructures.* Chemical reviews **118**, 6091–6133 (2018).

*Bibliography*

[Cam96]   A. R. Cameron, P. Riblet, and and A. Miller. *Spin Gratings and the Measurement of Electron Drift Mobility in Multiple Quantum Well Semiconductors*. Physical Review Letters **76** (1996).

[Cao12]   T. Cao, G. Wang, W. Han, H. Ye, C. Zhu, J. Shi, Q. Niu, P. Tan, E. Wang, B. Liu, and J. Feng. *Valley-selective circular dichroism of monolayer molybdenum disulphide*. Nature communications **3**, 887 (2012).

[Cao18]   Y. Cao, V. Fatemi, S. Fang, K. Watanabe, T. Taniguchi, E. Kaxiras, and P. Jarillo-Herrero. *Unconventional superconductivity in magic-angle graphene superlattices*. Nature **556**, 43–50 (2018).

[Car15]   B. R. Carvalho, L. M. Malard, J. M. Alves, C. Fantini, and M. A. Pimenta. *Symmetry-dependent exciton-phonon coupling in 2D and bulk MoS2 observed by resonance Raman scattering*. Physical review letters **114**, 136403 (2015).

[Cas14]   A. Castellanos-Gomez, M. Buscema, R. Molenaar, V. Singh, L. Janssen, H. S. J. van der Zant, and G. A. Steele. *Deterministic transfer of two-dimensional materials by all-dry viscoelastic stamping*. 2D Materials **1**, 011002 (2014).

[Che01]   D. S. Chemla and J. Shah. *Many-body and correlation effects in semiconductors*. Nature **411**, 549–557 (2001).

[Che14]   A. Chernikov, T. C. Berkelbach, H. M. Hill, A. Rigosi, Y. Li, O. B. Aslan, D. R. Reichman, M. S. Hybertsen, and T. F. Heinz. *Exciton binding energy and nonhydrogenic Rydberg series in monolayer WS(2)*. Physical review letters **113**, 076802 (2014).

[Cho17]   C. M. Chow, H. Yu, A. M. Jones, J. R. Schaibley, M. Koehler, D. G. Mandrus, R. Merlin, W. Yao, and X. Xu. *Phonon-assisted oscillatory exciton dynamics in monolayer MoSe2*. npj 2D Materials and Applications **1** (2017).

[Coe87]   R. Coehoorn, C. Haas, and R. A. de Groot. *Electronic structure of MoSe2, MoS2, and WSe2. II. The nature of the optical band gaps*. Physical review. B, Condensed matter **35**, 6203–6206 (1987).

[Cou17]   E. Courtade, M. Semina, M. Manca, M. M. Glazov, C. Robert, F. Cadiz, G. Wang, T. Taniguchi, K. Watanabe, M. Pierre, W. Escoffier, E. L. Ivchenko, P. Renucci, X. Marie, T. Amand, and B. Urbaszek. *Charged excitons in monolayer WSe2 : Experiment and theory*. Physical Review B **96** (2017).

112

[Cro97]   S. A. Crooker, D. D. Awschalom, J. J. Baumberg, F. Flack, and
          N. Samarth. *Optical spin resonance and transverse spin relaxation
          in magnetic semiconductor quantum wells.* Physical review. B, Con-
          densed matter **56**, 7574–7588 (1997).

[Cui14]   Q. Cui, F. Ceballos, N. Kumar, and H. Zhao. *Transient absorption mi-
          croscopy of monolayer and bulk WSe2.* ACS nano **8**, 2970–2976 (2014).

[Dal15]   S. Dal Conte, F. Bottegoni, E. A. A. Pogna, D. de Fazio, S. Ambro-
          gio, I. Bargigia, C. D'Andrea, A. Lombardo, M. Bruna, F. Ciccacci,
          A. C. Ferrari, G. Cerullo, and M. Finazzi. *Ultrafast valley relaxation
          dynamics in monolayer MoS2 probed by nonequilibrium optical tech-
          niques.* Physical Review B **92** (2015).

[Dei20]   T. Deilmann, P. Krüger, and M. Rohlfing. *Ab Initio Studies of Exciton
          g Factors: Monolayer Transition Metal Dichalcogenides in Magnetic
          Fields.* Physical review letters **124**, 226402 (2020).

[Dem13]   W. Demtröder. *Laserspektroskopie 2: Experimentelle Techniken.* 6. Aufl.
          2013. Berlin, Heidelberg: Springer Berlin Heidelberg, 2013.

[Dey16]   P. Dey, J. Paul, Z. Wang, C. E. Stevens, C. Liu, A. H. Romero, J.
          Shan, D. J. Hilton, and D. Karaiskaj. *Optical Coherence in Atomic-
          Monolayer Transition-Metal Dichalcogenides Limited by Electron-Phonon
          Interactions.* Physical review letters **116**, 127402 (2016).

[Dey17]   P. Dey, L. Yang, C. Robert, G. Wang, B. Urbaszek, X. Marie, and S. A.
          Crooker. *Gate-Controlled Spin-Valley Locking of Resident Carriers in
          WSe_2 Monolayers.* Physical review letters **119**, 137401 (2017).

[Dic23]   R. G. Dickinson and L. Pauling. *The crystal structure of molybdenite.*
          Journal of the American Chemical Society **1923** (1923).

[Don21]   S. Dong, M. Puppin, T. Pincelli, S. Beaulieu, D. Christiansen, H.
          Hübener, C. W. Nicholson, R. P. Xian, M. Dendzik, Y. Deng, Y. W.
          Windsor, M. Selig, E. Malic, A. Rubio, A. Knorr, M. Wolf, L. Rettig,
          and R. Ernstorfer. *Direct measurement of key exciton properties: En-
          ergy, dynamics, and spatial distribution of the wave function.* Natural
          Sciences **1** (2021).

[Ech16]   J. P. Echeverry, B. Urbaszek, T. Amand, X. Marie, and I. C. Gerber.
          *Splitting between bright and dark excitons in transition metal dichalco-
          genide monolayers.* Physical Review B **93** (2016).

# Bibliography

[Erk23]   D. Erkensten, S. Brem, R. Perea-Causin, J. Hagel, F. Tagarelli, E. Lopriore, A. Kis, and E. Malic. *Electrically tunable dipolar interactions between layer-hybridized excitons*. 2023.

[Eva67]   B. L. Evans. *Exciton spectra in thin crystals: the diamagnetic effect*. Proc. Phys. Soc. **91** (1967).

[Fal22]   D. Falter. „Zeitaufgelöste Faraday-Elliptizität zur Bestimmung des g-Faktors in WSe2". Master Thesis. Regensburg: Universität Regensburg, 2022.

[Fan19]   H. H. Fang, B. Han, C. Robert, M. A. Semina, D. Lagarde, E. Courtade, T. Taniguchi, K. Watanabe, T. Amand, B. Urbaszek, M. M. Glazov, and X. Marie. *Control of the Exciton Radiative Lifetime in van der Waals Heterostructures*. Physical review letters **123**, 067401 (2019).

[Far19]   P. E. Faria Junior, D. Tedeschi, M. de Luca, B. Scharf, A. Polimeni, and J. Fabian. *Common nonlinear features and spin-orbit coupling effects in the Zeeman splitting of novel wurtzite materials*. Physical Review B **99** (2019).

[Far23]   P. E. Faria Junior and J. Fabian. *Signatures of Electric Field and Layer Separation Effects on the Spin-Valley Physics of MoSe2/WSe2 Heterobilayers: From Energy Bands to Dipolar Excitons*. Nanomaterials (Basel, Switzerland) **13** (2023).

[Far46]   M. Faraday. *I. Experimental researches in electricity.—Nineteenth series*. Philosophical Transactions of the Royal Society of London **136**, 1–20 (1846).

[Fel22]   S. Feldl. „Zeitaufgelöste Faraday-Messungen an hBN-enkapsulierten WSe2-Monolagen". Bachelorabeit. Regensburg: Universität Regensburg, 2022.

[Fen22]   S. Feng, A. Campbell, M. Brotons-Gisbert, D. Andres-Penares, H. Baek, T. Taniguchi, K. Watanabe, B. Urbaszek, I. C. Gerber, and B. D. Gerardot. *Highly Tunable Ground and Excited State Excitonic Dipoles in Multilayer 2H-MoSe$_2$*. 2022.

[Feu91]   B. F. Feuerbacher, J. Kuhl, and K. and Ploog. *Biexcitonic contribution to the degenerate-four-wave-mixing signal from a GaAs/Al_xGa_1-xAs quantum well*. Physical Review B **43** (1991).

114

[För20]  J. Förste, N. V. Tepliakov, S. Y. Kruchinin, J. Lindlau, V. Funk, M. Förg, K. Watanabe, T. Taniguchi, A. S. Baimuratov, and A. Högele. *Exciton g-factors in monolayer and bilayer WSe2 from experiment and theory*. Nature communications **11**, 4539 (2020).

[For81]  R. L. Fork, B. I. Greene, and C. V. Shank. *Generation of optical pulses shorter than 0.1 psec by colliding pulse mode locking*. Applied Physics Letters **38**, 671–672 (1981).

[Fox12]  M. Fox. *Optical properties of solids*. 2 ed., (with corr.) Vol. 3. Oxford master series in physics Condensed matter physics. Oxford: Oxford Univ. Press, 2012.

[Fre37]  J. Frenkel. *Tightly bound excitons*. Phys. Rev. **1937** (1937).

[Fri63]  Frindt. *The optical properties of single crystals of WSe2 and MoTe2*. ournal of Physics and Chemistry of Solids **24** (1963).

[Gei13]  A. K. Geim and I. V. Grigorieva. *Van der Waals heterostructures*. Nature **499**, 419–425 (2013).

[Gib99]  J. Gibson and M. andChernuschenko. *Ruby films as surface temperature and pressure sensors*. Opt. Express, 443–448 (1999).

[Gla12]  M. M. Glazov. *Coherent spin dynamics of electrons and excitons in nanostructures (a review)*. Physics of the Solid State **54**, 1–27 (2012).

[Gla14]  M. M. Glazov, T. Amand, X. Marie, D. Lagarde, L. Bouet, and B. Urbaszek. *Exciton fine structure and spin decoherence in monolayers of transition metal dichalcogenides*. Physical Review B **89** (2014).

[Gla15]  M. M. Glazov, E. L. Ivchenko, G. Wang, T. Amand, X. Marie, B. Urbaszek, and B. L. Liu. *Spin and valley dynamics of excitons in transition metal dichalcogenide monolayers*. physica status solidi (b) **252**, 2349–2362 (2015).

[Gon13]  Z. Gong, G.-B. Liu, H. Yu, Di Xiao, X. Cui, X. Xu, and W. Yao. *Magnetoelectric effects and valley-controlled spin quantum gates in transition metal dichalcogenide bilayers*. Nature communications **4**, 2053 (2013).

[Gon20]  S.-H. Gong, I. Komen, F. Alpeggiani, and L. Kuipers. *Nanoscale Optical Addressing of Valley Pseudospins through Transverse Optical Spin*. Nano letters **20**, 4410–4415 (2020).

*Bibliography*

[Gor19]    M. Goryca, J. Li, A. V. Stier, T. Taniguchi, K. Watanabe, E. Cour-tade, S. Shree, C. Robert, B. Urbaszek, X. Marie, and S. A. Crooker. *Revealing exciton masses and dielectric properties of monolayer semi-conductors with high magnetic fields*. Nature communications **10**, 4172 (2019).

[Gra14]    C. Gradl, M. Kempf, D. Schuh, D. Bougeard, R. Winkler, C. Schüller, and T. Korn. *Hole-spin dynamics and hole g -factor anisotropy in coupled quantum well systems*. Physical Review B **90** (2014).

[Gra23]    M. Granados-Baez, A. Mukherjee, L. Qiu, C. Chakraborty, A. N. Vamivakas, and J. Cardenas. *Characterization of the on-chip cavity coupled emission of 2D materials at room temperature*. Optical Mate-rials Express **13**, 843 (2023).

[Gui18]    M. H. D. Guimarães and B. Koopmans. *Spin Accumulation and Dy-namics in Inversion-Symmetric van der Waals Crystals*. Physical re-view letters **120**, 266801 (2018).

[Hao16a]   K. Hao, G. Moody, F. Wu, C. K. Dass, L. Xu, C.-H. Chen, L. Sun, M.-Y. Li, L.-J. Li, A. H. MacDonald, and X. Li. *Direct measurement of exciton valley coherence in monolayer WSe2*. Nature Physics **12**, 677–682 (2016).

[Hao16b]   K. Hao, L. Xu, P. Nagler, A. Singh, K. Tran, C. K. Dass, C. Schüller, T. Korn, X. Li, and G. Moody. *Coherent and Incoherent Coupling Dy-namics between Neutral and Charged Excitons in Monolayer MoSe2*. Nano letters **16**, 5109–5113 (2016).

[Hao17]    K. Hao, J. F. Specht, P. Nagler, L. Xu, K. Tran, A. Singh, C. K. Dass, C. Schüller, T. Korn, M. Richter, A. Knorr, X. Li, and G. Moody. *Neu-tral and charged inter-valley biexcitons in monolayer MoSe2*. Nature communications **8**, 15552 (2017).

[Har71]    P. G. Harper and D. R. Edmodson. *Electronic band structure of the layer-type crystal MoS2 (atomic model)*. physica status solidi (b) **44**, 59–69 (1971).

[He20]     M. He, P. Rivera, D. van Tuan, N. P. Wilson, M. Yang, T. Taniguchi, K. Watanabe, J. Yan, D. G. Mandrus, H. Yu, H. Dery, W. Yao, and X. Xu. *Valley phonons and exciton complexes in a monolayer semi-conductor*. Nature communications **11**, 618 (2020).

[Hel21]  S. Helmrich, K. Sampson, Di Huang, M. Selig, K. Hao, K. Tran, A. Achstein, C. Young, A. Knorr, E. Malic, U. Woggon, N. Owschimikow, and X. Li. *Phonon-Assisted Intervalley Scattering Determines Ultrafast Exciton Dynamics in MoSe_2 Bilayers*. Physical review letters **127**, 157403 (2021).

[Hie97]  W. K. Hiebert, A. Stankiewicz, and M. R. Freeman. *Direct Observation of Magnetic Relaxation in a Small Permalloy Disk by Time-Resolved Scanning Kerr Microscopy*. Physical Review Letters **79** (1997).

[Hir20]  G. Hirschinger. „Ultrafast spectroscopy on single-layer MoSe2 in external magnetic fields". Master thesis. Regensburg: Uni Regensburg, 2020.

[Hol20]  J. Holler, L. Bauriedl, T. Korn, A. Seitz, F. Özyigit, M. Eichinger, C. Schüller, K. Watanabe, T. Taniguchi, C. Strunk, and N. Paradiso. *Air tightness of hBN encapsulation and its impact on Raman spectroscopy of van der Waals materials*. 2D Materials **7**, 015012 (2020).

[Hon89]  A. Honold, L. Schultheis, J. Kuhl, and C. W. Tu. *Collision broadening of two-dimensional excitons in a GaAs single quantum well*. Physical review. B, Condensed matter **40**, 6442–6445 (1989).

[Hos15]  M. Hosseini, M. Elahi, M. Pourfath, and D. Esseni. *Very large strain gauges based on single layer MoSe2 and WSe2 for sensing applications*. Applied Physics Letters **107** (2015).

[Hsu15]  W.-T. Hsu, Y.-L. Chen, C.-H. Chen, P.-S. Liu, T.-H. Hou, L.-J. Li, and W.-H. Chang. *Optically initialized robust valley-polarized holes in monolayer WSe2*. Nature communications **6**, 8963 (2015).

[Hsu17]  W.-T. Hsu, L.-S. Lu, D. Wang, J.-K. Huang, M.-Y. Li, T.-R. Chang, Y.-C. Chou, Z.-Y. Juang, H.-T. Jeng, L.-J. Li, and W.-H. Chang. *Evidence of indirect gap in monolayer WSe2*. Nature communications **8**, 929 (2017).

[Hua22]  Z. Huang, Y. Zhao, T. Bo, Y. Chu, J. Tian, Le Liu, Y. Yuan, F. Wu, J. Zhao, L. Xian, K. Watanabe, T. Taniguchi, R. Yang, D. Shi, L. Du, Z. Sun, S. Meng, W. Yang, and G. Zhang. *Spatially indirect intervalley excitons in bilayer WSe2*. Physical Review B **105** (2022).

[Ipp72]  E. P. Ippen, C. V. Shank, and A. Dienes. *Passive mode locking of the cw dye laser*. Applied Physics Letters **21**, 348–350 (1972).

*Bibliography*

[Jak16]    T. Jakubczyk, V. Delmonte, M. Koperski, K. Nogajewski, C. Faugeras, W. Langbein, M. Potemski, and J. Kasprzak. *Radiatively Limited Dephasing and Exciton Dynamics in MoSe2 Monolayers Revealed with Four-Wave Mixing Microscopy*. Nano letters **16**, 5333–5339 (2016).

[Jak18]    T. Jakubczyk, K. Nogajewski, M. R. Molas, M. Bartos, W. Langbein, M. Potemski, and J. Kasprzak. *Impact of environment on dynamics of exciton complexes in a WS 2 monolayer*. 2D Materials **5**, 031007 (2018).

[Jak19]    T. Jakubczyk, G. Nayak, L. Scarpelli, W.-L. Liu, S. Dubey, N. Bendiab, L. Marty, T. Taniguchi, K. Watanabe, F. Masia, G. Nogues, J. Coraux, W. Langbein, J. Renard, V. Bouchiat, and J. Kasprzak. *Coherence and Density Dynamics of Excitons in a Single-Layer MoS2 Reaching the Homogeneous Limit*. ACS nano **13**, 3500–3511 (2019).

[Jin19]    C. Jin, E. C. Regan, A. Yan, M. Iqbal Bakti Utama, D. Wang, S. Zhao, Y. Qin, S. Yang, Z. Zheng, S. Shi, K. Watanabe, T. Taniguchi, S. Tongay, A. Zettl, and F. Wang. *Observation of moiré excitons in WSe2/WS2 heterostructure superlattices*. Nature **567**, 76–80 (2019).

[Jon13]    A. M. Jones, H. Yu, N. J. Ghimire, S. Wu, G. Aivazian, J. S. Ross, B. Zhao, J. Yan, D. G. Mandrus, Di Xiao, W. Yao, and X. Xu. *Optical generation of excitonic valley coherence in monolayer WSe2*. Nature nanotechnology **8**, 634–638 (2013).

[Jon14]    A. M. Jones, H. Yu, J. S. Ross, P. Klement, N. J. Ghimire, J. Yan, D. G. Mandrus, W. Yao, and X. Xu. *Spin–layer locking effects in optical orientation of exciton spin in bilayer WSe2*. Nature Physics **10**, 130–134 (2014).

[Kan22]    T. Kang, T. W. Tang, B. Pan, H. Liu, K. Zhang, and Z. Luo. *Strategies for Controlled Growth of Transition Metal Dichalcogenides by Chemical Vapor Deposition for Integrated Electronics*. ACS materials Au **2**, 665–685 (2022).

[Kas06]    J. Kasprzak, M. Richard, S. Kundermann, A. Baas, P. Jeambrun, J. M. J. Keeling, F. M. Marchetti, M. H. Szymańska, R. André, J. L. Staehli, V. Savona, P. B. Littlewood, B. Deveaud, and S. Le Dang. *Bose-Einstein condensation of exciton polaritons*. Nature **443**, 409–414 (2006).

[Kat20]    F. Katsch, M. Selig, and A. Knorr. *Exciton-Scattering-Induced De-phasing in Two-Dimensional Semiconductors*. Physical review letters **124**, 257402 (2020).

[Kaz14]    T. Kazimierczuk, D. Fröhlich, S. Scheel, H. Stolz, and M. Bayer. *Gi-ant Rydberg excitons in the copper oxide Cu2O*. Nature **514**, 343–347 (2014).

[Kel79]    L. V. Keldysh. *Coulomb interaction in thin semiconductor and semimetal films*. JETP Lett. **29**, 658–661 (1979).

[Kik98]    J. M. Kikkawa and D. D. Awschalom. *Resonant Spin Amplification in n -Type GaAs*. Physical review letters **80**, 4313–4316 (1998).

[Kle22]    J. Klein, T. Pham, J. D. Thomsen, J. B. Curtis, T. Denneulin, M. Lorke, M. Florian, A. Steinhoff, R. A. Wiscons, J. Luxa, Z. Sofer, F. Jahnke, P. Narang, and F. M. Ross. *Control of structure and spin texture in the van der Waals layered magnet CrSBr*. Nature Communications **13**, 5420 (2022).

[Kli12]    C. Klingshirn. *Semiconductor Optics*. 4th ed. 2012. SpringerLink Bücher. Berlin, Heidelberg: Springer Berlin Heidelberg, 2012.

[Kne98]    P. Kner, W. Schäfer, R. Lövenich, and D. S. Chemla. *Coherence of Four-Particle Correlations in Semiconductors*. Physical Review Letters **81**, 5386–5389 (1998).

[Knu03]    M. Knupfer. *Exciton binding energies in organic semiconductors*. Applied Physics A **77**, 623–626 (2003).

[Kor15]    A. Kormányos, G. Burkard, M. Gmitra, J. Fabian, V. Zólyomi, N. D. Drummond, and V. Fal'ko. $k \cdot p$ *theory for two-dimensional transition metal dichalcogenide semiconductors*. 2D Materials **2**, 022001 (2015).

[Koś13]    K. Kośmider, J. W. González, and J. Fernández-Rossier. *Large spin splitting in the conduction band of transition metal dichalcogenide mono-layers*. Physical Review B **88** (2013).

[Kra27]    H. A. Kramers. *La diffusion de la lumiere par les atomes*. Atti Cong. Intern. Fisica (Transactions of Volta Centenary Congress) Como **2**, 545–557 (1927).

[Kro26]    L. R. de Kronig. *On the Theory of Dispersion of X-Rays*. Journal of the Optical Society of America **12**, 547 (1926).

Bibliography

[Kuh20]     H. Kuhn, J. Wagner, S. Han, R. Bernhardt, Y. Gao, L. Xiao, J. Zhu, and P. H. M. van Loosdrecht. *Excitonic Transport and Intervalley Scattering Dynamics in Large–Size Exfoliated MoSe 2 Monolayer Investigated by Heterodyned Transient Grating Spectroscopy*. Laser & Photonics Reviews **14** (2020).

[Kum14]     N. Kumar, Q. Cui, F. Ceballos, D. He, Y. Wang, and H. Zhao. *Exciton-exciton annihilation in MoSe 2 monolayers*. Physical Review B **89** (2014).

[Kun18]     J. Kunstmann, F. Mooshammer, P. Nagler, A. Chaves, F. Stein, N. Paradiso, G. Plechinger, C. Strunk, C. Schüller, G. Seifert, D. R. Reichman, and T. Korn. *Momentum-space indirect interlayer excitons in transition-metal dichalcogenide van der Waals heterostructures*. Nature Physics **14**, 801–805 (2018).

[Lan06]     W. Langbein and B. Patton. *Heterodyne spectral interferometry for multidimensional nonlinear spectroscopy of individual quantum systems*. Optics letters **31**, 1151–1153 (2006).

[Lee21]     K. Lee, A. H. Dismukes, E. J. Telford, R. A. Wiscons, J. Wang, X. Xu, C. Nuckolls, C. R. Dean, X. Roy, and X. Zhu. *Magnetic Order and Symmetry in the 2D Semiconductor CrSBr*. Nano Letters **21**, 3511–3517 (2021).

[Li07]     T. Li and G. Galli. *Electronic Properties of MoS 2 Nanoparticles*. The Journal of Physical Chemistry C **111**, 16192–16196 (2007).

[Li14]     Y. Li, J. Ludwig, T. Low, A. Chernikov, X. Cui, G. Arefe, Y. D. Kim, A. M. van der Zande, A. Rigosi, H. M. Hill, S. H. Kim, J. Hone, Z. Li, D. Smirnov, and T. F. Heinz. *Valley splitting and polarization by the Zeeman effect in monolayer MoSe2*. Physical review letters **113**, 266804 (2014).

[Li18]     Z. Li, T. Wang, Z. Lu, C. Jin, Y. Chen, Y. Meng, Z. Lian, T. Taniguchi, K. Watanabe, S. Zhang, D. Smirnov, and S.-F. Shi. *Revealing the biexciton and trion-exciton complexes in BN encapsulated WSe2*. Nature communications **9**, 3719 (2018).

[Li19]     Z. Li, T. Wang, C. Jin, Z. Lu, Z. Lian, Y. Meng, M. Blei, M. Gao, T. Taniguchi, K. Watanabe, T. Ren, T. Cao, S. Tongay, D. Smirnov, L. Zhang, and S.-F. Shi. *Momentum-Dark Intervalley Exciton in Monolayer Tungsten Diselenide Brightened via Chiral Phonon*. ACS nano **13**, 14107–14113 (2019).

[Li20]     Y. Li, X. Wei, J. Ye, G. Zhai, K. Wang, and X. Zhang. *Gate-controlled spin relaxation in bulk WSe 2 flakes*. AIP Advances **10**, 045315 (2020).

[Liu13]    G.-B. Liu, W.-Y. Shan, Y. Yao, W. Yao, and Di Xiao. *Three-band tight-binding model for monolayers of group-VIB transition metal dichalcogenides*. Physical Review B **88** (2013).

[Liu16]    Y. Liu, N. O. Weiss, X. Duan, H.-C. Cheng, Y. Huang, and X. Duan. *Van der Waals heterostructures and devices*. Nature Reviews Materials **1** (2016).

[Liu19]    E. Liu, J. van Baren, Z. Lu, M. M. Altaiary, T. Taniguchi, K. Watanabe, D. Smirnov, and C. H. Lui. *Gate Tunable Dark Trions in Monolayer WSe_ 2*. Physical review letters **123**, 027401 (2019).

[Liu23]    F. Liu. *Time- and angle-resolved photoemission spectroscopy (TR-ARPES) of TMDC monolayers and bilayers*. Chemical science **14**, 736–750 (2023).

[Lu20]     Z. Lu, D. Rhodes, Z. Li, D. van Tuan, Y. Jiang, J. Ludwig, Z. Jiang, Z. Lian, S.-F. Shi, J. Hone, H. Dery, and D. Smirnov. *Magnetic field mixing and splitting of bright and dark excitons in monolayer MoSe 2*. 2D Materials **7**, 015017 (2020).

[Mac15]    D. MacNeill, C. Heikes, K. F. Mak, Z. Anderson, A. Kormányos, V. Zólyomi, J. Park, and D. C. Ralph. *Breaking of valley degeneracy by magnetic field in monolayer MoSe2*. Physical review letters **114**, 037401 (2015).

[Mad20]    J. Madéo, M. K. L. Man, C. Sahoo, M. Campbell, V. Pareek, E. L. Wong, A. Al-Mahboob, N. S. Chan, A. Karmakar, B. M. K. Mariserla, X. Li, T. F. Heinz, T. Cao, and K. M. Dani. *Directly visualizing the momentum-forbidden dark excitons and their dynamics in atomically thin semiconductors*. Science (New York, N.Y.) **370**, 1199–1204 (2020).

[Mah18]    F. Mahmood, Z. Alpichshev, Y.-H. Lee, J. Kong, and N. Gedik. *Observation of Exciton-Exciton Interaction Mediated Valley Depolarization in Monolayer MoSe2*. Nano letters **18**, 223–228 (2018).

[Mai60]    T. Maiman. *Stimulated Optical Radiation in Ruby*. Nature **187**, 493–494 (1960).

[Mai93]    M. Z. Maialle, E. A. de Andrada e Silva, and and L. J. Sham. *Exciton spin dynamics in quantum wells*. Physical Review B **47** (1993).

*Bibliography*

[Mai94]    M. Z. Maialle and L. J. Sham. *Interacting electron theory of coherent nonlinear response*. Physical Review Letters **73**, 3310–3313 (1994).

[Mak10]    K. F. Mak, C. Lee, J. Hone, J. Shan, and T. F. Heinz. *Atomically thin MoS$_2$: a new direct-gap semiconductor*. Physical review letters **105**, 136805 (2010).

[Mak12]    K. F. Mak, K. He, J. Shan, and T. F. Heinz. *Control of valley polarization in monolayer MoS2 by optical helicity*. Nature nanotechnology **7**, 494–498 (2012).

[Mak13]    K. F. Mak, K. He, C. Lee, G. H. Lee, J. Hone, T. F. Heinz, and J. Shan. *Tightly bound trions in monolayer MoS2*. Nature materials **12**, 207–211 (2013).

[Map22]    V. Mapara, A. Barua, V. Turkowski, M. T. Trinh, C. Stevens, H. Liu, F. A. Nugera, N. Kapuruge, H. R. Gutierrez, F. Liu, X. Zhu, D. Semenov, S. A. McGill, N. Pradhan, D. J. Hilton, and D. Karaiskaj. *Bright and Dark Exciton Coherent Coupling and Hybridization Enabled by External Magnetic Fields*. Nano letters **22**, 1680–1687 (2022).

[Mer20]    P. Merkl, F. Mooshammer, S. Brem, A. Girnghuber, K.-Q. Lin, L. Weigl, M. Liebich, C.-K. Yong, R. Gillen, J. Maultzsch, J. M. Lupton, E. Malic, and R. Huber. *Twist-tailoring Coulomb correlations in van der Waals homobilayers*. Nature communications **11**, 2167 (2020).

[Mil85]    R. C. Miller and D. A. Kleinman. *Excitons in GaAs quantum wells*. Journal of Luminescence **30** (1985).

[Mit15]    A. A. Mitioglu, P. Plochocka, Á. Del Granados Aguila, P. C. M. Christianen, G. Deligeorgis, S. Anghel, L. Kulyuk, and D. K. Maude. *Optical Investigation of Monolayer and Bulk Tungsten Diselenide (WSe$_2$) in High Magnetic Fields*. Nano letters **15**, 4387–4392 (2015).

[Mit16]    A. A. Mitioglu, K. Galkowski, A. Surrente, L. Klopotowski, D. Dumcenco, A. Kis, D. K. Maude, and P. Plochocka. *Magnetoexcitons in large area CVD-grown monolayer MoS2 and MoSe2 on sapphire*. Physical Review B **93** (2016).

[Mol17]    M. R. Molas, C. Faugeras, A. O. Slobodeniuk, K. Nogajewski, M. Bartos, D. M. Basko, and M. Potemski. *Brightening of dark excitons in monolayers of semiconducting transition metal dichalcogenides*. 2D Materials **4**, 021003 (2017).

[Moo15]   G. Moody, C. Kavir Dass, K. Hao, C.-H. Chen, L.-J. Li, A. Singh, K. Tran, G. Clark, X. Xu, G. Berghäuser, E. Malic, A. Knorr, and X. Li. *Intrinsic homogeneous linewidth and broadening mechanisms of excitons in monolayer transition metal dichalcogenides*. Nature communications **6**, 8315 (2015).

[Moo16]   G. Moody, J. Schaibley, and X. Xu. *Exciton Dynamics in Monolayer Transition Metal Dichalcogenides*. Journal of the Optical Society of America. B, Optical physics **33**, C39–C49 (2016).

[Mue18]   T. Mueller and E. Malic. *Exciton physics and device application of two-dimensional transition metal dichalcogenide semiconductors*. npj 2D Materials and Applications **2** (2018).

[Mun19]   B. Munkhbat, D. G. Baranov, M. Stührenberg, M. Wersäll, A. Bisht, and T. Shegai. *Self-Hybridized Exciton-Polaritons in Multilayers of Transition Metal Dichalcogenides for Efficient Light Absorption*. ACS Photonics **6**, 139–147 (2019).

[Niu18]   Y. Niu, S. Gonzalez-Abad, R. Frisenda, P. Marauhn, M. Drüppel, P. Gant, R. Schmidt, N. S. Taghavi, D. Barcons, A. J. Molina-Mendoza, S. M. de Vasconcellos, R. Bratschitsch, D. Perez De Lara, M. Rohlfing, and A. Castellanos-Gomez. *Thickness-Dependent Differential Reflectance Spectra of Monolayer and Few-Layer $MoS_2$, $MoSe_2$, $WS_2$ and $WSe_2$*. Nanomaterials (Basel, Switzerland) **8** (2018).

[Nov04]   K. S. Novoselov. *Electric Field Effect in Atomically Thin Carbon Films*. Science (New York, N.Y.) **306** (2004).

[Nov16]   K. S. Novoselov, A. Mishchenko, A. Carvalho, and A. H. Castro Neto. *2D materials and van der Waals heterostructures*. Science (New York, N.Y.) **353**, aac9439 (2016).

[Par20]   I. Paradisanos, S. Shree, A. George, N. Leisgang, C. Robert, K. Watanabe, T. Taniguchi, R. J. Warburton, A. Turchanin, X. Marie, I. C. Gerber, and B. Urbaszek. *Controlling interlayer excitons in MoS2 layers grown by chemical vapor deposition*. Nature Communications **11**, 2391 (2020).

[Pei14]   M. F. Peintinger, M. J. Kratz, and T. Bredow. *Quantum-chemical study of stable, meta-stable and high-pressure alumina polymorphs and aluminum hydroxides*. J. Mater. Chem. A **2**, 13143–13158 (2014).

*Bibliography*

[Ple16]   G. Plechinger, P. Nagler, A. Arora, R. Schmidt, A. Chernikov, A. G. Del Águila, P. C. M. Christianen, R. Bratschitsch, C. Schüller, and T. Korn. *Trion fine structure and coupled spin-valley dynamics in monolayer tungsten disulfide.* Nature communications **7**, 12715 (2016).

[Poe15]   C. Poellmann, P. Steinleitner, U. Leierseder, P. Nagler, G. Plechinger, M. Porer, R. Bratschitsch, C. Schüller, T. Korn, and R. Huber. *Resonant internal quantum transitions and femtosecond radiative decay of excitons in monolayer WSe2.* Nature materials **14**, 889–893 (2015).

[Pur18]   D. G. Purdie, N. M. Pugno, T. Taniguchi, K. Watanabe, A. C. Ferrari, and A. Lombardo. *Cleaning interfaces in layered materials heterostructures.* Nature Communications **9**, 5387 (2018).

[Qiu13]   D. Y. Qiu, F. H. Da Jornada, and S. G. Louie. *Optical spectrum of MoS2: many-body effects and diversity of exciton states.* Physical review letters **111**, 216805 (2013).

[Rai19]   S. Raiber. „Time-resolved Faraday measurements on atomically thin MoSe2 in external magnetic fields". Master thesis. Universität Regensburg, 2019.

[Rai22]   S. Raiber, P. E. Faria Junior, D. Falter, S. Feldl, P. Marzena, K. Watanabe, T. Taniguchi, J. Fabian, and C. Schüller. *Ultrafast pseudospin quantum beats in multilayer WSe2 and MoSe2.* Nature Communications **13**, 4997 (2022).

[Raj17]   A. Raja, A. Chaves, J. Yu, G. Arefe, H. M. Hill, A. F. Rigosi, T. C. Berkelbach, P. Nagler, C. Schüller, T. Korn, C. Nuckolls, J. Hone, L. E. Brus, T. F. Heinz, D. R. Reichman, and A. Chernikov. *Coulomb engineering of the bandgap and excitons in two-dimensional materials.* Nature communications **8**, 15251 (2017).

[Raj18]   A. Raja, M. Selig, G. Berghäuser, J. Yu, H. M. Hill, A. F. Rigosi, L. E. Brus, A. Knorr, T. F. Heinz, E. Malic, and A. Chernikov. *Enhancement of Exciton–Phonon Scattering from Monolayer to Bilayer WS 2.* Nano Letters **18**, 6135–6143 (2018).

[Raj19]   A. Raja, L. Waldecker, J. Zipfel, Y. Cho, S. Brem, J. D. Ziegler, M. Kulig, T. Taniguchi, K. Watanabe, E. Malic, T. F. Heinz, T. C. Berkelbach, and A. Chernikov. *Dielectric disorder in two-dimensional materials.* Nature nanotechnology **14**, 832–837 (2019).

[Ram12]   A. Ramasubramaniam. *Large excitonic effects in monolayers of molybdenum and tungsten dichalcogenides.* Physical Review B **86** (2012).

[Raz17]   E. Razzoli, T. Jaouen, M.-L. Mottas, B. Hildebrand, G. Monney, A. Pisoni, S. Muff, M. Fanciulli, N. C. Plumb, V. A. Rogalev, V. N. Strocov, J. Mesot, M. Shi, J. H. Dil, H. Beck, and P. Aebi. *Selective Probing of Hidden Spin-Polarized States in Inversion-Symmetric Bulk MoS_2*. Physical review letters **118**, 086402 (2017).

[Rho19]   D. Rhodes, S. H. Chae, R. Ribeiro-Palau, and J. Hone. *Disorder in van der Waals heterostructures of 2D materials*. Nature materials **18**, 541–549 (2019).

[Riv15]   P. Rivera, J. R. Schaibley, A. M. Jones, J. S. Ross, S. Wu, G. Aivazian, P. Klement, K. Seyler, G. Clark, N. J. Ghimire, J. Yan, D. G. Mandrus, W. Yao, and X. Xu. *Observation of long-lived interlayer excitons in monolayer MoSe2-WSe2 heterostructures*. Nature communications **6**, 6242 (2015).

[Riv16]   P. Rivera, K. L. Seyler, H. Yu, J. R. Schaibley, J. Yan, D. G. Mandrus, W. Yao, and X. Xu. *Valley-polarized exciton dynamics in a 2D semiconductor heterostructure*. Science (New York, N.Y.) **351**, 688–691 (2016).

[Rob17]   C. Robert, T. Amand, F. Cadiz, D. Lagarde, E. Courtade, M. Manca, T. Taniguchi, K. Watanabe, B. Urbaszek, and X. Marie. *Fine structure and lifetime of dark excitons in transition metal dichalcogenide monolayers*. Physical Review B **96** (2017).

[Rob20]   C. Robert, B. Han, P. Kapuscinski, A. Delhomme, C. Faugeras, T. Amand, M. R. Molas, M. Bartos, K. Watanabe, T. Taniguchi, B. Urbaszek, M. Potemski, and X. Marie. *Measurement of the spin-forbidden dark excitons in MoS2 and MoSe2 monolayers*. Nature communications **11**, 4037 (2020).

[Rod23]   A. Rodek, T. Hahn, J. Howarth, T. Taniguchi, K. Watanabe, M. Potemski, P. Kossacki, D. Wigger, and J. Kasprzak. *Controlled coherent-coupling and dynamics of exciton complexes in a MoSe 2 monolayer*. 2D Materials **10**, 025027 (2023).

[Roj23]   R. R. Rojas-Lopez, F. Hendriks, C. H. van der Wal, P. S. S. Guimarães, and M. H. D. Guimarães. *Magnetic field control of light-induced spin accumulation in monolayer MoSe 2*. 2D Materials **10**, 035013 (2023).

# Bibliography

[Ros13]    J. S. Ross, S. Wu, H. Yu, N. J. Ghimire, A. M. Jones, G. Aivazian, J. Yan, D. G. Mandrus, Di Xiao, W. Yao, and X. Xu. *Electrical control of neutral and charged excitons in a monolayer semiconductor*. Nature communications **4**, 1474 (2013).

[Ros20]    M. R. Rosenberger, H.-J. Chuang, M. Phillips, V. P. Oleshko, K. M. McCreary, S. V. Sivaram, C. S. Hellberg, and B. T. Jonker. *Twist Angle-Dependent Atomic Reconstruction and Moiré Patterns in Transition Metal Dichalcogenide Heterostructures*. ACS nano **14**, 4550–4558 (2020).

[Sca17]    L. Scarpelli, F. Masia, E. M. Alexeev, F. Withers, A. I. Tartakovskii, K. S. Novoselov, and W. Langbein. *Resonantly excited exciton dynamics in two-dimensional MoSe2 monolayers*. Physical Review B **96** (2017).

[Sch17]    M. Schwemmer, P. Nagler, A. Hanninger, C. Schüller, and T. Korn. *Long-lived spin polarization in n-doped MoSe 2 monolayers*. Applied Physics Letters **111**, 082404 (2017).

[Sch85]    S. Schmitt-Rink, D. S. Chemla, and and D. A. B. Miller, D. A. B. *Theory of transient excitonic optical nonlinearities in semiconductor quantum-well structures*. Physical Review B **10** (1985).

[Sch87]    W. J. Schutte, J. L. de Boer, and F. Jellinek. *Crystal structures of tungsten disulfide and diselenide*. Journal of Solid State Chemistry **70**, 207–209 (1987).

[Sel19]    M. Selig, F. Katsch, R. Schmidt, S. Michaelis de Vasconcellos, R. Bratschitsch, E. Malic, and A. Knorr. *Ultrafast dynamics in monolayer transition metal dichalcogenides: Interplay of dark excitons, phonons, and intervalley exchange*. Physical Review Research **1** (2019).

[Ser23]    C. Serati de Brito, P. E. Faria Junior, T. S. Ghiasi, J. Ingla-Aynés, C. R. Rabahi, C. Cavalini, F. Dirnberger, S. Mañas-Valero, K. Watanabe, T. Taniguchi, K. Zollner, J. Fabian, C. Schüller, H. S. J. van der Zant, and Y. G. Gobato. *Charge Transfer and Asymmetric Coupling of MoSe2 Valleys to the Magnetic Order of CrSBr*. Nano letters (2023).

[Sey19]    K. L. Seyler, P. Rivera, H. Yu, N. P. Wilson, E. L. Ray, D. G. Mandrus, J. Yan, W. Yao, and X. Xu. *Signatures of moiré-trapped valley excitons in MoSe2/WSe2 heterobilayers*. Nature **567**, 66–70 (2019).

[Sha13]   J. Shah, M. Cardona, P. Fulde, K. V. Klitzing, and H. J. Queisser. *Ultrafast Spectroscopy of Semiconductors and Semiconductor Nanostructures*. 2nd ed. Vol. v. 115. Springer Series in Solid-State Sciences Ser. Berlin, Heidelberg: Springer Berlin / Heidelberg, 2013.

[She17]   G. D. Shepard, J. V. Ardelean, O. A. Ajayi, D. Rhodes, X. Zhu, J. C. Hone, and S. Strauf. *Trion-Species-Resolved Quantum Beats in MoSe2*. ACS nano **11**, 11550–11558 (2017).

[Shi22]   Q. Shi, E.-M. Shih, D. Rhodes, B. Kim, K. Barmak, K. Watanabe, T. Taniguchi, Z. Papić, D. A. Abanin, J. Hone, and C. R. Dean. *Bilayer WSe2 as a natural platform for interlayer exciton condensates in the strong coupling limit*. Nature nanotechnology **17**, 577–582 (2022).

[Sid17]   M. Sidler, P. Back, O. Cotlet, A. Srivastava, T. Fink, M. Kroner, E. Demler, and A. Imamoglu. *Fermi polaron-polaritons in charge-tunable atomically thin semiconductors*. Nature Physics **13**, 255–261 (2017).

[Sie15]   E. J. Sie, A. J. Frenzel, Y.-H. Lee, J. Kong, and N. Gedik. *Intervalley biexcitons and many-body effects in monolayer MoS2*. Physical Review B **92** (2015).

[Sig18]   M. W. Sigrist. *Laser: Theorie, Typen und Anwendungen*. 8. Aufl. 2018. Berlin, Heidelberg: Springer Berlin Heidelberg, 2018.

[Sin14]   A. Singh, G. Moody, S. Wu, Y. Wu, N. J. Ghimire, J. Yan, D. G. Mandrus, X. Xu, and X. Li. *Coherent Electronic Coupling in Atomically Thin MoSe2*. Physical Review Letters **112** (2014).

[Slo19]   A. O. Slobodeniuk, Ł. Bala, M. Koperski, M. R. Molas, P. Kossacki, K. Nogajewski, M. Bartos, K. Watanabe, T. Taniguchi, C. Faugeras, and M. Potemski. *Fine structure of K-excitons in multilayers of transition metal dichalcogenides*. 2D Materials **6**, 025026 (2019).

[Spl10]   A. Splendiani, L. Sun, Y. Zhang, T. Li, J. Kim, C.-Y. Chim, G. Galli, and F. Wang. *Emerging photoluminescence in monolayer MoS2*. Nano letters **10**, 1271–1275 (2010).

[Spo22]   L. Sponfeldner, N. Leisgang, S. Shree, I. Paradisanos, K. Watanabe, T. Taniguchi, C. Robert, D. Lagarde, A. Balocchi, X. Marie, I. C. Gerber, B. Urbaszek, and R. J. Warburton. *Capacitively and Inductively Coupled Excitons in Bilayer MoS_2*. Physical review letters **129**, 107401 (2022).

*Bibliography*

[Sri15]    A. Srivastava, M. Sidler, A. V. Allain, D. S. Lembke, A. Kis, and A. Imamoğlu. *Valley Zeeman effect in elementary optical excitations of monolayer WSe2*. Nature Physics **11**, 141–147 (2015).

[Ste17]    A. Steinhoff, M. Florian, M. Rösner, G. Schönhoff, T. O. Wehling, and F. Jahnke. *Exciton fission in monolayer transition metal dichalcogenide semiconductors*. Nature communications **8**, 1166 (2017).

[Ste18a]    A. Steinhoff, M. Florian, A. Singh, K. Tran, M. Kolarczik, S. Helmrich, A. W. Achtstein, U. Woggon, N. Owschimikow, F. Jahnke, and X. Li. *Biexciton fine structure in monolayer transition metal dichalcogenides*. Nature Physics **14**, 1199–1204 (2018).

[Ste18b]    C. E. Stevens, J. Paul, T. Cox, P. K. Sahoo, H. R. Gutiérrez, V. Turkowski, D. Semenov, S. A. McGill, M. D. Kapetanakis, I. E. Perakis, D. J. Hilton, and D. Karaiskaj. *Biexcitons in monolayer transition metal dichalcogenides tuned by magnetic fields*. Nature communications **9**, 3720 (2018).

[Sti16]    A. V. Stier, K. M. McCreary, B. T. Jonker, J. Kono, and S. A. Crooker. *Exciton diamagnetic shifts and valley Zeeman effects in monolayer WS2 and MoS2 to 65 Tesla*. Nature communications **7**, 10643 (2016).

[Sti18]    A. V. Stier, N. P. Wilson, K. A. Velizhanin, J. Kono, X. Xu, and S. A. Crooker. *Magnetooptics of Exciton Rydberg States in a Monolayer Semiconductor*. Physical review letters **120**, 057405 (2018).

[Stö06]    J. Stöhr, H.-C. Siegmann, and H. C. Siegmann. *Magnetism: From fundamentals to nanoscale dynamics ; with 325 figures and 39 tables*. Vol. 152. Springer series in solid-state sciences. Berlin and Heidelberg: Springer, 2006.

[Tag23]    F. Tagarelli, E. Lopriore, D. Erkensten, R. Perea-Causín, S. Brem, J. Hagel, Z. Sun, G. Pasquale, K. Watanabe, T. Taniguchi, E. Malic, and A. Kis. *Electrical control of hybrid exciton transport in a van der Waals heterostructure*. Nature photonics **17**, 615–621 (2023).

[Ter14]    H. Terrones and M. Terrones. *Bilayers of transition metal dichalcogenides: Different stackings and heterostructures*. Journal of Materials Research **29**, 373–382 (2014).

[Tha20]    K. Thakar and S. Lodha. *Optoelectronic and photonic devices based on transition metal dichalcogenides*. Materials Research Express **7**, 014002 (2020).

[Tor18]     H. Tornatzky, A.-M. Kaulitz, and J. Maultzsch. *Resonance Profiles of Valley Polarization in Single-Layer MoS_2 and MoSe_2*. Physical review letters **121**, 167401 (2018).

[Tra19]     K. Tran, G. Moody, F. Wu, X. Lu, J. Choi, K. Kim, A. Rai, D. A. Sanchez, J. Quan, A. Singh, J. Embley, A. Zepeda, M. Campbell, T. Autry, T. Taniguchi, K. Watanabe, N. Lu, S. K. Banerjee, K. L. Silverman, S. Kim, E. Tutuc, L. Yang, A. H. MacDonald, and X. Li. *Evidence for moiré excitons in van der Waals heterostructures*. Nature **567**, 71–75 (2019).

[van14]     A. M. van der Zande, J. Kunstmann, A. Chernikov, D. A. Chenet, Y. You, X. Zhang, P. Y. Huang, T. C. Berkelbach, L. Wang, F. Zhang, M. S. Hybertsen, D. A. Muller, D. R. Reichman, T. F. Heinz, and J. C. Hone. *Tailoring the electronic structure in bilayer molybdenum disulfide via interlayer twist*. Nano letters **14**, 3869–3875 (2014).

[Ven77]     H. Venghaus, S. Suga, and and K. Cho. *Magnetoluminescence and magnetoreflectance of the A exciton of CdS and CdSe*. **16** (1977).

[Wag23]     K. Wagner. „Exciton diffusion and interactions with a two-dimensional Fermi sea". Phd thesis. Universität Regensburg, 2023.

[Wag97]     H. P. Wagner, A. Schätz, R. Maier, W. Langbein, and J. M. Hvam. *Coherent optical nonlinearities and phase relaxation of quasi-three-dimensional and quasi-two-dimensional excitons in ZnSxSe1−x/ZnSe structures*. Physical review. B, Condensed matter **56**, 12581–12588 (1997).

[Wal12]     M. P. Walser, C. Reichl, W. Wegscheider, and G. Salis. *Direct mapping of the formation of a persistent spin helix*. Nature Physics **8**, 757–762 (2012).

[Wal16]     R. Wallauer, J. Reimann, N. Armbrust, J. Güdde, and U. Höfer. *Intervalley scattering in MoS2 imaged by two-photon photoemission with a high-harmonic probe*. Applied Physics Letters **109** (2016).

[Wal21]     R. Wallauer, R. Perea-Causin, L. Münster, S. Zajusch, S. Brem, J. Güdde, K. Tanimura, K.-Q. Lin, R. Huber, E. Malic, and U. Höfer. *Momentum-Resolved Observation of Exciton Formation Dynamics in Monolayer WS2*. Nano letters **21**, 5867–5873 (2021).

*Bibliography*

[Wan13]   G. Wang, B. L. Liu, A. Balocchi, P. Renucci, C. R. Zhu, T. Amand, C. Fontaine, and X. Marie. *Gate control of the electron spin-diffusion length in semiconductor quantum wells.* Nature communications **4**, 2372 (2013).

[Wan15a]  G. Wang, I. C. Gerber, L. Bouet, D. Lagarde, A. Balocchi, M. Vidal, T. Amand, X. Marie, and B. Urbaszek. *Exciton states in monolayer MoSe 2 : impact on interband transitions.* 2D Materials **2**, 045005 (2015).

[Wan15b]  G. Wang, E. Palleau, T. Amand, S. Tongay, X. Marie, and B. Urbaszek. *Polarization and time-resolved photoluminescence spectroscopy of excitons in MoSe 2 monolayers.* Applied Physics Letters **106**, 112101 (2015).

[Wan18]   G. Wang, A. Chernikov, M. M. Glazov, T. F. Heinz, X. Marie, T. Amand, and B. Urbaszek. *Colloquium : Excitons in atomically thin transition metal dichalcogenides.* Reviews of Modern Physics **90** (2018).

[Wan37]   G. H. Wannier. *The Structure of Electronic Excitation Levels in Insulating Crystals.* Phys. Rev. **1937** (1937).

[Wan93]   H. Wang, Kyle Ferrio, Duncan G. Steel, Y. Z. Hu, R. Binder, and and S. W. Koch. *Transient nonlinear optical response from excitation induced dephasing in GaAs.* Physical Review **71** (1993).

[Wan94]   H. Wang, J. Shah, and T. Damen. *Polarization-dependent coherent nonlinear optical response in GaAs quantum wells.* Solid State Communications **91** (1994).

[Wil21]   N. P. Wilson, K. Lee, J. Cenker, K. Xie, A. H. Dismukes, E. J. Telford, J. Fonseca, S. Sivakumar, C. Dean, T. Cao, X. Roy, X. Xu, and X. Zhu. *Interlayer electronic coupling on demand in a 2D magnetic semiconductor.* Nature materials **20**, 1657–1662 (2021).

[Wil69]   J. A. Wilson and A. D. Yoffe. *The transition metal dichalcogenides discussion and interpretation of the observed optical, electrical and structural properties.* Advances in Physics **18**, 193–335 (1969).

[Win01]   C. Winnewisser, J. Schneider, M. Börsch, and H. W. Rotter. *In situ temperature measurements via ruby R lines of sapphire substrate based InGaN light emitting diodes during operation.* Journal of Applied Physics **89**, 3091–3094 (2001).

[Woź20]    T. Woźniak, P. E. Faria Junior, G. Seifert, A. Chaves, and J. Kunstmann. *Exciton g factors of van der Waals heterostructures from first-principles calculations.* Physical Review B **101** (2020).

[Xu14]     X. Xu, W. Yao, Di Xiao, and T. F. Heinz. *Spin and pseudospins in layered transition metal dichalcogenides.* Nature Physics **10**, 343–350 (2014).

[Xua20]    F. Xuan and S. Y. Quek. *Valley Zeeman effect and Landau levels in two-dimensional transition metal dichalcogenides.* Physical Review Research **2** (2020).

[Yan15a]   L. Yang, W. Chen, K. M. McCreary, B. T. Jonker, J. Lou, and S. A. Crooker. *Spin Coherence and Dephasing of Localized Electrons in Monolayer MoS₂.* Nano letters **15**, 8250–8254 (2015).

[Yan15b]   L. Yang, N. A. Sinitsyn, W. Chen, J. Yuan, J. Zhang, J. Lou, and S. A. Crooker. *Long-lived nanosecond spin relaxation and spin coherence of electrons in monolayer MoS2 and WS2.* Nature Physics **11**, 830–834 (2015).

[Yan20]    M. Yang, C. Robert, Z. Lu, D. van Tuan, D. Smirnov, X. Marie, and H. Dery. *Exciton valley depolarization in monolayer transition-metal dichalcogenides.* Physical Review B **101** (2020).

[Yao08]    W. Yao, Di Xiao, and Q. Niu. *Valley-dependent optoelectronics from inversion symmetry breaking.* Physical Review B **77** (2008).

[Ye17]     Z. Ye, D. Sun, and T. F. Heinz. *Optical manipulation of valley pseudospin.* Nature Physics **13**, 26–29 (2017).

[Yeh15]    P.-C. Yeh, W. Jin, N. Zaki, D. Zhang, J. T. Liou, J. T. Sadowski, A. Al-Mahboob, J. I. Dadap, I. P. Herman, P. Sutter, and R. M. Osgood. *Layer-dependent electronic structure of an atomically heavy two-dimensional dichalcogenide.* Physical Review B **91** (2015).

[You15]    Y. You, X.-X. Zhang, T. C. Berkelbach, M. S. Hybertsen, D. R. Reichman, and T. F. Heinz. *Observation of biexcitons in monolayer WSe2.* Nature Physics **11**, 477–481 (2015).

[Yu10]     P. Y. Yu and M. Cardona. *Fundamentals of Semiconductors: Physics and Materials Properties.* 4th ed. Springer eBook Collection. Berlin, Heidelberg: Springer Berlin Heidelberg, 2010.

*Bibliography*

[Yu14]     T. Yu and M. W. Wu. *Valley depolarization due to intervalley and intravalley electron-hole exchange interactions in monolayer MoS2.* Physical Review B **89** (2014).

[Yu23]     L. Yu, K. Pistunova, J. Hu, K. Watanabe, T. Taniguchi, and T. F. Heinz. *Observation of quadrupolar and dipolar excitons in a semiconductor heterotrilayer.* Nature materials (2023).

[Zen13]    H. Zeng, G.-B. Liu, J. Dai, Y. Yan, B. Zhu, R. He, L. Xie, S. Xu, X. Chen, W. Yao, and X. Cui. *Optical signature of symmetry variations and spin-valley coupling in atomically thin tungsten dichalcogenides.* Scientific reports **3**, 1608 (2013).

[Zha09]    G. P. Zhang, W. Hübner, G. Lefkidis, Y. Bai, and T. F. George. *Paradigm of the time-resolved magneto-optical Kerr effect for femtosecond magnetism.* Nature Physics **5**, 499–502 (2009).

[Zha14]    Y. Zhang, T.-R. Chang, B. Zhou, Y.-T. Cui, H. Yan, Z. Liu, F. Schmitt, J. Lee, R. Moore, Y. Chen, H. Lin, H.-T. Jeng, S.-K. Mo, Z. Hussain, A. Bansil, and Z.-X. Shen. *Direct observation of the transition from indirect to direct bandgap in atomically thin epitaxial MoSe2.* Nature nanotechnology **9**, 111–115 (2014).

[Zha17]    X.-X. Zhang, T. Cao, Z. Lu, Y.-C. Lin, F. Zhang, Y. Wang, Z. Li, J. C. Hone, J. A. Robinson, D. Smirnov, S. G. Louie, and T. F. Heinz. *Magnetic brightening and control of dark excitons in monolayer WSe2.* Nature nanotechnology **12**, 883–888 (2017).

[Zha23]    Y. Zhang, C. Xiao, D. Ovchinnikov, J. Zhu, X. Wang, T. Taniguchi, K. Watanabe, J. Yan, W. Yao, and X. Xu. *Every-other-layer dipolar excitons in a spin-valley locked superlattice.* Nature nanotechnology **18**, 501–506 (2023).

[Zhu11]    Z. Y. Zhu, Y. C. Cheng, and U. Schwingenschlögl. *Giant spin-orbit-induced spin splitting in two-dimensional transition-metal dichalcogenide semiconductors.* Physical Review B **84** (2011).

[Zhu14]    C. R. Zhu, K. Zhang, M. Glazov, B. Urbaszek, T. Amand, Z. W. Ji, B. L. Liu, and X. Marie. *Exciton valley dynamics probed by Kerr rotation in WSe2 monolayers.* Physical Review B **90** (2014).

[Zhu20]     E. A. Zhukov, V. N. Mantsevich, D. R. Yakovlev, N. E. Kopteva, E. Kirstein, A. Waag, G. Karczewski, T. Wojtowicz, and M. Bayer. *Renormalization of the electron g factor in the degenerate two-dimensional electron gas of ZnSe- and CdTe-based quantum wells*. Physical Review B **102** (2020).

[Zib14]     N. Zibouche, A. Kuc, J. Musfeldt, and T. Heine. *Transition–metal dichalcogenides for spintronic applications*. Annalen der Physik **526**, 395–401 (2014).

[Zip18]     J. Zipfel, J. Holler, A. A. Mitioglu, M. V. Ballottin, P. Nagler, A. V. Stier, T. Taniguchi, K. Watanabe, S. A. Crooker, P. C. M. Christianen, T. Korn, and A. Chernikov. *Spatial extent of the excited exciton states in WS2 monolayers from diamagnetic shifts*. Physical Review B **98** (2018).

[Zip20]     J. Zipfel. „Excitons in monolayer semiconductors in complex environments and under external fields". PhD thesis. Universität Regensburg, 2020.

# Acknowledgements / Dank

An dieser Stelle möchte ich einigen Leuten explizit danken, die an der fruchtbaren Zeit der Promotion und dem Gelingen dieser Arbeit maßgeblich beteiligt waren.

Mein besonderer Dank geht an meinen Doktorvater Christian Schüller, der ganz viel Wohlwollen und Zutrauen in mich gesetzt hat und es mir ermöglicht hat, tief in die Welt der (Halbleiter-) Physik einzutauchen. Deine Fähigkeit, komplexe Sachverhalte einfach zu erklären und ein intuitives Verständnis dafür zu entwickeln, hat mit sehr oft die Augen geöffnet und neue Impulse für die weiter Arbeit gesetzt. Herzlichen Dank für Deine unkomplizierte Art, Dein offenes Ohr und Deine intrinsische Begeisterung für die Weitergabe Deines Wissens!

Ganz herzlich danken möchte ich allen Mitgliedern der Arbeitsgruppe Schüller, angefangen bei Johannes Holler, der das Verbindungsglied in die Gruppe darstellte. Danke für Deine Hilfsbereitschaft, Deine Herzlichkeit und für Deine Freundschaft. Ich bin sehr dankbar über die Fülle der gemeinsamen Zeit im Büro, Labor und auch außerhalb der Uni. Es war sehr viel wert, einen guten Freund als Kollegen zu haben. Du hast entscheidend dazu beigetragen, dass mir die Uni, aber auch Regensburg selbst zur neuen Heimat wurde. Danke auch an meinen zweiten Bürokollegen und Freund Michael Kempf. Ihr habt zusammen für Leichtigkeit und gute Laune im manchmal etwas zähem Laboralltag und während den grauen Wintertagen gesorgt.

Weiteren Dank möchte ich an meine Kollegen Andreas Beer, Philipp Parzefall, Caique Serati de Brito und Anna Weindl richten. Danke für die vielen kleinen Gespräche zwischen Tür und Angel oder beim Mittagessen über die Physik und darüber hinaus. Danke Phillip für die Radtouren und Urlaube vor, nach oder während den Konferenzen. Danke Andi für Deine endlose Begeisterung für die Physik und das Leben und die vielen emotionalen Diskussionen darüber.

Besonders hervorheben möchte ich an dieser Stelle noch einmal den Beitrag meiner zu betreuenden Bachelor- und Masterstudenten: Gabriela Hirschinger, Dennis Falter, Marco Schmauser, Simon Feldl, Petter Marzena, Eleonora Buchholz und